

SAND 2002-8018
Unlimited Release
Printed March 2002

Applied Microfluidic Physics LDRD

Final Report

E. B. Cummings
S. K. Griffiths
R. H. Nilson

Sandia National Laboratories

Abstract

The transport phenomena electrokinesis and dielectrophoresis are studied theoretically, experimentally, and computationally. Novel electrokinesis-based microfluidic devices are synthesized to solve practical engineering problems including turning and injecting analyte bands. The novel experimental methodology used to validate the theory and computational software tools is described and presented. Finally, the computational software tools developed to assist with both practical design and fundamental theory are presented.

This page intentionally contains only this sentence.

Contents

1	Overview	9
1.1	Introduction to ideal electrokinesis	9
1.2	Accomplishments of this LDRD	11
2	Summary of published results	13
2.1	Conditions for similitude in electroosmotic flow	13
2.2	Liposome flow markers for PIV	13
2.3	Electroosmosis at non-negligible zeta potentials	14
2.3.1	Abstract	14
2.3.2	Summary	14
2.4	Hydrodynamic dispersion in electroosmotic flow	15
2.4.1	Abstract	15
2.4.2	Summary	16
2.5	Low-dispersion turns and junctions	16
2.5.1	Abstract	16
2.5.2	Summary	17
2.6	Band spreading in microchannel turns	18
2.6.1	Abstract	18
2.6.2	Summary	18
2.7	Low dispersion turns patent summary	19
3	EK and DEP in arrays of insulating posts	21
3.1	Abstract	21
3.2	Introduction	22
3.3	Electrostatically driven flow	23
3.3.1	Physics of electrokinesis	23
3.3.2	Physics of dielectrophoresis	24
3.3.3	Continuum equations	24
3.4	Experimental Apparatus	26
3.5	Results	27
3.5.1	Electrokinesis	27
3.5.2	Filamentary dielectrophoresis	27
3.5.3	Trapping dielectrophoresis	28
3.6	Conclusions	28
4	A PIV methodology for high-resolution statistics	45
4.1	Abstract	45
4.2	Introduction	46
4.3	Processing procedure	46

4.3.1	Single-pixel correlation	47
4.3.2	Multiple-point correlations	47
4.4	Steady electrokinetic flow in uniform post arrays	48
4.4.1	Basis function for the nonlinear filter	48
4.4.2	Experimental apparatus	49
4.4.3	Results	49
4.5	Stationary turbulent circular jet	50
4.5.1	Basis function for the nonlinear filter	51
4.5.2	Experimental apparatus	51
4.5.3	Results	52
4.6	Conclusions	53
5	Laplace: general-purpose ideal EK flow simulator	65
5.1	Abstract	65
5.2	Introduction	66
5.3	Software overview	69
5.3.1	Format and philosophy	69
5.3.2	Data display	70
5.3.3	Data exporting	70
5.3.4	Session serialization	70
5.4	Grid formation	70
5.4.1	The user interface	71
5.4.2	Notes from beneath the hood	72
5.5	The flow solver	72
5.5.1	The user interface	73
5.5.2	Notes from beneath the hood	73
5.5.3	Port boundary conditions	73
5.6	Flow post-processing	73
5.6.1	Steps	74
5.6.2	Particles	74
5.6.3	Contours	74
5.6.4	Super particles	74
5.6.5	Flows	75
5.7	Conclusions	75
5.8	Future development areas	75

List of Figures

3.1	Diagram of the experimental apparatus for studying electrokinesis and dielectrophoresis in microarrays. Video from the inverted epifluorescence microscope is digitized and recorded to disk. The glass substrate containing the microfluidic channels is supported in a fixture combining a vacuum chuck, reservoirs, and electrodes. The optical micrographs show patterned glass microchannels used in this study.	30
3.2	Raw experimental particle image used in the PIV analysis. The image spans a $520\text{-}\mu\text{m} \times 390\text{-}\mu\text{m}$ rectangle.	31
3.3	Overlay of experimental speed field on ideal electrokinetic speed field. The electric field of 2 V/mm is applied from top to bottom, oriented down columns of $93\text{-}\mu\text{m}$ circular posts on $200\text{-}\mu\text{m}$ centers. The fringe spacing is $24.5\text{ }\mu\text{m/s}$. Experimental measurements occupy a rectangle that includes the central four circular posts. The measurements can be distinguished from the ideal flow by the presence of scatter and flow imperfections of order $2\text{ }\mu\text{m/s}$	32
3.4	Overlay of experimental speed field on ideal electrokinetic speed field. The electric field of 2 V/mm is applied from top to bottom, oriented at 45° with respect to columns of $93\text{-}\mu\text{m}$ circular posts on $200\text{-}\mu\text{m}$ centers. The fringe spacing is $24.5\text{ }\mu\text{m/s}$. The rectangle containing experimental measurements is tilted by 45° toward the bottom left end of the image.	33
3.5	Overlay of experimental speed field on ideal electrokinetic speed field. The electric field of 2 V/mm is applied from top to bottom, oriented at 20° with respect to columns of $93\text{-}\mu\text{m}$ circular posts on $200\text{-}\mu\text{m}$ centers. The fringe spacing is $24.5\text{ }\mu\text{m/s}$	34
3.6	Overlay of experimental speed field on ideal electrokinetic speed field. The electric field of 1 V/mm is applied from top to bottom, oriented down columns of $142\text{-}\mu\text{m}$ square posts on $200\text{-}\mu\text{m}$ centers. The fringe spacing is $9.8\text{ }\mu\text{m/s}$	35
3.7	Overlay of experimental speed field on ideal electrokinetic speed field. The electric field of 1 V/mm is applied from top to bottom, oriented at 22° with respect to columns of $104\text{-}\mu\text{m}$ square posts on $200\text{-}\mu\text{m}$ centers. The fringe spacing is $4.9\text{ }\mu\text{m/s}$	36
3.8	Time-averaged particle fluorescence image of a predominantly electrokinetic flow. The fluorescence intensity is proportional to particle concentration. The slight rarefaction at the stagnation streamline evidenced by the dark streak is apparently a weak filamentary dielectrophoretic effect.	37
3.9	Particle fluorescence image of filamentary dielectrophoretic flow produced by an applied field of 80 V/mm from top to bottom, oriented at 45° with respect to columns of $36\text{-}\mu\text{m}$ square posts on $63\text{-}\mu\text{m}$ centers. The fluorescence intensity variation shows strong effects of dielectrophoretic concentration and rarefaction of particles.	38

3.10	Particle fluorescence image of filamentary dielectrophoresis at the end of an array. The flow is from top to bottom produced by an applied field of 80 V/mm, oriented at $\sim 2^\circ$ with respect to columns of $36\text{-}\mu\text{m}$ square posts on $63\text{-}\mu\text{m}$ centers. Particles are significantly depleted along the post columns.	39
3.11	Particle fluorescence image of flow at the entrance of the square array in Fig. 3.10. The amount of rarefaction grows as the flow passes repeatedly past rows of posts. . .	40
3.12	Particle fluorescence image of filamentary dielectrophoresis at the end of an array. The flow is from top to bottom produced by an applied field of 25 V/mm oriented down columns of $33\text{-}\mu\text{m}$ circular posts on $63\text{-}\mu\text{m}$ centers. The fluorescence intensity variation shows the dielectrophoretic concentration of particles in the region along the post columns.	41
3.13	Particle fluorescence image and calculated ideal electrokinetic streamlines and electric field magnitude (indicated by a spectral color map: blue corresponds to high field). The concentration of filament is nearly constant along streamlines but varies significantly across streamlines.	42
3.14	Particle fluorescence image of dielectrophoretic trapping. The flow is from top to bottom produced by an applied field of 100 V/mm down columns of $33\text{-}\mu\text{m}$ circular posts on $63\text{-}\mu\text{m}$ centers. Regions of trapped particles emit intense fluorescence. The overlayed image shows a simplified model of the potential experienced by particles. Regions where isopotentials curve back onto a post are dielectrophoretic traps. . . .	43
4.1	Experimentally measured velocity histograms from single-pixel subimages in a turbulent flow vs. the number of frame-pair correlations. The curves at the top and bottom were obtained in low- and high-turbulence regions, respectively.	54
4.2	Diagram of the experimental apparatus for studying electrokinetic flow in microarrays and micrographs of patterned glass microarrays.	55
4.3	Electrokinetic speed field within an array of circular posts at 45° with respect to the applied electric field. The fringe spacing is 0.5 pixels per image delay ($24.5\text{ }\mu\text{m/s}$). .	56
4.4	Electrokinetic speed field within an array of circular posts at 22.5° with respect to the applied electric field. The fringe spacing is 0.5 pixels per image delay ($24.5\text{ }\mu\text{m/s}$). .	57
4.5	Electrokinetic u velocity field in an array of square posts at 0° with respect to the electric field applied from left to right. The fringe spacing is 0.2 pixels per image delay ($9.8\text{ }\mu\text{m/s}$). The inset image show a detail of the flow in the upper-right junction. The white rectangle in the inset shows the size of a single pixel.	58
4.6	Electrokinetic speed field within an array of square posts at 45° with respect to the applied electric field. The fringe spacing is 0.5 pixels per image delay ($24.5\text{ }\mu\text{m/s}$). The inset image shows a detail of the flow in the upper right junction.	59
4.7	Color map and simulated interferogram of the mean speed field in the turbulent jet measured with 8×8 -pixel subimages. Red corresponds to zero speed and blue corresponds to 10 pixels displacement between images.	60
4.8	Color map and simulated interferogram of the mean speed field in the turbulent jet measured with single-pixel subimages. Red corresponds to zero speed and blue corresponds to 10 pixels displacement between images.	61
4.9	Color map and simulated interferogram of the components of the effective variance (σ) and peak correlation amplitude (A) measured with 8×8 -pixel subimages. The color-map ranges and fringe spacings are indicated beneath the images. The units of the variance are pixels per image delay and the units of the amplitude are arbitrary.	62
4.10	Color map and simulated interferogram of the components of the eccentricity vector measured with 8×8 -pixel subimages. The color-map ranges and fringe spacings are indicated beneath the image in units of pixel per image delay.	63

4.11	Color map of the Gaussian two-point correlation width from six different reference locations. The reference locations are located at the centers of the pronounced red spots in each image, corresponding to a small correlation width. The dip in the correlation width surrounding the reference point is evidence of the geometry of eddies near the reference region.	64
5.1	Sample black and white image of a whimsical microchannel design. Curves and lines that are not aligned with the rows and columns of the image are represented as abrupt steps.	67
5.2	Sample anti-aliased gray-scale image of the same whimsical design as in Fig. 5.1. Boundary curves and lines are smoothed by representing them using grayscales. This smoothing dramatically improves numerical results produced by Laplace	76
5.3	Sample anti-aliased and blurred gray-scale image of the same whimsical design. The blurring simulates the slope of walls that are fabricated using non-ideal techniques, e.g., embossing by an imperfect stamp. This allows the user to simulate systems that approximate production geometries.	77
5.4	Close up of a corner from the previous three grids showing the effect of anti-aliasing and blurring.	78
5.5	Particular speed field solutions obtained by Laplace using the black-and-white grid in Fig. 5.1 at left and the gray-scale grid in Fig. 5.2 at right. The speed fields are presented as simulated interferograms. The solution at left shows considerable artifacts of the discrete boundary steps, while that at right is less affected.	79
5.6	Grids and solutions derived from Fig. 5.3 at varying amounts of downsampling. The image in the left column is the downsampled grid image (blue-green pixels are outside the solution domain). The center column of images shows a simulated interferogram of the speed field. The right column shows calculated streamlines overlayed on a color map of the speed field. The streamlines are affected more than the speed field by reductions in resolution.	80
5.7	Calculated curves of the inverse of the particle transit time through the whimsical microsystem versus stream function. The gross deviations of these curves at low resolution is caused by cumulative errors from interpolation in the particle-propagation.	81
5.8	Fields that Laplace can display and save to disk.	82
5.9	Screen shot of Laplace displaying the computational grid of an array at low resolution.	83
5.10	Screen shots of Laplace graphically displaying the equations automatically generated an interior point (a.) near an internal boundary (b. and c.) and at a port (d.) Interior equations are gridded using a 9-point Laplacian stencil. Equations next to boundaries require a customized stencil.	84
5.11	Screen shot showing the dialog box used to adjust the way field images are displayed.	85
5.12	Screen shot of dialog used to set the properties of the automatically generated array image.	85
5.13	Screen shot of the solver-controller dialog showing the daunting list of Krylov subspace iterator options. Fortunately the default settings have been chosen for their good performance on even ill-conditioned geometries. Press “Solve” to solve.	86
5.14	Screen shot of the port-properties dialog. This dialog is currently “read only” but that status may change in future developments.	86
5.15	Screen shot of the sequenced-field-properties dialog that allows users to specify an arbitrary sequence of propagation steps for post-processing of the solution.	87
5.16	Electrokinetic streamlines and streaklines in an array of circular posts. The background image shows a spectral color map of the electrokinetic speed. Blue is the highest speed and red is zero speed.	88

5.17 Streaklines of simulated particles undergoing electrokinesis and diffusion (a.) and electrokinesis, dielectrophoresis, and diffusion (b.). Trapping dielectrophoresis is evident in b. The background image is a color map of the mean particle speed through the array. Blue is the highest speed and red is zero speed.	89
--	----

Acknowledgment

The authors gratefully acknowledge the skillful help of Allen Salmi in designing and fabricating the laboratory apparatus, George Sartor in fabricating our microfluidic circuits, and Robert Schefer in applying our diagnostics to macroflows. We also thank Anup Singh for his ideas and help in using fluorescent liposomes for particle-image velocimetry flow markers, which ultimately led us to discover a new class of microdevices based on dielectrophoresis.

This LDRD benefited tremendously from the efforts of the PETSC (portable extensible toolkit for scientific computation) program of Argonne National Laboratory and the authors are grateful for the superb library package they have published.

The authors also owe a debt of gratitude to Costanzo LaJeunesse who helped to put `Laplace` software application into a format suitable for its initial release.

This work was funded by a Sandia Engineering Sciences LDRD. Sandia is a multi-program laboratory operated by Sandia Corporation, a Lockheed-Martin company, for the United States Department of Energy under contract DE-AC04094AL85000.

CHAPTER 1

Applied Microfluidic Physics LDRD Overview

The primary goal of the Applied Microfluidic Physics LDRD was to develop a fundamental understanding of and experimental and design tools for electrokinesis-based microsystems. This report overviews selected accomplishments of the LDRD. Accomplishments that have been previously published are summarized and referenced in Chapter 2. Non-patent-sensitive unpublished accomplishments are detailed in Chapters 3–5. A significant volume of the accomplishments of this LDRD are documented in patent filings that remain pending at the time of this writing and are not presented. Intellectual-property sensitive material that has not previously been publicly disclosed is intentionally absent from this report to protect Sandia’s investment.

This LDRD successfully achieved its objectives and additionally generated microfluidic device designs and methodologies having substantial technological importance. These advances include the precision experimental validation of the theory of ideal electrokinesis, the inventions of low-dispersion turns and junctions, high-performance sample-injection methodologies, and the invention of a new class of microfluidic devices based upon dielectrophoresis. The LDRD has also produced powerful and simple-to-use software for simulating electrokinesis and dielectrophoresis-based microsystems of arbitrary quasi-two-dimensional geometry. In the course of meeting the objectives of the LDRD, significant advances were made in the field of microflow diagnostics, fixturing, and instrumentation.

The following sections of this chapter describe the concept of ideal electroosmosis, a central theoretical advance behind the technical advances in this LDRD, and overviews the motivation behind and the results of the AMPL LDRD.

1.1 Introduction to ideal electrokinesis

Electrokinesis (EK), the flow of a material having a net mobile charge under the influence of an applied electric field, is a physical phenomenon behind an emerging billion dollar industry. Electrokinesis embodies both electrophoresis (EP)—electrokinesis of solids immersed in a liquid—and electroosmosis (EO)—electrokinesis of liquids past solid boundaries. Electrophoresis is widely used in analytical chemistry and microbiology to separate molecules and particles by charge-to-mass ratio or surface-charge density. Electroosmosis is used to produce flow and pressure in electrokinetic pumps and to augment transport of molecules and particles in chemical separations by capillary electrochromatography (CEC) and recently in more general microfluidic systems.

First documented in 1809 by Reuss in observations of electrostatically induced flow in fine glass capillaries[32], electrokinesis in straight channels and simple geometries has been studied extensively

during the 20th century[37, 33, 30][...]. The nanoscopic physics behind electrokinesis is understood qualitatively. Quantitative semi-empirical models based upon this physical understanding are successful at reducing experimental data and reconciling data from different types of electrokinetic systems.

The problem of understanding electrokinesis in systems of arbitrary geometry[25] has until recently been less successful. Numerical or theoretical modelling requires the coupling of the Navier-Stokes flow equations, the Poisson equation of electrostatics, the Boltzmann equation of statistical thermodynamics and species transport equations, together with models of physical properties at the liquid-solid interfaces. The numerical solution of these coupled equations is complicated by the wide range of length scales in typical flow systems of interest. For example, the physical properties of the liquid typically vary over a distance $O(1-10\text{ nm})$ from the solid boundary. The thickness of the layer in the fluid having an appreciable mobile net charge, the Debye layer, is typically $O(1-100\text{ nm})$. Photolithographically defined microchannels most often used in microfluidics have cross-flow dimensions typically $O(1-100\text{ }\mu\text{m})$. The length of such channels can be $O(10-100\text{ mm})$. There have been a number of attempts at simulation of electrokinesis in spite of these difficulties[26], but the disparity in length scales typically requires the modeler to adopt physically unrealistic approximations, e.g., expanding the thickness of the Debye layer by three orders of magnitude.

In a previous Sandia LDRD, the concept of “ideal electrokinesis” was explored[5]. The goal of the study was to find a physically meaningful ideal limit of electrokinetic flow which was analytically and numerically tractable. This study produced the theoretically and technologically important result that the electrokinetic flow velocity field is everywhere proportional to the local electric field within the fluid, provided some well-defined conditions are met. The uniform proportionality between the electric field and flow velocity is termed “similitude.” The value of the proportionality coefficient is the same as the empirical constant developed previously for simple geometries. Ideal electrokinesis is a useful concept since it represents a desirable limiting case in which hydrodynamic dispersion is minimal and both the flow and electric field can be derived from a single solution of the Laplace equation. A wide range of numerical methods, analytic tools, and mathematical theorems have been derived for solutions of this equation. The conditions for similitude are[7]

1. the geometrical dimensions of the flow channel are everywhere large compared to the thickness of the Debye layer,
2. the liquid is at least weakly conductive and has a uniform conductivity, dielectric constant, and viscosity (outside the Debye layer),
3. the surfaces bounding the channels are non-conducting, impervious to the fluid, and have a uniform surface charge density, and
4. the flow through entry and exit ports of the system satisfies similitude.

Condition 1. is met for most photolithographically defined channels and systems of interest in microfluidics. Condition 2. is met for systems filled with a uniform liquid, which applies to many microfluidic applications, but notably excludes separation systems employing buffer gradients and “sample stacking.” Condition 3. is commonly satisfied locally within a microsystem, but cannot apply everywhere, since the electric field is applied by electrodes that cannot be insulating. Fortunately, the perturbation produced by the electrodes decays rapidly away from the electrodes, so both Condition 3. and 4. are approximated to a high precision provided electrodes are located remotely. Condition 4. also requires that there is no total pressure difference across the entry and exit ports. Such differences can be minimized in practical systems by nulling pressure differences produced hydrostatically and by surface tension, locating electrodes in comparatively large open fluid reservoirs, and constructing microsystems from a single type of material.

1.2 Accomplishments of this LDRD

Although supported by a mathematical proof (see also Section 2.1), the concept of ideal electrokinesis required definitive experimental validation to show that the physical presumptions[7] behind ideal electrokinesis are correct and to demonstrate that the conditions for similitude can be readily approached in practice. This validation appears in Chapter 3. A new high-resolution particle-image velocimetry methodology was developed to perform this validation convincingly. This technique, documented in Chapter 4, can provide measurements of the velocity fields of stationary flows having a spatial resolution limited only by optical diffraction. Although outside the thrust of the LDRD, the methodology was also applied to study a turbulent jet flow. This demonstration showed for the first time how a parallel technique like particle-image velocimetry can effectively provide high-resolution flow velocity statistics and multiple-point correlations previously obtainable only by point techniques like laser Doppler velocimetry or hot-wire anemometry.

The precision validation of ideal electrokinesis helps to liberate the microfluidic designer from a difficult, expensive, and time-consuming design—fabricate—test design cycle to a design—simulate cycle. This cycle was not immediately easy to embrace, however, since appropriate simulation tools were not available. The software application **Laplace** was written to assist designers with the new design methodology. **Laplace** rapidly and precisely simulates ideal electrokinesis in quasi-planar microsystems whose geometry is defined by a bitmap image—essentially a picture of the microsystem. It has been a useful tool for our theoretical development as well, providing all the numerical simulations that appear in this report. Chapter 5 outlines the **Laplace** software.

Perhaps most exciting, mathematical modeling tools allow designers to adopt the most modern design technique (which is no longer a cycle): identify requirements—synthesize a design to meet these requirements. Several high-value synthetic designs[17] were developed and filed for patent protection during this LDRD. A patent describing the optimum geometry of low-dispersion turns and junctions (US 6,270,641B1) has issued in August 2000 (see Section 2.7). These turns allow designers to bend and fold channels on chips without the substantial dispersion penalty of conventional turns. As a result of these designs, meter-long separation columns can be shrunk below the size of a fingernail with an insignificant loss in separation efficiency.

Ideal electrokinesis has the special property of “solenoidality.” This means particles and molecules undergoing electrokinesis are neither concentrated nor rarefied. Thus, when particle concentration gradients began to appear in experiments that should have satisfied the conditions for ideal electrokinesis, it was clear that a different transport phenomenon had appeared[9]. Indeed this understanding led to the immediate diagnosis of dielectrophoresis, the flow of particles under the action of an electric field gradient. Dielectrophoresis is of second order in the applied electric field and proportional to the difference between the particle and immersion-fluid polarizability, just like buoyancy is proportional to the difference between the particle and immersion-fluid density. Most importantly, dielectrophoresis is *not* solenoidal so it can concentrate and rarefy particles. While the details of the work in dielectrophoresis are sensitive Sandia intellectual property, they promise to produce a new class of microfluidic devices. Our publicly disclosed work in dielectrophoresis appears in Chapter 3.

This page intentionally contains only this sentence.

CHAPTER 2

Summary of published results from the AMPL LDRD

This chapter presents references, abstracts, and brief summaries of selected published results of the AMPL LDRD.

2.1 Conditions for similitude between the electric field and flow velocity in electroosmotic flow

Cummings, E. B., Griffiths, S. K., Nilson, R. H., Paul, P. H. (2000) "Conditions for similitude between the fluid velocity and electric field in electroosmosis," *Anal. Chem.*, **72**, pp 2526–2532.[7]

Electroosmotic flow is fluid motion driven by an electric field acting on the net fluid charge produced by charge separation at a fluid-solid interface. Under many conditions of practical interest, the resulting fluid velocity is proportional to the local electric field, and the constant of proportionality is everywhere the same. Here we show that the main conditions necessary for this similitude are a steady electric field, uniform fluid and electric properties, an electric Debye layer that is thin compared to any physical dimension, and fluid velocities on all inlet and outlet boundaries that satisfy the Helmholtz-Smoluchowski relation normally applicable to fluid-solid boundaries. Under these conditions, the velocity field can be determined directly from the Laplace equation governing the electric potential, without solving either the continuity or momentum equations. Three important consequences of these conditions are that the fluid motion is everywhere irrotational, that fluid velocities in two-dimensional channels bounded by parallel planes are independent of the channel depth, and that such flows exhibit no dependence on the Reynolds number. Similitude is demonstrated by comparing measured and computed fluid streamlines with computed electric flux lines.

2.2 Fluorescent liposome flow markers for microscale particle-image velocimetry

Singh, A. K., Cummings, E. B., Throckmorton, D. J., (2001) "Fluorescent liposome flow markers for microscale particle-image velocimetry," *Anal. Chem.*, **73**, pp 1057–1061.[36]

Unilamellar liposomes carrying both encapsulated and surface-immobilized fluorophores have been synthesized as novel fluorescent markers to image flow profiles in microfabricated structures. The unilamellar liposomes were made with phospholipids and cholesterol by extrusion through a polycarbonate membrane. They contained carboxyfluorescein in the aqueous core and fluorescein-labeled lipids in the bilayer to render them both a surface and volume fluorescer, maximizing their fluorescence intensity. The lipid composition was chosen to impart a net negative charge to liposomes to minimize self-aggregation as well as interaction with negatively charged glass surfaces of the channels. These liposomes were mono-disperse (mean diameter 283 nm), neutrally buoyant, and hydrophilic and exhibited no adsorption on glass surfaces. Unlike polystyrene spheres, they were readily broken up by surfactants, thereby allowing for easy and complete removal from microfluidic channels. The fluorescent liposomes were used to investigate pressure-driven flow in an offset cross intersection in a microfluidic chip and provided images with excellent signal-to-noise ratio. A novel computational scheme that is particularly suitable for analyzing particle-image velocimetry data in micrometer-scale flow channels was employed to analyze the images. These liposomes are easily synthesized and can be custom-made for various applications to offer a broad range of surface and volume characteristics such as charge, size, and surface chemistry.

2.3 *Electroosmotic fluid motion and late-time solute transport for large zeta potentials*

Griffiths, S. K., Nilson, R. H., (2000) "Electroosmotic fluid motion and late-time solute transport for large zeta potentials," *Anal. Chem.*, **72**, pp 4767–4777.[16]

2.3 Abstract

Analytical and numerical methods are employed to determine the electric potential, fluid velocity and late-time solute distribution for electroosmotic flow in a tube and channel when the zeta potential is not small. The electric potential and fluid velocity are in general obtained by numerical means. In addition, new analytical solutions are presented for the velocity in a tube and channel in the extremes of large and small Debye layer thickness. The electroosmotic fluid velocity is used to analyze late-time transport of a neutral non-reacting solute. Zeroth and first-order solutions describing axial variation of the solute concentration are determined analytically. The resulting expressions contain eigenvalues representing the dispersion and skewness of the axial concentration profiles. These eigenvalues and the functions describing transverse variation of the concentration field are determined numerically using a shooting technique. Results are presented for both tube and channel geometries over a wide range of the normalized Debye layer thickness and zeta potential. Simple analytical approximations to the eigenvalues are also provided for the limiting cases of large and small values of the Debye layer thickness. The methodology developed here for electroosmotic flow is also applied to the Taylor problem of late-time transport and dispersion in pressure-driven flows.

2.3 Summary

We have examined the electroosmotic fluid motion and late-time solute transport in a tube and in a channel for cases in which the zeta potential is not negligibly small. Using both numerical and analytical methods, the transverse variation of the electric potential and fluid speed were computed over a broad range of the normalized Debye layer thickness, λ^* , and the normalized zeta potential, ζ^* . These fluid velocities were then used to compute the late-time distribution of a neutral non-reacting solute carried in the flow.

The numerical procedure used here is based on a shooting method. This procedure was checked against previously-published analytical and numerical solutions for both large and small values of the zeta potential. In comparisons with analytical results for a negligible zeta potential, the two agree within a relative error of 10^{-6} for all values of the transverse position and values of λ^* between 10^{-3} and 10^3 .

Analytical solutions were also obtained for the fluid velocity in a tube and channel in the asymptotic limits of small and large λ^* . The first of these applies when the Debye layer thickness is small compared to the transverse tube or channel dimension and is valid for all values of the normalized zeta potential. The second is applicable to large values of the Debye layer thickness. These solutions are again valid for all ζ^* , but carry the restriction that $\sinh\zeta^*/\zeta^* < \lambda^{*2}$. The accuracy and applicable range of each solution is discussed, and expansions of the solutions for large and small ζ^* are provided.

Based on these fluid velocities and a series describing the full late-time concentration field, the mean axial variation of the field was determined in closed form. The first and second-order solutions describing this variation contain two unknown constants that arise as eigenvalues in the series solution. These eigenvalues are the coefficients of axial dispersion and skewness. They are determined numerically along with the solutions describing transverse variation of the concentration field. The numerical procedure reduces the governing equations to a system of ten coupled first-order ordinary differential equations, which are integrated in the transverse direction using a standard integration routine.

The results presented here recover the well-known solutions for dispersion in pressure-driven flows when the Debye length is sufficiently large. In this limit, the axial dispersion is proportional to the square of the Peclet number based on the transverse dimension of the tube or channel and is independent of the zeta potential. The skewness in this limit is proportional to the cube of this Peclet number and is also independent of the zeta potential. In the limit of a small Debye layer thickness, we find that the dispersion varies as the square of the Peclet number based on the Debye length. The skewness varies as the cube of this Peclet number. In this limit, both the dispersion and skewness exhibit a first-order dependence on the zeta potential. Simple approximations to the dependence are presented. We find that increasing values of the zeta potential always reduce both late-time dispersion and skewness.

The methodology devised here for analyzing the late-time transport in electroosmotic flow was also applied to the Taylor problem of pressure-driven flow in a tube and channel. This analysis yields new analytical solutions describing the axial variation of the mean solute concentration for the problems of an initial planar source and a translating solute interface.

2.4 Hydrodynamic dispersion of a neutral non-reacting solute in electroosmotic flow

SAND99-8249
Unlimited Release
Printed June 1999

2.4 Abstract

Analytical methods are employed to determine the axial dispersion of a neutral non-reacting solute in an incompressible electroosmotic flow. In contrast to previous approaches, the dispersion is obtained here by solving the time-dependent diffusion-advection equation in transformed spatial and temporal coordinates to obtain the two-dimensional late-time concentration field. The coefficient of dispersion arises as a separation eigenvalue, and its value is obtained as a necessary condition for satisfying

all of the required boundary conditions. Solutions based on the Debye-Hückel approximation are presented for both a circular tube and a channel of infinite width. These results recover the well-known solutions for dispersion in pressure-driven flows when the Debye length is very large. In this limit, the axial dispersion is proportional to the square of the Peclet number based on the characteristic transverse dimension of the tube or channel. In the limit of very small Debye lengths, we find that the dispersion varies as the square of the Peclet number based on the Debye length. Simple approximations to the coefficient of dispersion as a function of the Debye length and Peclet number are also presented.

2.4 Summary

Using analytical methods, we have determined the first-order concentration field and coefficient of axial dispersion of a neutral non-reacting solute in an incompressible electroosmotic flow. Here, in contrast to previous approaches, the dispersion is calculated by directly solving the governing transport equations. Using a late-time series to describe the full concentration field, the coefficient of dispersion arises naturally as a necessary condition for satisfying all required boundary conditions in transformed spatial and temporal coordinates.

Solutions based on the Debye-Hückel approximation are presented for both a circular tube and a channel of infinite width. These results recover the well-known solutions for dispersion in pressure-driven flows when the Debye length is very large. In this limit, the axial dispersion is proportional to the square of the Peclet number based on the characteristic transverse dimension of the tube or channel. In the limit of very small Debye lengths, we find that the dispersion varies as the square of the Peclet number based on the Debye length. Simple approximations to the dispersion as a function of the Debye length and Peclet number are also presented.

Although dispersion in both electroosmotic and pressure-driven flows grows as the square of the Peclet number, the coefficient of dispersion in an electroosmotic flow may be many orders of magnitude smaller than that for the parabolic velocity profile of a pressure-driven flow. The low coefficient of dispersion permits optimum operation of microchannel systems at very high Peclet numbers. This minimizes the role of ordinary diffusion in electroosmotic flows, thus offering the potential for long-range transport with little axial spreading of solute peaks or interfaces due to either dispersion or diffusion.

In addition to providing physical insight into the nature of dispersion in electroosmotic flow, the analytical solutions presented here provide a valuable benchmark for developing numerical solutions to related problems. Direct numerical simulation of transport in electroosmotic flow is a challenging task because widely disparate length scales, spanning nearly seven orders of magnitude, must be resolved. Benchmark solutions are important in such cases since accurate numerical solutions are difficult to obtain.

2.5 *Low-dispersion turns and junctions for microchannel systems*

Griffiths, S. K., Nilson, R. H., (2001) "Low-dispersion turns and junctions for microchannel systems," *Anal. Chem.*, **73**, pp 272–278.[17]

2.5 Abstract

Numerical methods are employed to optimize the geometry of two-dimensional microchannel turns such that the turn-induced spreading of a solute band is minimized. An inverted numerical method is first developed to compute the electric potential and local species motion in turns of arbitrary

geometry. The turn geometry is then optimized by means of a nonlinear least-squares minimization algorithm using the spatial variance of the species distribution leaving the turn as the object function. This approach yields the turn geometry producing the minimum possible dispersion, subject only to prescribed constraints. The resulting low-dispersion turns provide an induced variance two to three orders of magnitude below that of a comparable conventional turns. Sample results are presented for 180 and 90 degree turns, and the use of these turns to form wyes and tees is discussed. A sample 45 degree wye is presented. The use of low-dispersion turns in folding separation columns is also discussed, and sample calculations are presented for folding a column 100 μm in width and up to 900 mm in length onto a region of only 10 by 10 mm. These low-dispersion geometries are applicable to electroosmosis, electrophoresis and to some pressure-driven flows.

2.5 Summary

To quantify and remedy the dispersion occurring in turns and junctions, we have developed a numerical model describing species transport in electroosmotic flows, electrophoretic species motion, and species transport in some pressure-driven flows. This model is not based on traditional finite-difference or finite-element methods. Instead, we solve the governing equations by an inverted approach in which the dependent variables are the unknown values of the spatial coordinates and the independent variables are the electric potential and an associated stream function describing fluid or ion motion. The advantage of this approach is that the two-dimensional computational domain is always rectangular; the irregular topology of the channel walls appears only as boundary conditions on the regular computational domain. Transport in channels of arbitrarily complexity is thus easily analyzed by this approach, with no need for adaptive meshing schemes or for re-meshing the domain when the channel geometry is altered.

This inverted numerical model is coupled with a nonlinear least-squares minimization algorithm used to optimize the turn geometry. The minimization object function is simply the increased spatial variance of a species band accumulated in traversing the turn. To obtain a single optimum geometry often requires up to one hundred realizations of species transport through candidate turns, and each computational realization is equivalent to a single experiment. As such, it is unlikely that turns and junctions matching the performance of those described here could be obtained by experimental methods alone.

The resulting optimum geometries yield a turn-induced spatial variance of a sample band that is two to three orders of magnitude below that of equivalent conventional turns. For all turn angles, the species band emerging from the turn is nearly flat and orthogonal to the channel walls. Such turns are useful in microchannel systems for sample preparation and other routine transport processes. This dramatic improvement in turn-induced spreading also permits folding long separation columns onto small areas. Using the 180 degree turn presented here, a 100 μm channel up to 900 mm long can be folded onto a region covering only 10 by 10 mm. The turns in this configuration do not contribute significantly to band spreading for Peclet numbers up to about 8000. For electrophoretic processes, this corresponds to an applied electric field up to about 2000 kV/m.

The low-dispersion turns can also be used to form wyes and tees. Such junctions permit splitting a single sample into two equal sub-samples for subsequent parallel processing. Cascading a series of such wyes permits precise subdivision into numerous sub-samples that are all nearly flat and orthogonal to the channel walls. Further, all sub-samples will travel through this network at the same mean speed and so arrive simultaneously downstream. Low-dispersion junctions may also find use in joining sub-samples for mixing and dilution processes.

All of these low-dispersion turns and junctions are applicable to electroosmotic and electrophoretic transport. The channels may be either open or filled with a gel or porous material. They are further applicable to pressure-driven flows in packed or shallow channels. Finally, these low-dispersion geometries are readily produced using existing manufacturing methods. The optimum geometries do not rely on features very much smaller than the nominal channel width and do not require deep

narrow channels having high aspect ratios. The channel depths are also uniform, so these geometries can be produced using all existing molding, embossing and etching techniques.

2.6 Band spreading in two-dimensional microchannel turns for electrokinetic species transport

Griffiths, S. K., Nilson, R. H., (2000) "Band spreading in two-dimensional microchannel turns for electrokinetic species transport," *Anal. Chem.*, **72**, pp 5473–5482.[15]

2.6 Abstract

Analytical and numerical methods are employed to investigate species transport by electrophoretic or electroosmotic motion in the curved geometry of a two-dimensional turn. Closed-form analytical solutions describing the turn-induced diffusive and dispersive spreading of a species band are presented for both the low and high Peclet number limits. We find that the spreading due to dispersion is proportional to the product of the turn included angle and the Peclet number at low Peclet numbers. It is proportional to the square of the included angle and independent of the Peclet number when the Peclet number is large. A composite solution applicable to all Peclet numbers is constructed from these limiting behaviors. Numerical solutions for species transport in a turn are also presented over a wide range of the included angle and the mean turn radius. Based on comparisons between the analytical and numerical results, we find that the analytical solutions provide very good estimates of both dispersive and diffusive spreading provided that the mean turn radius exceeds the channel width. These new solutions also agree well with data from a previous study. Optimum conditions minimizing total spreading in a turn are presented and discussed.

2.6 Summary

Here we examine the spreading of a species band induced by electrophoretic or electroosmotic transport through a two-dimensional turn. Analytical solutions to the governing transport equations are obtained in the limits of low and high Peclet numbers. From these asymptotic behaviors, we construct a composite solution applicable to all Peclet numbers. Numerical solutions are also presented for a variety of turn geometries and a wide range of the Peclet number. These solutions rely on no approximations regarding either the Peclet number or geometry of the turn.

We find that the band spreading due to transport through by a turn is well described for all Peclet numbers by the composite solution

$$\left(\frac{\sigma}{a}\right)^2 = \frac{\theta^2 \epsilon Pe}{15} \theta + 3 \epsilon Pe + \frac{2\theta}{\epsilon Pe} \quad (2.1)$$

where σ^2 is the total increased variance of the downstream species distribution, a is the mean channel width, θ is the included angle of the turn, ϵ is the ratio of the channel width to the mean turn radius, and $Pe = Ua/D$ is the Peclet number based on the mean channel width and fluid or species speed. The first term on the right of this expression describes the dispersive contribution to the total variance; the second term describes the additional contribution of streamwise diffusion.

This analytical expression is based on an assumption that the radius of the turn is much larger than the channel width. Despite this assumption, the expression provides accurate results even when the turn radius is comparable to the channel width. Based on comparisons with our numerical results, we find that it yields both the dispersive component and total variance to within about 10% for all Peclet numbers, all $\bar{r}/a = 1/\epsilon \geq 1$, and included turn angles up to 180° .

The dispersive portion of the turn-induced variance in the high Peclet number limit is proportional to the squares of the channel width and the included turn angle, but is independent of both the Peclet number and radius of the turn. As such, more gradual turns do not reduce the variance when the product ϵPe is larger than about five times the included angle. On the contrary, large radius turns generally increase the total variance owing to the added contribution of streamwise diffusion. At low Peclet numbers, we find that the dispersive portion of the total variance is proportional to the product $\theta \epsilon Pe$. In this limit, the dispersive variance is thus inversely proportional to the turn radius. In contrast, the total variance grows in proportion to the turn radius when the Peclet number is small.

Based on the expression above, the total turn-induced variance exhibits a minimum between the extremes of low and high Peclet number if the included angle of the turn is greater than about 63° . The optimum condition defines either a preferred Peclet number for a fixed turn geometry or a preferred geometry for a fixed Peclet number. The total variance at this minimum is about a factor of two below the value in the high Peclet number limit for a 180° included angle. While this is a significant reduction, it may not provide any real practical benefit when the Peclet number is large. When the Peclet number is small, however, a large turn radius should be avoided to limit band spreading by diffusion. In this case, the benefit of the optimum geometry can be very large since diffusive spreading may far exceed that due to the turn geometry when the Peclet number is small.

Finally, this analytical expression is compared with experimental results previously obtained by Culbertson et al. We find that the dispersive portion of the expression agrees well with their data, provided that the mean channel width properly accounts for the channel sidewall taper.

2.7 Low dispersion turns patent summary

Inventors: Griffiths, S. K., Nilson, R. H.

The present invention improves the performance of microchannel systems by providing turns, wyes, tees, and other junctions that generate very little dispersion of a chemical or biological sample as it traverses the turn or junction. The reduced dispersion results from turns and junctions having contraction and expansion regions that constrict the cross-section area in a portion of the turn or junction. By carefully designing the geometries of the constricted portion and adjacent contraction and expansion regions, dispersion produced by the improved turns and junctions is reduced by orders of magnitude below that of conventional devices. Embodiments of the invention include: 45, 90 and 180 degree turns, wyes, and tees, as well as sample splitting devices and serpentine channels for folding long columns into small areas.

In one embodiment, the improved turns and junctions have rectangular cross sections and a uniform depth, permitting straightforward fabrication by conventional etching, molding and embossing techniques. Further, because the turns and junctions are only moderately constricted over relatively short distances, they do not lead to excessive increases in electrical resistance and Joule heating. This is made possible by the use of numerical algorithms to discern turn and junction geometries that dramatically reduce dispersion by contraction and expansion regions that offset most of the dispersion that would otherwise occur. This invention is applicable to pressure-driven chromatographic separations, electrochromatographic separations and electrophoretic separations, as well as many microfluidic processes such as routine sample transport, sample reaction and species synthesis. It is also applicable to channels and junctions that are open, filled with a gel, or filled with a porous or granular material.

This page intentionally contains only this sentence.

CHAPTER 3

Ideal electrokinesis and dielectrophoresis in arrays of insulating posts

3.1 *Abstract*

Electrokinesis and dielectrophoresis, technologically important particle and fluid transport mechanisms in microscale flow channels, are respectively linear and nonlinear in the electric field applied along the channel. Experimental and computational studies have been performed in three regimes of steady electrokinetic and dielectrophoretic particle transport in uniform square arrays of insulating posts. At low applied electric fields, electrokinesis dominates transport and is observed to approach “ideal electrokinesis” in which the particle and flow velocity field is irrotational outside nanometer-scale boundary layers. At moderate applied fields, dielectrophoresis is observed to produce flowing filaments of concentrated and rarefied particles. At high applied fields, dielectrophoresis becomes the dominant transport mechanism and is observed to concentrate and trap particles.

Nomenclature

ϵ	Dielectric constant of the fluid
ϕ	Electrostatic potential
μ_i	Electrokinetic mobility of the i -th chemical species
ν	Kinematic viscosity of the liquid
ν_i	Dielectrophoretic mobility of the i -th chemical species
ρ	Density
ρ_e	Charge density
ζ	Empirical effective potential of mobile particles near an interface
c_i	Concentration of the i -th chemical species
c_{i0}	Unforced equilibrium concentration of the i -th chemical species
D_i	Diffusivity of the i -th species in the fluid
e	Charge of an electron
\mathbf{E}	Electric field
\mathbf{i}	Electric current flux vector
\mathbf{j}_i	Flux vector of the i -th chemical species
k	Boltzmann’s constant
p	Pressure

- \mathbf{r} Position vector
- t Time
- T Absolute temperature
- \mathbf{u} Velocity vector
- z_i Charge number of the i -th chemical species

3.2 Introduction

Electrokinesis and dielectrophoresis are two technologically important transport phenomena produced by applying an electrostatic field to a conductive fluid. Electrokinesis was first observed by Reuss[32] in 1809 and has been studied extensively since the 19th century. Dielectrophoresis has been studied since the seminal papers and book[27] of Pohl in the 1970's. The current push to develop microfabricated chemical and biological processing and analysis systems has renewed interest in these phenomena.

Electrokinesis is particle or fluid transport produced by an electric field acting on a fluid having a net mobile charge[37, 29, 34]. Net charges appear within a nanometer-scale layer at many liquid/solid interfaces, e.g., water/glass, water/alumina and on many particles in solution, e.g., DNA. Electrokinesis is significant at the microscale and is of considerable practical importance in microfluidics, since it provides a mechanism for manipulating particles and conveying fluids in microsystems using only an applied electric field. The electrokinetic flow rate is linear in the electric field. "Ideal electrokinesis" is a limiting case of electrokinesis that is approached in systems having uniform insulating surfaces and uniform fluids. Ideal electrokinesis is irrotational with a velocity field everywhere proportional to the electric field. Ideal electrokinesis is a solenoidal transport mechanism and consequently does not produce particle concentration gradients in an initially uniform suspension[9].

Dielectrophoresis is particle motion produced by an electric field gradient on the induced dipole moment of a particle and surrounding fluid. The dielectrophoretic potential field experienced by a particle is of second order in the local electric field and is proportional to the difference between the particle and fluid polarizabilities. This transport mechanism is not solenoidal[9] and can therefore rarefy, concentrate, and trap particles. Dielectrophoresis is used for manipulating, fusing, sorting, and lysing biological cells[12, 4, 21, 14, 11, 22, 24]. In microsystems, it promises to provide these functions, again, using only applied electric fields.

Insulating post arrays are particularly interesting and technologically important among microchannel geometries. For fundamental studies, they provide well defined and controlled boundary conditions and are amenable to unit-cell analyses. In contrast, the study of flow in multiple-channel junctions where each leg of the junction connects to an independent reservoir and electrode is complicated by a number of physical effects that are mitigated within the interior of arrays. The current flowing through each channel depends on the surface state and area of the electrodes as well as the resistance of the channel from the electrode to the junction. Within an array this effect simply scales the flow field uniformly, but in a multiple-channel junction it can affect the current and fluid flux balance between channels. Furthermore, electrocapillary effects can induce pressure-driven flows that are sensitive to trace variations in surfactant concentrations and meniscus shapes in reservoirs. This effect is less complicated to mitigate in a two-port array than in a many-port system.

A uniform post array also provides a channel geometry in which fluid elements or suspended particles can repeatedly experience a flow field or transport phenomenon. By repetition, a small transport effect can be compounded into an appreciable or even dominant effect. Coherent, repeated dielectrophoretic forcing is shown to produce flowing filaments of highly concentrated and rarefied particles. Furthermore, the dispersion in passage time of fluid elements and particles through an array can be increased or reduced by adjusting how or whether the flow field repeats upon passage through the array. This ability has applications in fractionation, mixing, and filtration. Engineered

patterned arrays promise novel categories of devices and performance advances[31, 18] over the ubiquitous random packed bed in chemical processing and analysis.

The following sections outline the mathematical and physical description of electrokinesis and dielectrophoresis and present experimental observations of these phenomena. In combined electrokinetic and dielectrophoretic flows, three flow regimes are observed at low, moderate, and high applied electric fields[9]. These regimes are respectively labeled electrokinesis, filamentary dielectrophoresis, and trapping dielectrophoresis. The observed flow behavior is compared to simple theoretical models. Detailed measurements of electrokinetic flow fields agree well with computed ideal flow fields. Filaments of concentrated and rarefied particles are shown to align closely with ideal-flow streamlines, an observation that enables simplified models of filamentary dielectrophoresis. Finally, trapping dielectrophoresis is shown to concentrate and immobilize particles in dielectrophoretic traps. A simple superposition of electrokinetic and dielectrophoretic potential fields is shown to provide a reasonable estimate of the location and extent of these traps.

3.3 Electrostatically driven flow

Three different flow regimes typically exist for flows in which dielectrophoresis is combined with electrokinesis or advection. Dielectrophoresis is practically absent at the lowest applied fields. This particle flow regime is called simply “electrokinesis” or “advection,” depending on the dominant transport mechanism.

For particle flows at high Peclet number, dielectrophoresis begins to overcome diffusion and electrostatic repulsion above a threshold applied field, but cannot overcome advection and electrokinesis. Filaments of concentrated and rarefied particles appear along flow streamlines. This flow regime is called “filamentary dielectrophoresis.”

Above a higher threshold applied field, dielectrophoresis overwhelms advection and electrokinesis as well as diffusion and electrostatic repulsion. In this regime, particles are dielectrophoretically trapped and can be concentrated nearly to solid density. This regime is called “trapping dielectrophoresis.”

The following sections outline mathematical and physical descriptions of electrokinesis and dielectrophoresis.

3.3 Physics of electrokinesis

Electrokinesis is flow produced by the action of an electric field on a fluid having a net mobile charge. The flow of the charged fluid is often called electroosmosis and the flow of bodies suspended or solvated in the fluid is often called electrophoresis. These phenomena differ primarily by choice of reference frame and are both called electrokinesis.

A net charge generally appears at interfaces as a result of chemical reactions, adsorption, and other surface processes. A practical example is the interface of glass and water, in which the Si-O bonds on the surface react spontaneously with water to form Si-OH^- , immobilizing negative charges. The immobilized charges attract counterions in the fluid. If the surface charge is high, a large number of counterions are effectively bound ionically to the surface and are thus also immobilized. The bound counterions screen the surface charge, lowering the attractive electric field. When the attractive potential is comparable to the thermal energy of the counterions, Brownian collisions can dislodge the ions from stable positions near the surface. These ions are mobile and drift under the action of an applied electric field. The mobile ions induce electrokinesis as they exchange their drift momentum with the other molecules of the fluid.

The characteristic electrostatic potential of the mobile counterions is a function of both the surface and fluid composition, but ranges generally between $\pm 10kT$. This empirical potential, also

called the ζ potential is useful for calculating the electrokinetic mobility μ of the fluid,

$$\mu = \frac{\epsilon\zeta}{\rho\nu}. \quad (3.1)$$

The electrokinetic mobility of the surface is the negative of the electrokinetic mobility of the fluid.

In systems having inhomogeneous fluids and surfaces, electrokinesis is generally quite complicated. The computation of electrokinetic flows can involve the full unsteady species-transport equations (3.8) coupled to the Poisson (3.3), Navier-Stokes (3.6), and conduction (3.10) equations. Impressively nonlinear effects including “sample stacking” and “Teorell’s oscillations[34]” can be observed. However, many practical microfluidic devices are designed to operate with nearly uniform fluids and contain nominally uniform insulating surfaces. Electrodes are typically placed remotely in relatively large open reservoirs. Furthermore, the Debye length in most practical devices is much smaller than characteristic geometrical dimensions. Such systems closely approach the requirements for “ideal electrokinesis[7],” a dramatic simplification over general electrokinesis. Ideal electrokinesis is irrotational, with the flow velocity given by

$$\mathbf{u}(\mathbf{r}) = \mu\mathbf{E}(\mathbf{r}), \quad (3.2)$$

where the vector position \mathbf{r} appears explicitly to indicate the local flow velocity is proportional to the local electric field throughout the fluid. For ideal electrokinesis, it is sufficient for the electrokinetic mobility μ to be uniform for all surfaces within the system, the surfaces to be insulating and impervious, the Debye layer to be negligibly thin compared to channel geometrical length scales, the fluid to be uniform, the total pressure to be balanced on all entry and exit ports, and the inflow and outflow conditions to obey Eq. 3.2. Under these conditions, one may simply solve Laplace’s equation for the electrokinetic velocity potential. In many practical microsystems, the channel geometry is planar or quasi-planar. The electrokinetic flow in a planar geometry is purely two dimensional, another significant simplification used in the numerical modeling results presented later.

3.3 Physics of dielectrophoresis

Dielectrophoresis is particle motion caused by the action of an electric field gradient on an induced dipole moment of a particle and the fluid surrounding a particle[27, 19]. The dielectrophoretic force is of second order in the local electric field, so, unlike electrokinesis, dielectrophoresis is sensitive to the magnitude, not the sign, of the applied field. Thus dielectrophoresis can be and typically is driven by alternating electric fields. The results presented here employ a steady applied field.

Good analogies exist between dielectrophoresis and sedimentation in centrifugal fields. Particles that are more and less polarizable than the surrounding liquid have respectively a positive and negative dielectrophoretic mobility, just as particles that are less and more dense than the surrounding liquid have respectively a positive and negative buoyancy. The particles in this study have a positive dielectrophoretic mobility. Because of similitude between the electric and velocity fields, the electric field intensity and dynamic pressure field are proportional. The dielectrophoretic behavior in these flows can be intuited by the analogous behavior of bubbles in the dynamic pressure gradients of the same flow field, with viscosity scaled to match the relative drag force.

3.3 Continuum equations

The equations that describe electrostatically driven flow on continuum length scales are well known[34, 29, 27]. The relation between the electric potential, ϕ and the net charge density ρ_e in a fluid is given by the Poisson equation,

$$\nabla \cdot (\epsilon\nabla\phi) = \rho_e, \quad (3.3)$$

where ϵ is the dielectric constant of the fluid. The net charge density is

$$\rho_e = e \sum_i z_i c_i, \quad (3.4)$$

where the summation is over all ionic components including particulates, z_i and c_i are respectively the charge and concentration (number density) of the i th ionic component, and e is the unit electronic charge.

In an equilibrium balance between electrostatic drift and diffusion,

$$c_i = c_{i0} \exp\left(-\frac{e z_i \phi}{kT}\right), \quad (3.5)$$

where k is Boltzmann's constant, T is the temperature, and c_{i0} is the concentration at zero electric field. Combining Eqs. 3.3–3.5 produces the well known Poisson-Boltzmann equation that describes the electric field and charge density in an ionic fluid near a charged interface. The Poisson-Boltzmann equation has been analyzed extensively in a variety of interfacial geometries[37, 33]. Solutions of this equation show that an ionic fluid bears an appreciable net charge only in the region immediately adjacent to a charged interface. This region, also called the Debye layer, generally extends into the fluid $O(1\text{--}100)$ nm. The electrokinetic flow boundary layer coincides with the nanometer-scale Debye layer. Since microfabricated devices have length scales ranging from $1\text{ }\mu\text{m}$ to 10 mm , the relative thinness of the Debye layer facilitates matched asymptotic analyses of electrokinetic flow. In ideal electrokinesis, the Debye layer is assumed to be infinitesimally thin and is replaced by a slip boundary condition.

The incompressible momentum and continuity equations are respectively

$$\frac{\partial \mathbf{u}}{\partial t} + (\mathbf{u} \cdot \nabla) \mathbf{u} = -\frac{\nabla p}{\rho} + \nu \nabla^2 \mathbf{u} + \frac{\rho_e}{\rho} \mathbf{E}, \quad \text{and} \quad (3.6)$$

$$\nabla \cdot \mathbf{u} = 0, \quad (3.7)$$

where ρ is the fluid density, ν is the fluid kinematic viscosity, and $\mathbf{E} = \nabla \phi$ is the electric field. The electrostatic forcing term responsible for electrokinesis appears as a body force on the fluid. A dielectrophoretic term does not appear since in a system having a single-phase fluid, dielectrophoretic forcing, like gravity, affects only the hydrostatic pressure. Like fluid-level differences, differences in the dielectrophoretic force at compliant or free interfaces can generate a pressure-driven flow, but this behavior can be treated in the entry- and exit-pressure boundary conditions.

The flow systems studied contain a dilute suspension of solid particles and are not truly single-phase. In regions where dielectrophoresis concentrates or immobilizes these particles, the fluid viscosity, surface charge density, and even boundary location can be affected. These effects require attention to component-specific transport within the fluid via the equations

$$\frac{\partial c_i}{\partial t} + \nabla \cdot \mathbf{j}_i = 0, \quad (3.8)$$

where \mathbf{j}_i is the flux of the i th component of the fluid. When diffusion, advection, electrophoresis, and dielectrophoresis dominate transport, an empirical relation for \mathbf{j}_i is

$$\mathbf{j}_i = -D_i \nabla c_i + c_i [\mathbf{u} - \mu_i \mathbf{E} + \nu_i \nabla(\mathbf{E} \cdot \mathbf{E})], \quad (3.9)$$

where D_i is the effective diffusivity, μ_i is the electrophoretic mobility, and ν_i is the dielectrophoretic mobility of the i th component. The relation of μ_i and ν_i to the physical characteristics of the particles and ions has been studied extensively. In general, it has been found that the electrophoretic mobility of a particle that is large compared to the thickness of its Debye layer is independent of the size and shape of the particle[30, 25]. In contrast, the dielectrophoretic mobility increases as the square

of the particle size[27, 19]. Generally, the dielectrophoretic flux term of Eq. 3.8 is negligible for small molecules except within the Debye layer where electric field gradients can be $10^5 \text{ V}/\mu\text{m}^2$. Electric field gradients produced by photolithographically fabricated structures in microchannels are typically limited to $O(1 \text{ V}/\mu\text{m}^2)$ thus dielectrophoretic fluxes in microfabricated structures are typically appreciable only for larger molecules and particles larger than $O(10 \text{ nm})$.

Finally, charge and therefore electrical current is conserved within the fluid,

$$\nabla \cdot \mathbf{i} = 0, \quad (3.10)$$

where the current density \mathbf{i} is

$$\mathbf{i} = \epsilon \frac{\partial \mathbf{E}}{\partial t} + \mathbf{u} e \sum_i z_i c_i - e \sum_i D_i \nabla c_i - \mathbf{E} e \sum_i z_i \mu_i c_i. \quad (3.11)$$

The terms on the right side of Eq. 3.10 are the displacement, convection, diffusion, and conduction current from first to last. The coefficient of \mathbf{E} in the conduction term is fluid conductivity.

3.4 Experimental Apparatus

Figure 3.1 shows a diagram of the microflow experimental apparatus and micrographs of flow channels filled with post arrays etched in glass. The particle-image recording system is an inverted $10\times$ video epifluorescence microscope with a blue light-emitting diode ring illuminator. The RS-170 output of the video camera (Cohu 4910) is digitized to 8 bits by a frame grabber (Matrox Meteor) and recorded directly to computer disk. The images are interlaced at 640×480 -pixel resolution, with each interlaced field temporally separated by 16.7 ms.

The microfluidic circuit consists of a uniform post array isotropically etched in glass with a thermally bonded glass cover slip. Holes drilled in the cover provide access to the microchannels. The circuit is held in place using a 16-port test fixture having gold ring electrodes and 1-ml fluid reservoirs. The channels and reservoirs contain a uniform aqueous suspension of fluorescein-labeled 200-nm latex nanospheres with a carboxylate-modified surface (Molecular Probes, yellow-green fluospheres). The solution is buffered to pH 7.7 by 1-mM phosphate-buffered saline. Voltages are applied to the fixture electrodes via a regulated power supply (HP 6236B or SRS PS350).

Pressure-driven flow produced by liquid-level differences in the reservoirs and air currents above the reservoirs is carefully minimized. Measurements are taken within two hours of the first post-fabrication introduction of liquid to the microsystems.

The microchannels studied have uniform square arrays of square and circular posts at different angles with respect to the applied electric field. The channels are $\sim 10 \mu\text{m}$ deep. Velocity measurements of electrokinetic flow fields were obtained for square posts that are 104 and 142 μm on a side and circular posts that are 93 μm in diameter on 200 μm centers. Fluorescence images were taken of dielectrophoresis in arrays of square posts that are 36 μm on a side and circular posts that are 33 μm in diameter on 63- μm centers.

Cross-correlation particle-image velocimetry[35, 23, 6] provided single-pixel-resolution electrokinetic flow velocity fields from videos of 2,000 sequential 640×480 -pixel interlaced images. Figure 3.2 shows a typical raw particle image from a video.

The iterative image-processing procedure used to extract velocity measurements[6] employs continuous image-shifting optimizations. The maximum particle displacement per image delay is ~ 3 pixels ($\sim 150 \mu\text{m}/\text{s}$). Because the images are sequential, an additional optimization was performed in which up to 32 frames are skipped between correlation pairs so that the particle displacement between correlation pairs is 1–3 pixels. This optimization is performed independently for each velocity measurement so more frames are skipped in slow-moving regions of the flow than in fast-moving regions, significantly extending the range of velocities that can be measured accurately.

3.5 Results

Experiments were conducted to observe and quantify the three regimes of electrostatically driven flow: electrokinesis, filamentary dielectrophoresis, and trapping dielectrophoresis. The electrokinetic flow field is measured at high spatial resolution using particle image velocimetry and compared to the calculated two-dimensional ideal electrokinetic flow fields. Particle fluorescence images of dielectrophoretic flows are compared with calculated flow streamlines and dielectrophoretic trapping-potential fields.

3.5 Electrokinesis

Figures 3.3–3.7 show overlays of measured electrokinetic flow speed fields and calculated two-dimensional, ideal electrokinetic speed fields. The speed fields are presented in the form of a simulated interferogram. Lines of constant gray scale are contours of constant speed. The magnitude of the speed at any point can be estimated with reasonable accuracy by counting and interpolating fringes starting at the stagnation points toward the top and bottom of the posts.

The experimental data show $520\text{-}\mu\text{m}\times 390\text{-}\mu\text{m}$ -rectangular regions that are rotated so that the mean flows are from top to bottom. The data can be distinguished from the theoretical flow speed by its scatter and flow imperfections. The spatial resolution of the velocity measurements is $\sim 0.8\text{ }\mu\text{m}\times 0.8\text{ }\mu\text{m}$.

The agreement with theory is quite good in spite of manufacturing imperfections and the presence of agglomerated particles and surface contaminants. Flow-marking particles that agglomerate typically have abnormal surface charge and consequently have an abnormal electrokinetic mobility. These particles flow at different speeds from normal particles and can skew velocity measurements. A simple image-thresholding procedure mitigates the effect of these particles at the expense of measurement signal to noise. The synthetic interferograms in Figs. 3.3–3.7 sensitively display small variations in speed, revealing residual streaks of slightly skewed speed measurements from agglomerated particles. Contaminants, for example agglomerated particles stuck to channel surfaces, locally perturb the surface charge density, violating the conditions for ideal electrokinesis. The effect of these contaminants appears as relatively strong localized perturbations in the speed contours. The contaminants typically produce a jet or wake that persists at most a few channel depths along the flow. At the low Reynolds numbers in this study $O(10^{-1}\text{--}10^{-2})$ the flow rapidly recovers its irrotational nature following a perturbation. For this reason, one finds rotational electrokinetic flow in microsystems only in localized regions where the conditions for ideal electrokinesis are violated, provided the violation does not produce a global pressure-driven flow.

Figure 3.8 shows an image of the time-averaged particle fluorescence in a predominantly electrokinetic flow from top to bottom. The fluorescence intensity is proportional to the particle concentration. Agglomerated particles produce the weak bright streaks in the otherwise uniform concentration field between the columns. The slight rarefaction of particles along the stagnation streamlines is attributed to a weak dielectrophoretic effect resulting from the use of finite applied electric fields, since ideal electrokinesis does not produce concentration gradients.

3.5 Filamentary dielectrophoresis

Filamentary dielectrophoresis is observed when dielectrophoresis is strong enough to overwhelm diffusion and electrostatic repulsion, but not strong enough to overcome electrokinesis or advection[9]. Flowing filaments of nearly constant particle concentration follow streamlines. Significant concentration gradients can appear across streamlines. The nature of filamentary dielectrophoretic flow in arrays depends on the orientation of the the array with respect to the applied electric field. For example, Fig. 3.9 shows highly-concentrated filaments of particles flowing down the central streamlines

between posts when the electric field is oriented at 45° with respect to post columns. In contrast, Fig. 3.10 shows broader highly rarefied filaments flowing down columns of posts.

The relatively strong rarefaction of particles along post columns in Fig. 3.10 is the effect of coherent reinforcement of dielectrophoretic transport down repeated rows of posts, as evidenced by the flow at the start of the array shown in Fig. 3.11. The degree of coherent reinforcement is sensitive to the alignment of the applied field with the post columns. At the edges of the array in Fig. 3.11, the electric field lines are poorly aligned with the columns and the filaments are less pronounced than along the centerline of the array.

The nature of the dielectrophoretic filaments is also sensitive to post shape. Figure 3.12 shows the filamentary flow at the end of an array of circular posts. In this flow, apart from a slight rarefaction immediately near the stagnation streamline (also seen in Fig. ??, particles are concentrated along rows of posts, the opposite behavior of that in Fig. 3.10.

Figure 3.13 juxtaposes experimental particle fluorescence images with calculated streamlines and a spectral color map of the magnitude of the electric field. In the color map, red is zero field and blue is the highest field. The filaments are substantially aligned with the calculated electrokinetic flow streamlines.

3.5 Trapping dielectrophoresis

At relatively high applied fields, dielectrophoresis overcomes electrokinesis, advection, diffusion, and electrostatic repulsion to concentrate and trap particles. Figure 3.14 shows steady-state trapping dielectrophoresis. The zones of bright fluorescence contain particles that are concentrated to near solid density and relatively immobile. Weaker filamentary dielectrophoresis is also evident. In steady state, the traps are filled with particles to capacity, limited by the potential well depth and extent.

The shape and depth of the trapping potential well is generally affected by perturbations of the electrokinetic flow and viscosity by the partly and wholly immobilized particles and perturbations of the flow boundaries. However, a simple model of the trapping potential that neglects these complications captures the general nature of the trapped regions. The combined electrokinetic and dielectrophoretic potential[9], $\mu\phi - \nu(\mathbf{E} \cdot \mathbf{E})$, within an array of circular posts is overlaid in Fig. 3.14 as a simulated interferogram where fringes correspond to isopotentials. This simplified theory strictly applies before particle concentration gradients form. The regions on the lower left and right of the posts where fringes begin and end on the same post are a potential well for positive dielectrophoretic particles. Traps for negative dielectrophoretic particles also appear at the top and bottom of the post. The number of fringes in these potential wells shows that the depth of the negative dielectrophoretic trap is much smaller than that of the positive dielectrophoretic traps.

3.6 Conclusions

Three regimes of electrostatically driven particle transport in uniform insulating post arrays have been observed. At the lowest applied electric fields, electrokinesis is the dominant flow mechanism. The electrokinetic flows observed in the arrays agree well with calculations based on ideal electrokinesis. At moderate applied fields, dielectrophoresis, a transport phenomenon that is nonlinear in the applied electric field, begins to overwhelm diffusion and electrostatic repulsion between the colloiddally suspended particles. Filamentary dielectrophoresis is observed, characterized by flowing filaments of concentrated and rarefied particles that are closely aligned with flow streamlines. Gradients in particle concentration across the filaments can be large, but gradients along the filaments are small. At higher applied fields, trapping dielectrophoresis is observed as dielectrophoresis dominates other transport mechanisms. Particles become highly concentrated and immobilized in zones adjacent to posts. In steady state, the trapping zones are filled to capacity with particles, which locally perturb the surface charge density and viscosity, altering the electrokinetic mobility, and violating

the conditions for ideal electrokinesis. The trapped particles also change the effective shape of the posts. The proper numerical treatment of steady trapping dielectrophoresis is complicated and non-linear. However, linearly superimposing the unperturbed ideal electrokinetic and dielectrophoretic potentials produces the potential field experienced by particles before concentration gradients form. This unperturbed field can be used as a first estimate of the steady-state trapping-potential field.

Filamentary dielectrophoresis can be coherently reinforced within a patterned array of posts. The ability to amplify a transport process coherently within an array is novel and may enable microfluidic devices to out-perform conventional devices that employ random packed beds.

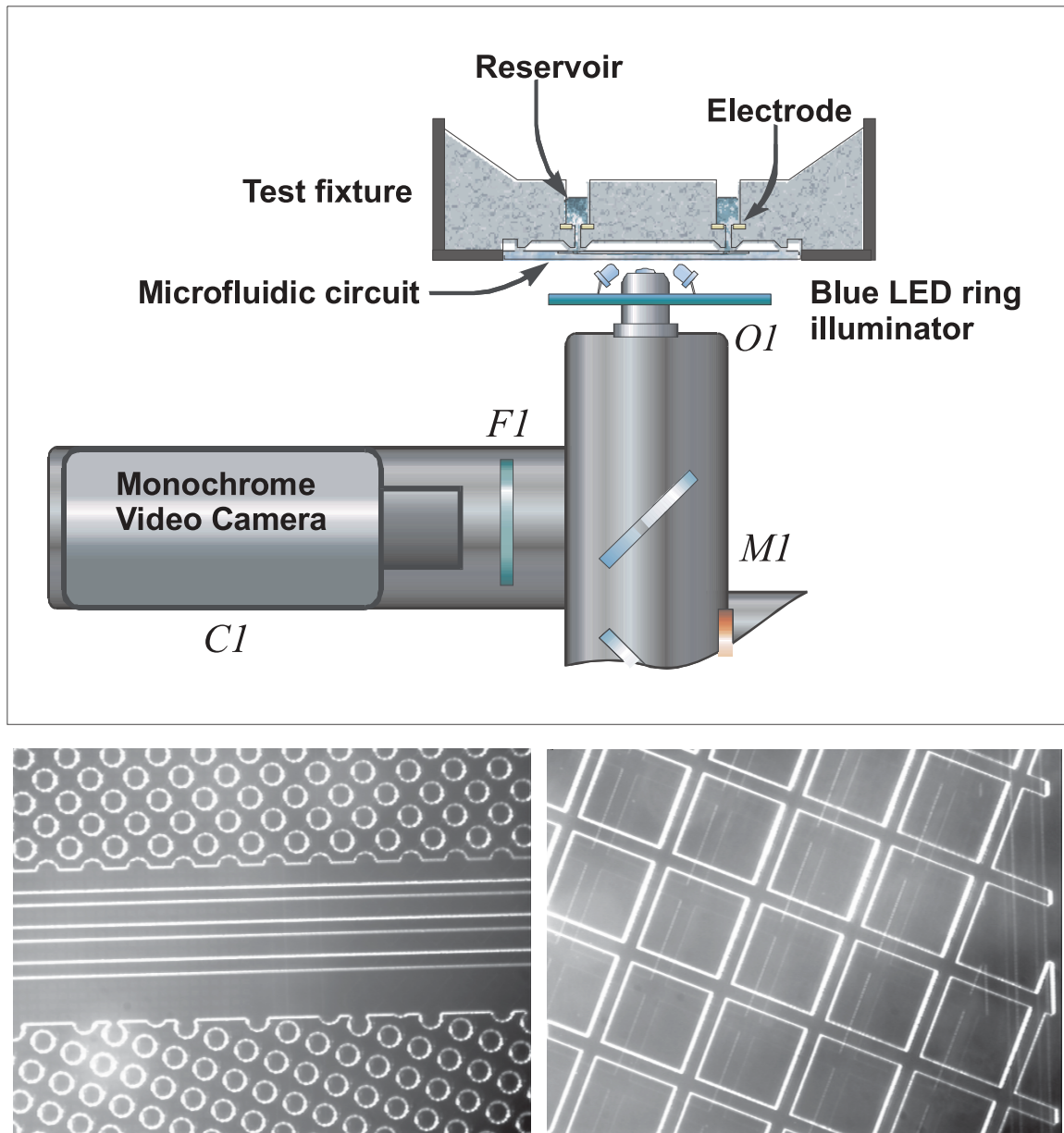


Figure 3.1: Diagram of the experimental apparatus for studying electrokinesis and dielectrophoresis in microarrays. Video from the inverted epifluorescence microscope is digitized and recorded to disk. The glass substrate containing the microfluidic channels is supported in a fixture combining a vacuum chuck, reservoirs, and electrodes. The optical micrographs show patterned glass microchannels used in this study.

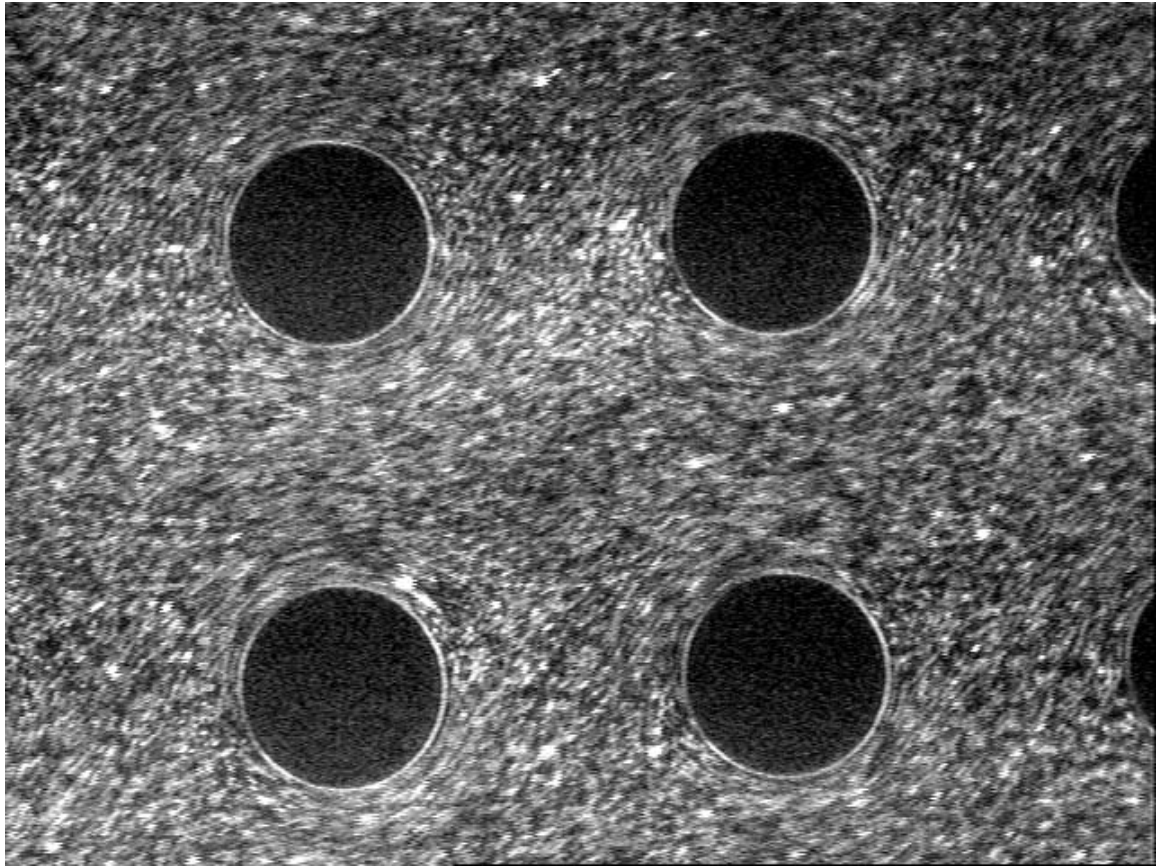


Figure 3.2: Raw experimental particle image used in the PIV analysis. The image spans a $520\text{-}\mu\text{m} \times 390\text{-}\mu\text{m}$ rectangle.

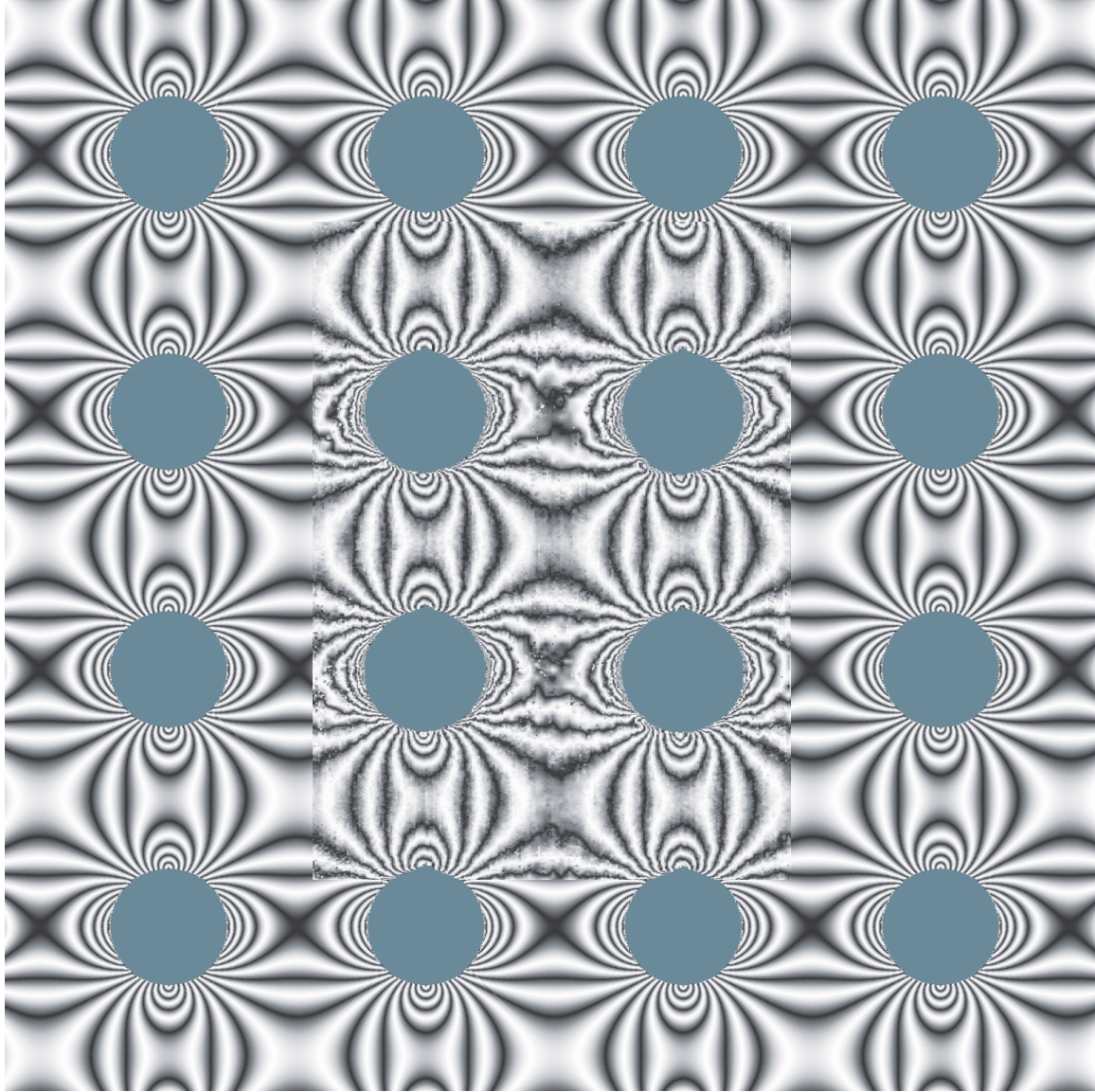


Figure 3.3: Overlay of experimental speed field on ideal electrokinetic speed field. The electric field of 2 V/mm is applied from top to bottom, oriented down columns of 93- μm circular posts on 200- μm centers. The fringe spacing is 24.5 $\mu\text{m/s}$. Experimental measurements occupy a rectangle that includes the central four circular posts. The measurements can be distinguished from the ideal flow by the presence of scatter and flow imperfections of order 2 $\mu\text{m/s}$.

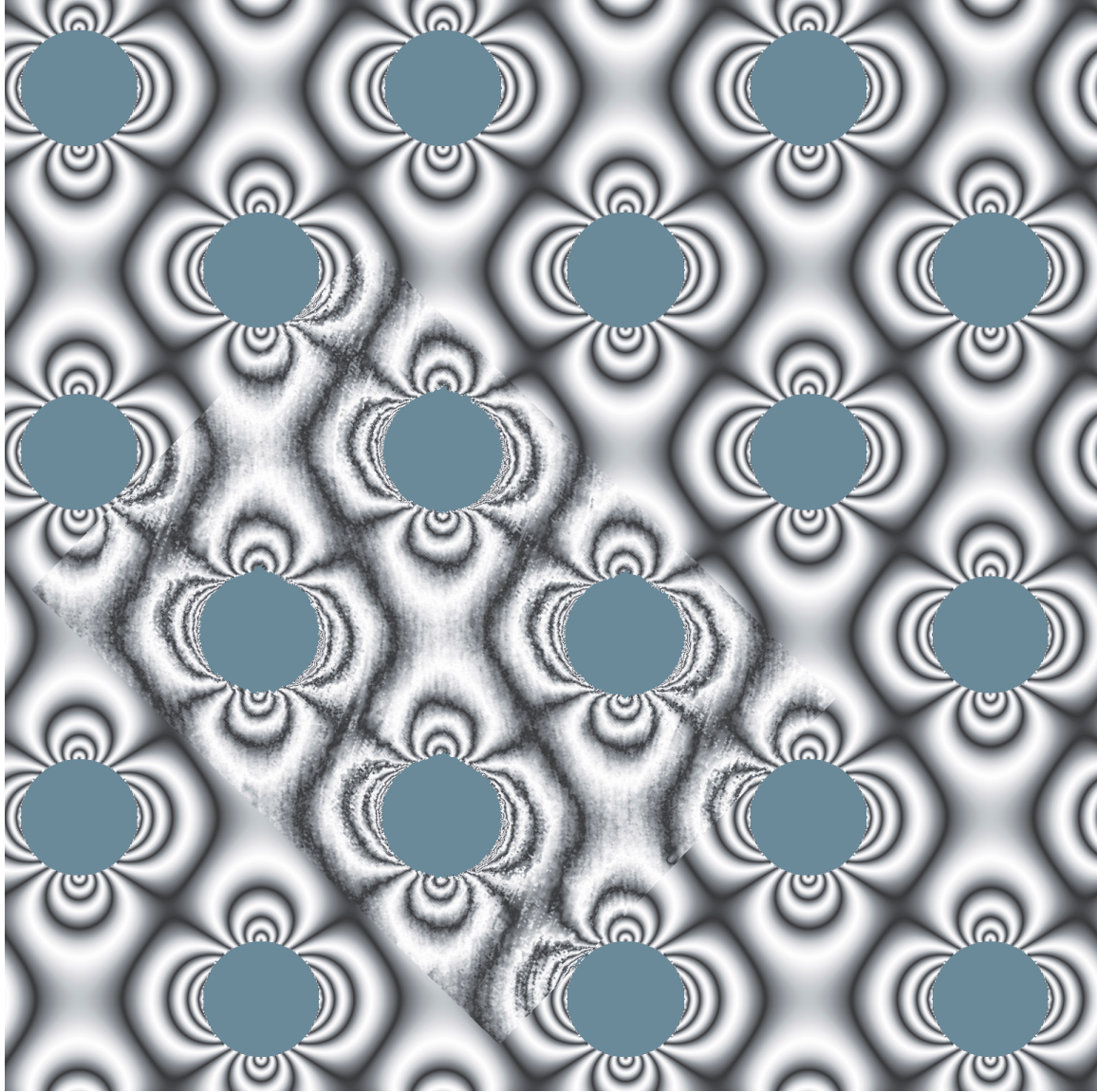


Figure 3.4: Overlay of experimental speed field on ideal electrokinetic speed field. The electric field of 2 V/mm is applied from top to bottom, oriented at 45° with respect to columns of $93\text{-}\mu\text{m}$ circular posts on $200\text{-}\mu\text{m}$ centers. The fringe spacing is $24.5\text{ }\mu\text{m/s}$. The rectangle containing experimental measurements is tilted by 45° toward the bottom left end of the image.

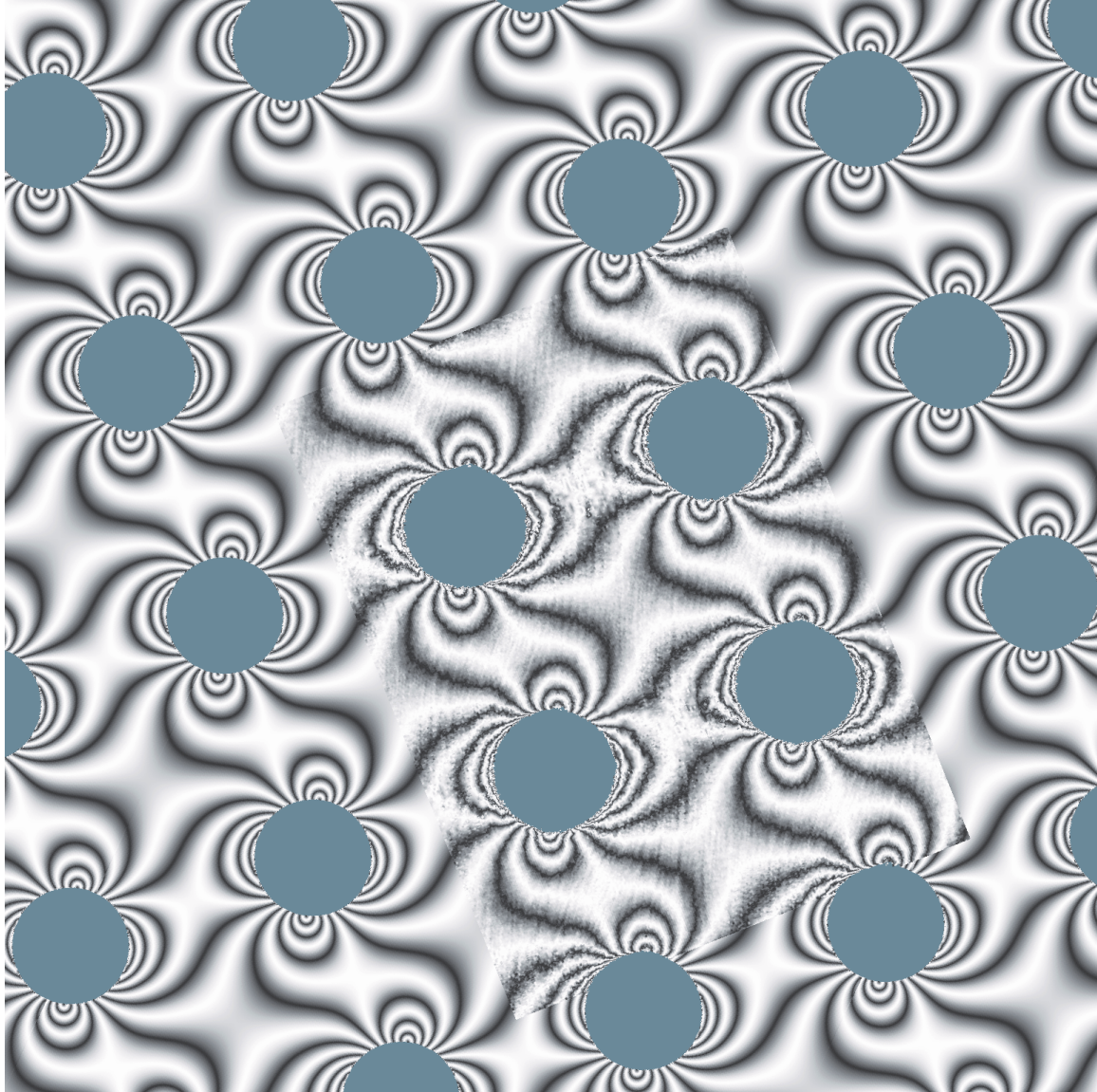


Figure 3.5: Overlay of experimental speed field on ideal electrokinetic speed field. The electric field of 2 V/mm is applied from top to bottom, oriented at 20° with respect to columns of $93\text{-}\mu\text{m}$ circular posts on $200\text{-}\mu\text{m}$ centers. The fringe spacing is $24.5\text{ }\mu\text{m/s}$.

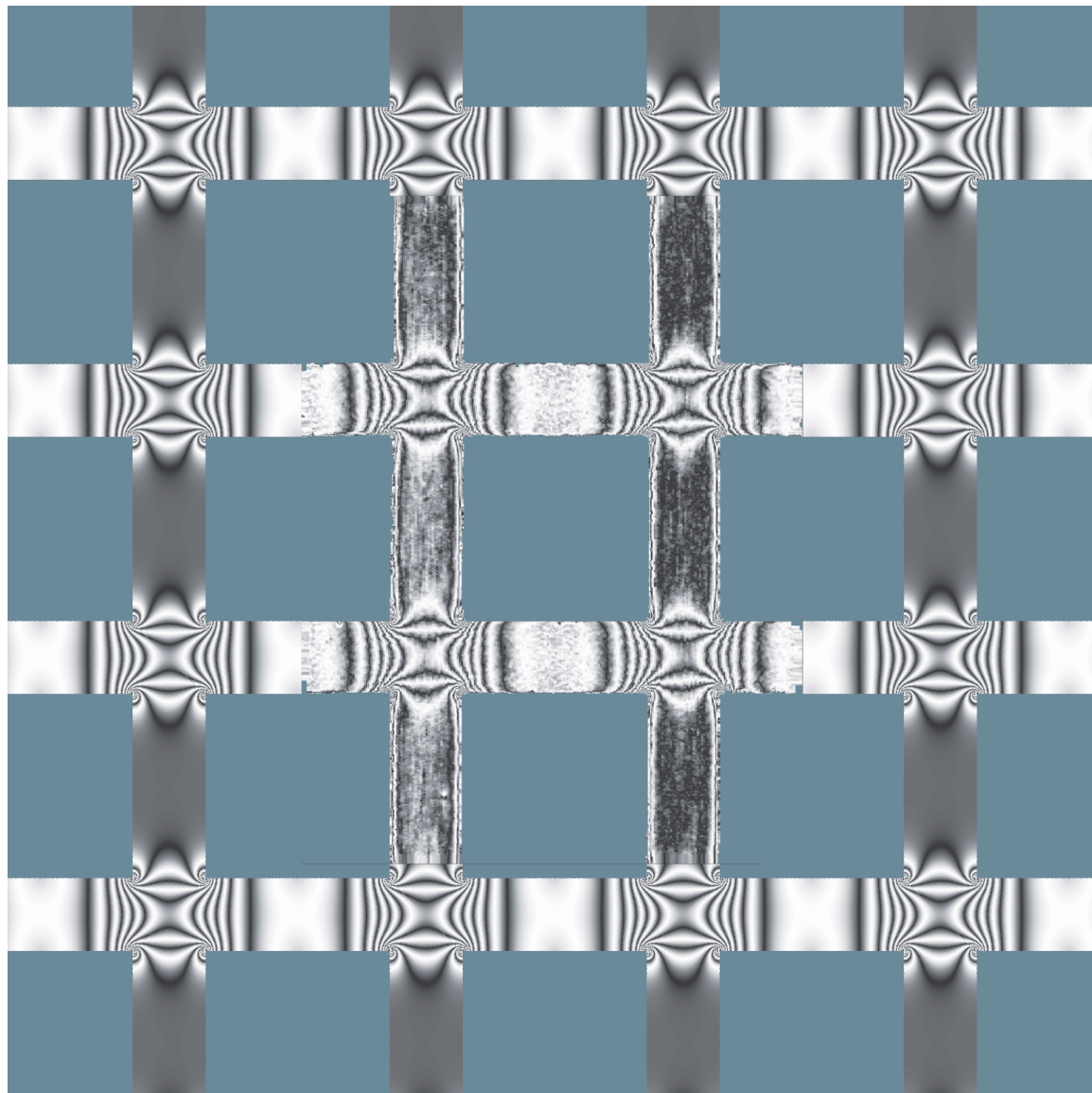


Figure 3.6: Overlay of experimental speed field on ideal electrokinetic speed field. The electric field of 1 V/mm is applied from top to bottom, oriented down columns of 142- μm square posts on 200- μm centers. The fringe spacing is 9.8 $\mu\text{m/s}$.

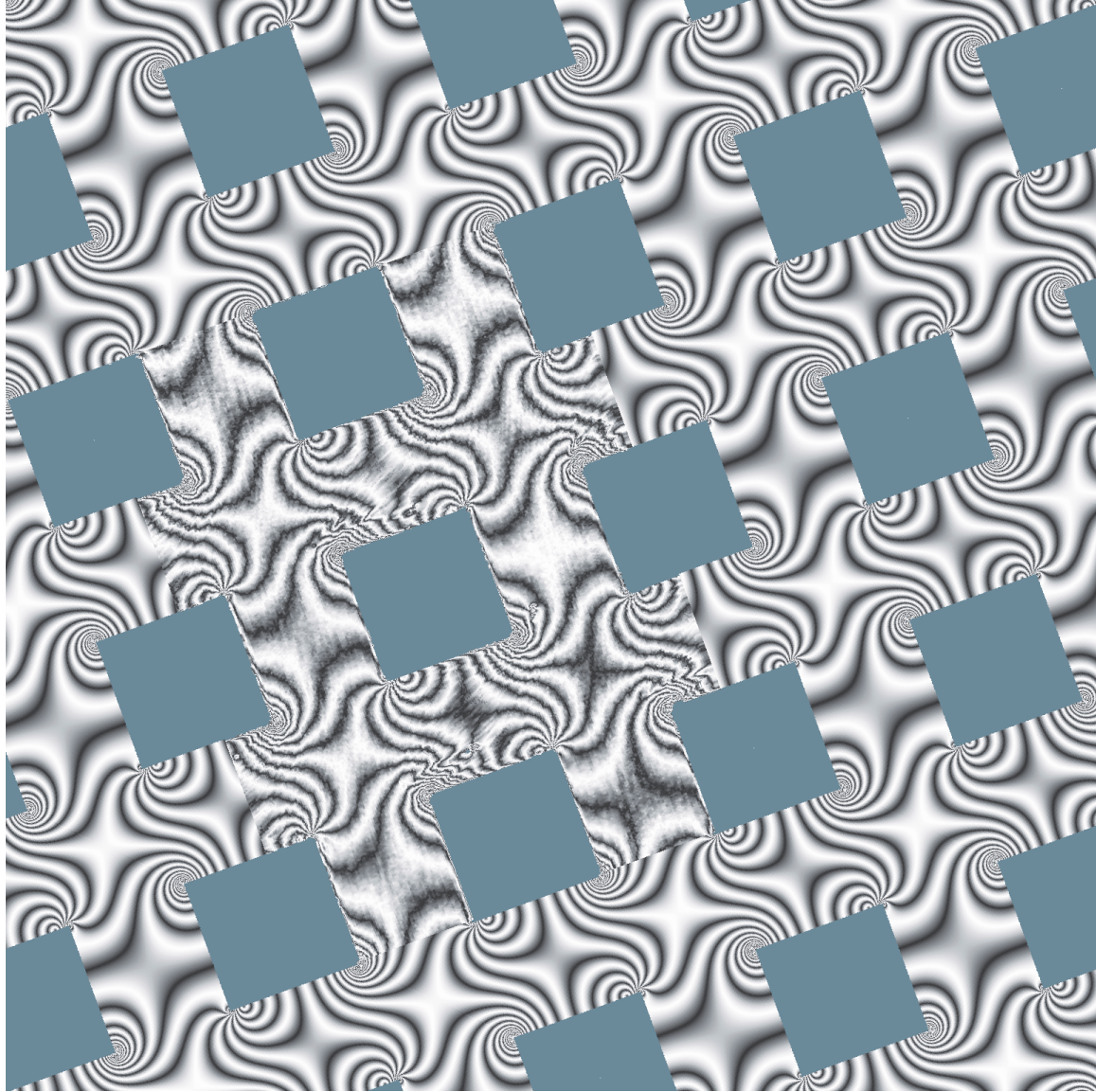


Figure 3.7: Overlay of experimental speed field on ideal electrokinetic speed field. The electric field of 1 V/mm is applied from top to bottom, oriented at 22° with respect to columns of $104\text{-}\mu\text{m}$ square posts on $200\text{-}\mu\text{m}$ centers. The fringe spacing is $4.9\text{ }\mu\text{m/s}$.

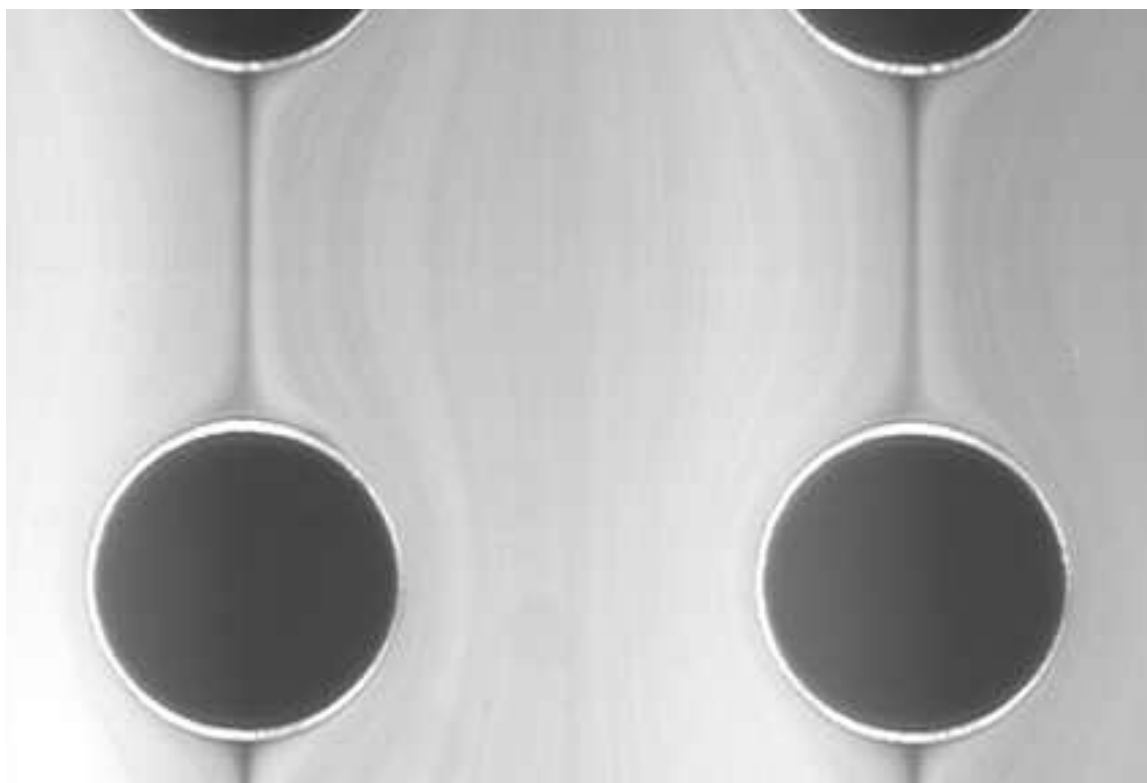


Figure 3.8: Time-averaged particle fluorescence image of a predominantly electrokinetic flow. The fluorescence intensity is proportional to particle concentration. The slight rarefaction at the stagnation streamline evidenced by the dark streak is apparently a weak filamentary dielectrophoretic effect.

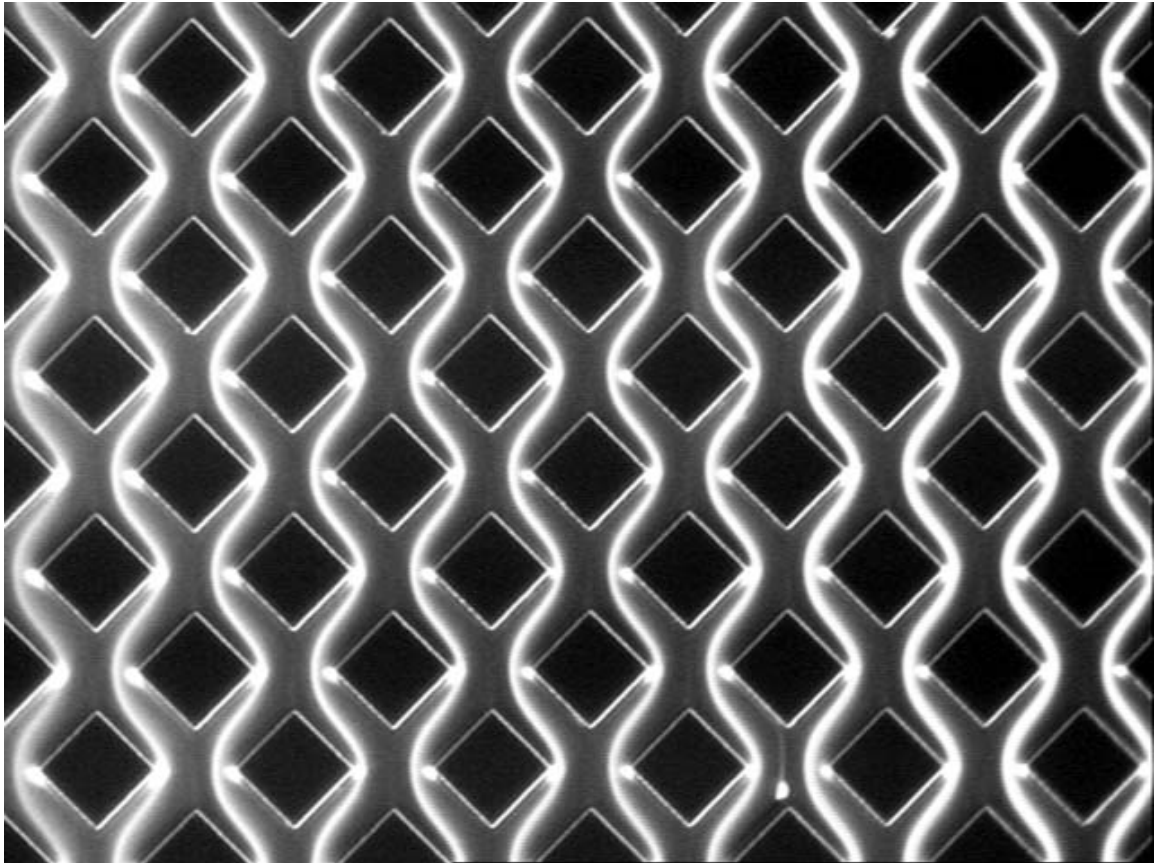


Figure 3.9: Particle fluorescence image of filamentary dielectrophoretic flow produced by an applied field of 80 V/mm from top to bottom, oriented at 45° with respect to columns of $36\text{-}\mu\text{m}$ square posts on $63\text{-}\mu\text{m}$ centers. The fluorescence intensity variation shows strong effects of dielectrophoretic concentration and rarefaction of particles.

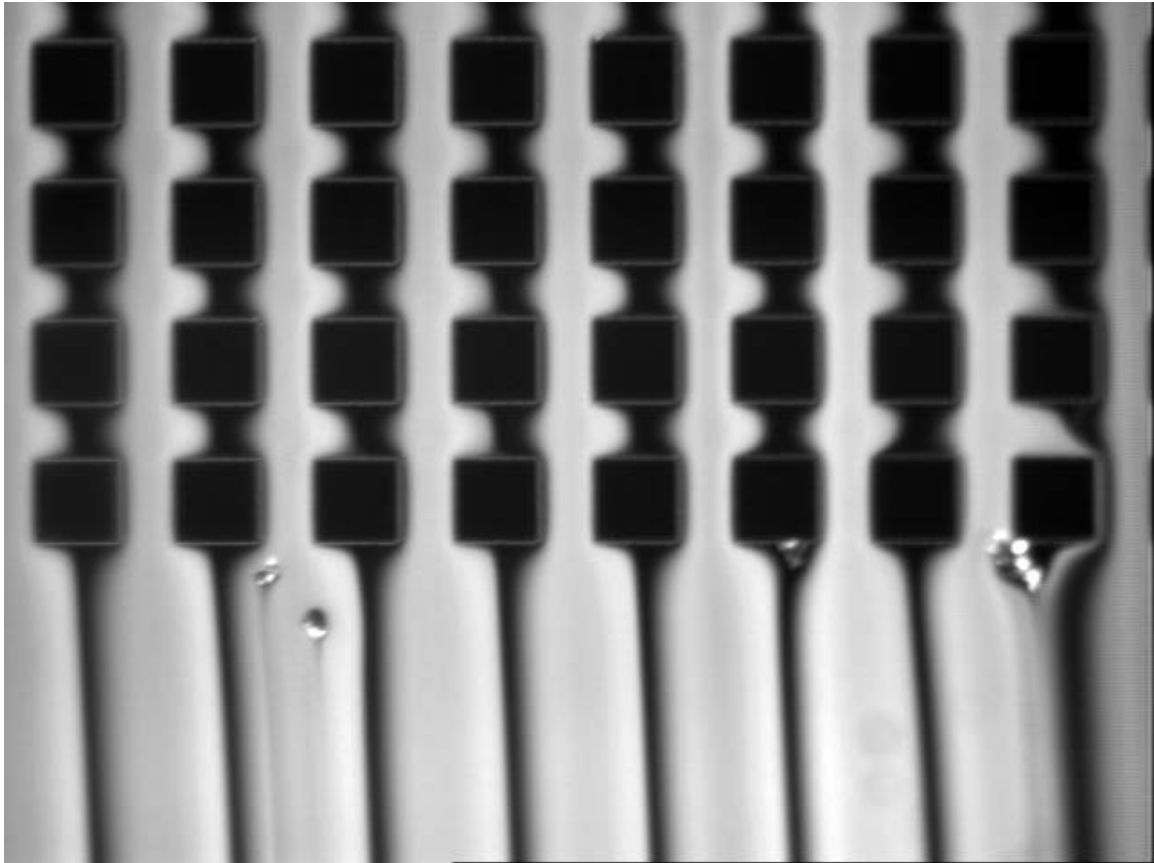


Figure 3.10: Particle fluorescence image of filamentary dielectrophoresis at the end of an array. The flow is from top to bottom produced by an applied field of 80 V/mm, oriented at $\sim 2^\circ$ with respect to columns of $36\text{-}\mu\text{m}$ square posts on $63\text{-}\mu\text{m}$ centers. Particles are significantly depleted along the post columns.

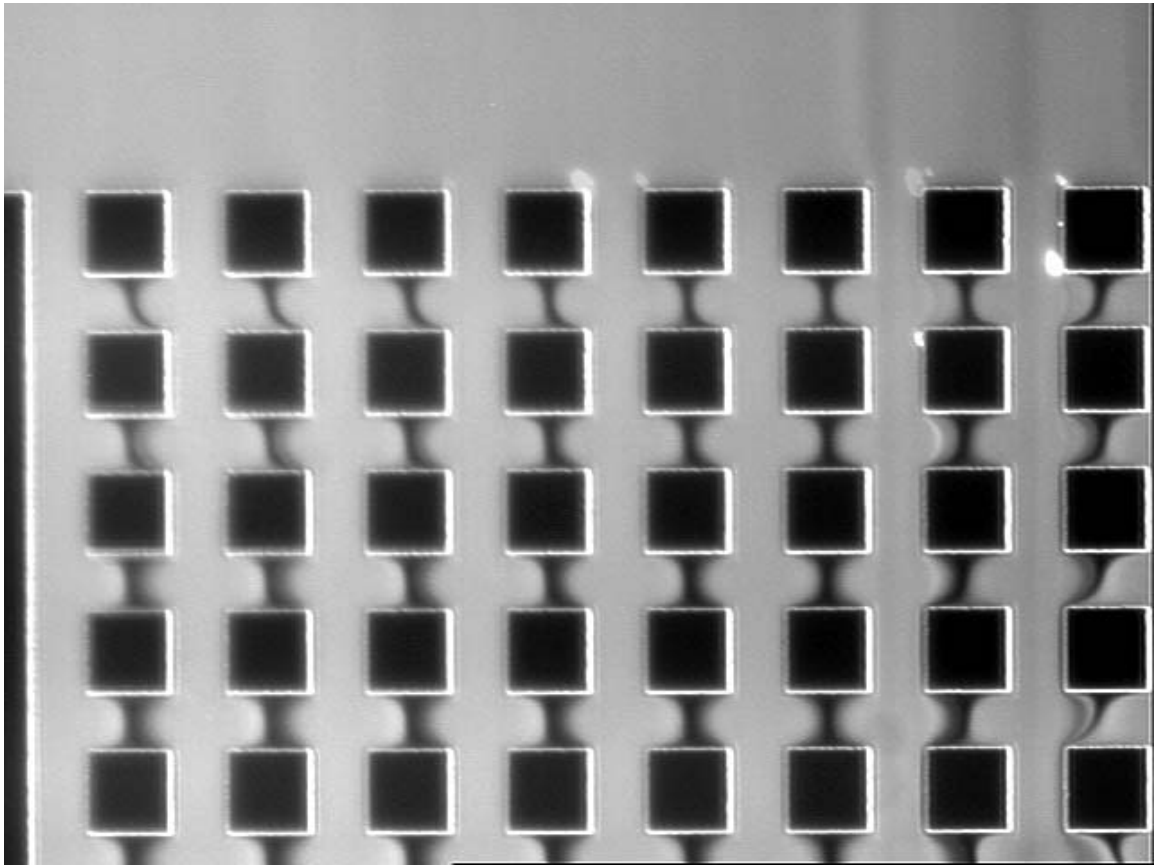


Figure 3.11: Particle fluorescence image of flow at the entrance of the square array in Fig. 3.10. The amount of rarefaction grows as the flow passes repeatedly past rows of posts.

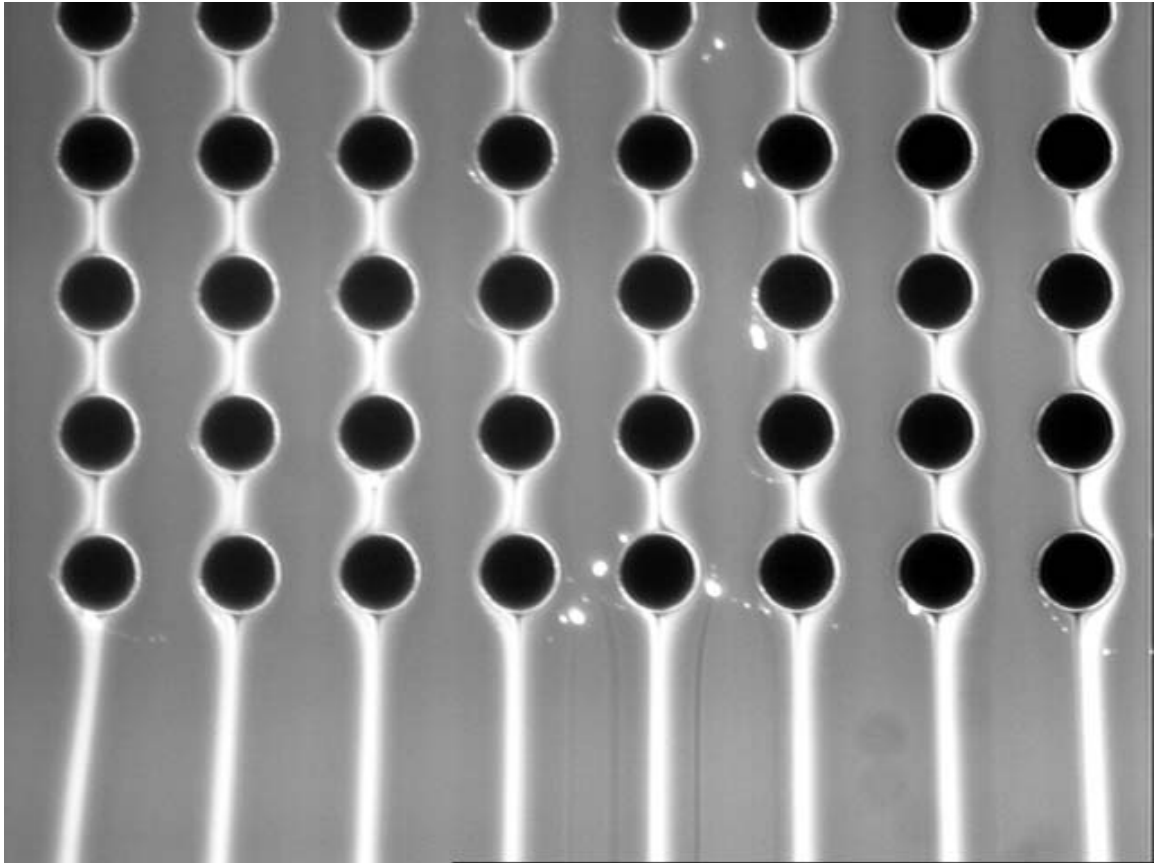


Figure 3.12: Particle fluorescence image of filamentary dielectrophoresis at the end of an array. The flow is from top to bottom produced by an applied field of 25 V/mm oriented down columns of 33- μm circular posts on 63- μm centers. The fluorescence intensity variation shows the dielectrophoretic concentration of particles in the region along the post columns.

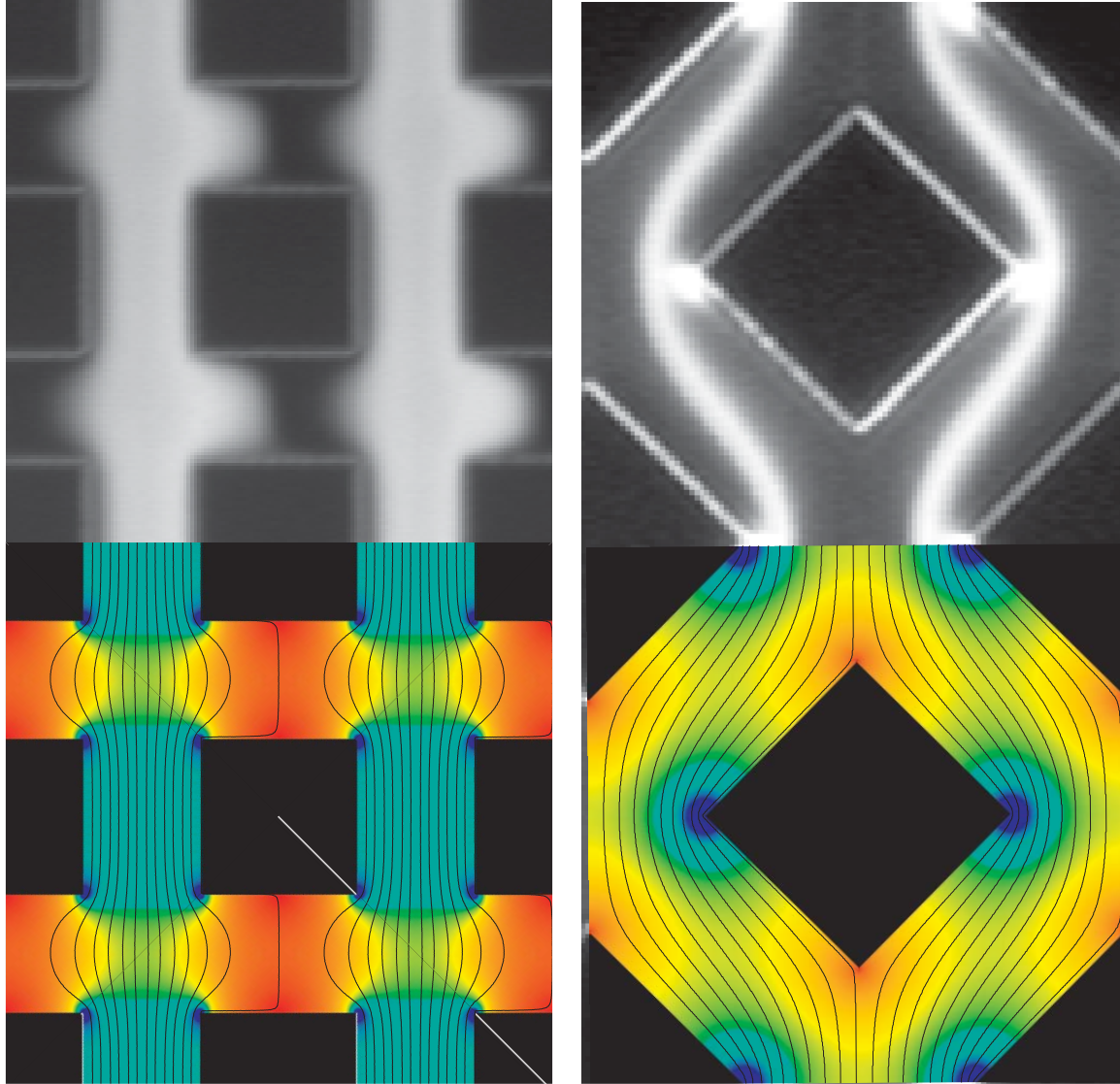


Figure 3.13: Particle fluorescence image and calculated ideal electrokinetic streamlines and electric field magnitude (indicated by a spectral color map: blue corresponds to high field). The concentration of filament is nearly constant along streamlines but varies significantly across streamlines.

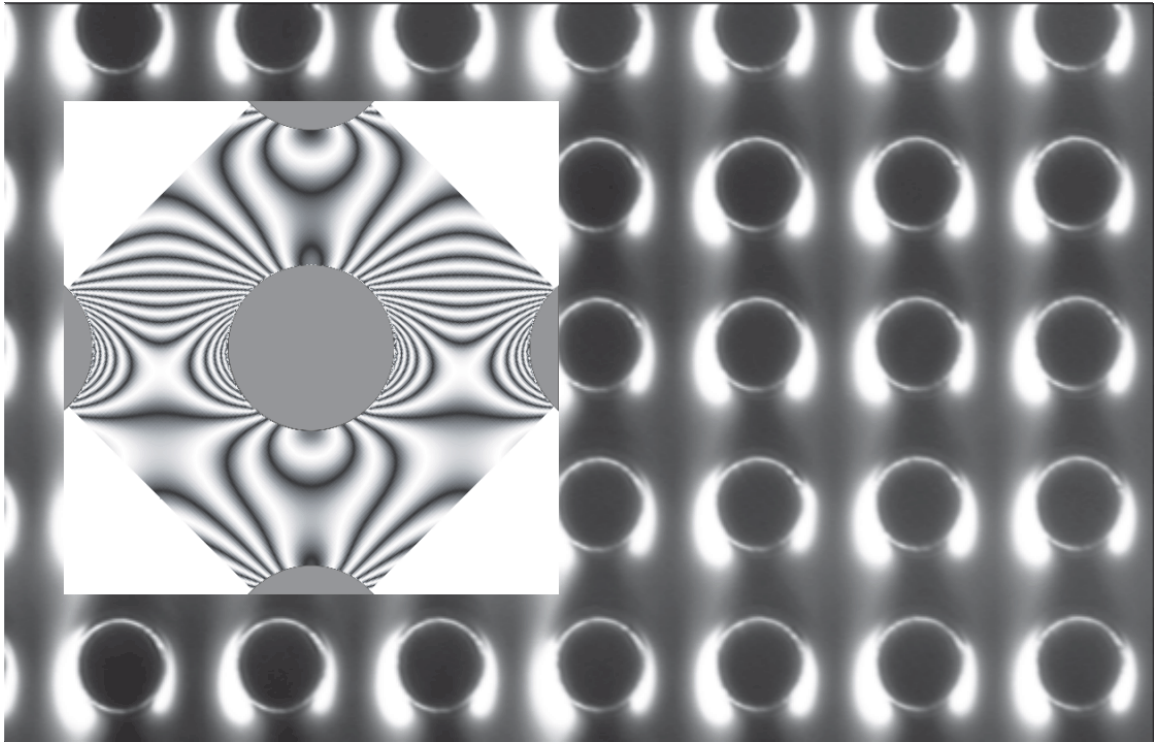


Figure 3.14: Particle fluorescence image of dielectrophoretic trapping. The flow is from top to bottom produced by an applied field of 100 V/mm down columns of $33\text{-}\mu\text{m}$ circular posts on $63\text{-}\mu\text{m}$ centers. Regions of trapped particles emit intense fluorescence. The overlaid image shows a simplified model of the potential experienced by particles. Regions where isopotentials curve back onto a post are dielectrophoretic traps.

This page intentionally contains only this sentence.

CHAPTER 4

A PIV methodology for high-resolution measurement of flow statistics

4.1 Abstract

Particle-image velocimetry (PIV) is a flow-diagnostic technique that provides velocity fields from a comparison of correlated images of particulate-laden flow. We have developed a PIV processing methodology that extracts measurements of the particle-displacement histogram from a flow video or ensemble of flow-image pairs. Single-pixel measurement of mean velocity can be obtained from an ensemble of $O(10^3)$ images. Measurements of higher-order moments of the velocity histogram require spatial averaging (i.e., lower spatial resolution), larger ensembles of images, or a combination of the two. We present single-pixel-resolution PIV measurements of a steady microflow and high-resolution measurements of the velocity histogram and two-point velocity correlations of a stationary turbulent flow. This methodology has applications in quantifying velocity statistics in other stochastic flows, e.g., bulk and near-wall boiling.

Nomenclature

- A amplitude parameter
- α, β semi-major and semi-minor axes of the elliptical Gaussian velocity histogram
- D effective particle diffusivity
- Δt time delay between subimages in correlation pair
- $\delta x, \delta y$ Cartesian independent variables of the filter basis function
- $\delta x', \delta y'$ independent variables of the filter basis function rotated into the frame of the eccentricity vector
- \mathbf{e} eccentricity vector of the elliptical Gaussian velocity histogram
- e_x, e_y Cartesian components of the eccentricity vector
- $\mathcal{P}\{\delta x, \delta y\}$ histogram of particle displacement (nonlinear filter basis function)
- σ mean half-width of the velocity histogram
- u, v Cartesian components of the electrokinetic velocity vector
- u_0, v_0 Cartesian components of the mean velocity vector

4.2 Introduction

Particle-image velocimetry (PIV) is a standard technique for quantifying flow-velocity fields. In PIV, the velocity field is measured by comparing the locations of particles or groups of particles in images of a particulate-laden flow. Often this comparison is performed using image-correlation techniques. In this article we report on extensions of the correlation-based PIV technique to obtain high measurement spatial resolution and the ability to measure single and multiple-point velocity statistics accurately and efficiently. These extensions employ ensemble averaging of correlations over a large number flow images. Correlation averaging in PIV is a relatively new procedure [23, 10, 6] which allows the experimentalist to trade between spatial resolution, temporal resolution, and signal-to-noise ratio (SNR) or measurement accuracy. This flexibility is particularly useful in microsystems, where the spatial resolution of flow images is limited by diffraction. We present single-pixel-resolution measurements of steady electrokinetic flow velocities in microchannels[8].

Correlation averaging can also be used to measure flow statistics in stationary¹, but unsteady, flows. We present single-pixel resolution measurements of velocity histograms at the mid-plane of a circular jet with co-flowing air at Reynolds number 6,100. The procedure of single-pixel correlation is particularly simple and minimizes issues of gradients within the subimage that can distort measurements. The disadvantage of single-pixel correlation is that a large number of flow images must be processed to obtain a useful SNR. For example, in a steady flow, 1024 image pairs must be processed to obtain a single-pixel correlation similar to a 32×32 -pixel subimage correlation of a single frame pair. A factor of 10–1000 more image pairs are required for measuring flow statistics in an unsteady flow. Fortunately, with a processing rate on a standard workstation of ~ 1 frame pair per second for a 1024×1024 -pixel image, ensembles of $O(10^4)$ and even $O(10^5)$ images are practical.

4.3 Processing procedure

The methodology used in this study to obtain high-resolution velocity histograms has been published elsewhere [6]. This methodology involves image pre-processing followed by an iterated sequence of cross correlation, correlation processing, nonlinear filtering to extract measurements, and measurement-grid refinement. The pre-processing phase minimizes sources of velocity bias by background subtraction, flat-field correction, etc. The cross correlation and correlation-processing steps are conducted as in standard PIV. However, the image auto-correlations are also calculated and ultimately used to deconvolve imaging defects, blur, and finite-particle-size effects from the correlations. Following the correlation processing, the correlation field can be related to a velocity histogram. By ensemble averaging over many image pairs, an accurate velocity histogram is constructed without the need for large amounts of spatial averaging in the form of large subimages. The method of single-pixel correlation is unconventional and will be discussed in the next section.

Flow measurements are extracted from these histograms via an optimal nonlinear filter. This filter is a nonlinear least-squares fit of the experimentally obtained histograms to a basis function of the filter having a number of adjustable parameters. The best-fit parameters are the measurements extracted from the histograms, e.g., mean velocity, variance, etc. The filter is optimal when the basis function of the filter properly matches the functional form of the histogram and its dependence upon the adjustable parameters. Different basis functions are presented to account for the different physics of the two flows in this study.

¹A stationary flow, which has constant *mean* properties, is distinct from a steady flow, which has constant *instantaneous* properties.

4.3 Single-pixel correlation

In PIV, image correlation is usually performed using the Fourier convolution theorem because of the computational speed of the fast Fourier transform. This transform adds an artificial velocity ambiguity, since it incorrectly treats the image data as spatially periodic. One means to remove this ambiguity by padding one of the subimages of a pair with null pixels to twice its original size in the row- and column-wise directions before convolving with the other subimage. The measurement resolution is limited by the size of the original un-padded subimage, i.e., measurements that are separated by one un-padded subimage size are independent. The size of the correlation field and hence velocity histogram is set by the size of the padded subimage. By using different amounts of padding, the measurement resolution and histogram width can be varied independently. Taking this procedure to a logical limit, it is possible to pad a single-pixel subimage to a desired histogram width and perform a “single-pixel correlation.”

The signal-to-noise ratio (SNR) of a single-pixel correlation from a single image pair is significantly less than unity and must be improved by ensemble averaging in order to obtain a useful measurement. Figure 4.1 shows the effect of averaging on 16×16 -pixel velocity histogram measurements obtained from single-pixel subimages of a turbulent flow. The curves show the histogram of $u - u_0$ at $v = v_0$, where u and v are respectively the row- and column-wise velocities and the subscript ‘0’ denotes the mean value. The top family of curves was measured from a low-turbulence region. The 10^3 - and 10^4 -image-pair averaged histograms are similar, implying the histogram has converged acceptably at 10^3 averages, analogous to using $\sim 32 \times 32$ -pixel subimages in a single-frame-pair correlation. The 10^2 - and 10^3 -frame-pair averages have significant differences and the 10-frame-pair and single-frame-pair histograms are completely invalid. The family of histogram measurements at the bottom of Fig. 4.1 was measured from a relatively turbulent region of the same flow. The 10^3 - and 10^4 -frame-pair averages are significantly different, indicating the need for $> 10^3$ image pairs for performing such measurements in turbulent regions.

The use of a single-pixel subimage eliminates issues of velocity gradients across the subimage and allows the full measurement resolution permitted by the imaging system to be realized. Furthermore the single-pixel correlation procedure degenerates to multiplying each pixel of the second subimage by the value of the single pixel, a computationally and algorithmically efficient procedure.

4.3 Multiple-point correlations

Multiple-point velocity fluctuation correlations provide a statistical measure of the coherence length scale of turbulent eddies. To date these correlations have been obtained only by the use of multiple time-correlated single-point measurements and have been of limited utility because of the limited amount of data about a flow that is practical to obtain using this serial technique. We have developed and implemented an algorithm for quantifying multiple-point correlations that employs correlation averaging similar to that described earlier. Instead of averaging the cross correlation of subimages from an ensemble of image pairs, the results of a correlation (or correlations) between the cross correlations of a “reference” and one (or more) “comparison” subimages are averaged. This has been implemented as a procedure several steps. For a two-point correlation between a single reference subimage and a range of comparison subimages, these steps are:

1. Select a reference subimage. The velocity within this subimage will be correlated with subimages in the rest of the image or within a selected range from the reference subimage.
2. Set the current image pair to the first image pair in the data set.
3. Clear (initialize with zero values) the two-point correlation arrays of all comparison subimages.
4. Cross correlate the reference subimage in the current image pair.

5. Deconvolve this cross correlation by the average autocorrelation of the subimage. Note that if the signal-to-noise ratio of the image is not sufficiently high, the autocorrelation must be first filtered to remove the strong noise coherence spike at the origin.
6. Reset the index that enumerates the current comparison subimage.
7. Cross correlate the indexed comparison subimage.
8. Deconvolve this cross correlation by the average autocorrelations of the subimage, again, with proper attention to avoid any noise spike at the origin of the autocorrelation.
9. Cross correlate the resulting correlations for the reference and comparison subimages, producing a double correlation.
10. Add this correlation to the two-point correlation array of the current comparison subimage.
11. If not done with the last comparison subimage, increment the comparison subimage index and go to step 7; otherwise continue.
12. If not finished with the last image pair in the data set, advance to the next image pair and go to step 4; otherwise continue.
13. The two point correlation is complete for all comparison subimages. Perform additional normalization by the single-point correlations, if desired.
14. Process the resulting correlations using a nonlinear filter to extract measurements, if desired.

The computational burden of performing this double correlation for a single reference subimage is practically the same as that for cross-correlating and deconvolving all of the comparison subimages. Thus, this algorithm does not scale favorably for systematically performing two point correlations from each subimage in a flow to each other subimage. Moreover, the data storage requirements for such a procedure also scale poorly. However, this technique does provide a unique method of quantifying the spatial coherence behavior of flows.

4.4 Steady electrokinetic flow in uniform post arrays

Electrokinesis is the flow produced by the action of an electric field on a fluid or immersed particle having a net mobile charge. Net charges appear within the nanoscopic Debye layer of many liquid/solid interfaces, e.g., water/glass, water/alumina and on many particles in solution, e.g., DNA. This flow achieves significance at the microscale and is of considerable practical importance in microfluidics, since it is a mechanism for manipulating particles and conveying fluids in microsystems using only an applied electric field. The flow rate is linear in the applied field. Furthermore, electrokinetic flow in systems with uniform insulating surfaces and uniform solutions is irrotational with a velocity field everywhere proportional to the electric field. Diffraction-limited, single-pixel-resolution optical diagnostics are often marginal for detailing electrokinesis in real microsystems. The systems chosen for this study are microchannels packed with uniform arrays of posts. Flow in such arrays is amenable to analysis and potentially useful for chemical and particle separations.

4.4 Basis function for the nonlinear filter

The basis function of the nonlinear filter is derived assuming the flow is uniform from the top of the channel to the bottom, as in ideal electroosmosis in a planar system [7]. All marker particles are assumed to have the same electrokinetic mobility and diffusivity. The electrokinetic velocity distribution in the absence of diffusion is a delta function at the mean-flow velocity. When diffusion

is present, the velocity distribution spreads into a Gaussian shape. The basis function used in the nonlinear filter is

$$\mathcal{P}\{\delta x, \delta y\} = A \exp \left(- [\delta x - u \Delta t]^2 + \frac{[\delta y - v \Delta t]^2}{D \Delta t} \right), \quad (4.1)$$

where $\mathcal{P}\{\delta x, \delta y\}$ is the histogram of particle displacement through $(\delta x, \delta y)$, A is an amplitude scale that can vary across the image. The parameters u and v are the mean electrokinetic velocity components in the row-wise and column-wise directions and D is the effective diffusion coefficient of the particles. The time delay between frames, Δt , can also vary across the image as a result of optimizations. Parameters A and D can only take positive values. This range is ensured by using their logarithms in the external parameter set adjusted by the nonlinear filter. Thus the adjustable parameters of the basis function are u , v , $\log(A)$, and $\log(D)$. The particle diffusivity D is practically constant across the flow. The value of this parameter is initially allowed to be adjusted by the nonlinear filter. The diffusivity field is then fixed at the mean value obtained from the filter in the initial measurement. Thus the filter is given three degrees of freedom: u , v , and $\log(A)$. If the assumptions made in the development of this basis function are rigorously valid and there are no additional complications, such as pressure-driven flow, the filter is optimal. In reality, there are variations in the electrokinetic mobility of the particles that elongate the particle-displacement histogram in the direction of the mean displacement, among other complications. Nevertheless, this basis function usually performs well and has the advantage of simplicity.

4.4 Experimental apparatus

Figure 4.2, the same as Fig. 3.1 in the previous chapter, is repeated here for convenience. This figure shows a diagram of the microflow experimental apparatus and micrographs of flow channels filled with post arrays etched in glass. The particle-image recording system in the electrokinetic flow experiments is an inverted 10 \times video epifluorescence microscope with a blue light-emitting diode ring illuminator. The RS-170 output of the video camera (Cohu 4910) is digitized to 8 bits by a frame grabber (Matrox Meteor) and recorded directly to computer disk. The images are interlaced at 640 \times 480-pixel resolution, with each interlaced field temporally separated by 16.7 ms.

The microfluidic circuit consists of a uniform post array isotropically etched in glass with a thermally bonded glass cover slip. Holes drilled in the cover provide access to the microchannels. The circuit is held in place using a 16-port test fixture having gold ring electrodes and 1-ml fluid reservoirs. The channels and reservoirs contain a uniform aqueous suspension of fluorescein-labeled 200-nm latex nanospheres with a carboxylate-modified surface (Molecular Probes, yellow-green fluospheres). The solution is buffered to pH 7.7 by 1-mM phosphate-buffered saline. Voltages are applied to the fixture electrodes via a regulated power supply (HP 6236B or SRS PS350).

The microchannels studied have uniform square arrays of square and circular posts at different angles with respect to the applied electric field. The channels are $\sim 10 \mu\text{m}$ deep. The square posts are 142 μm on a side on 200 μm centers. The circular posts are 93 μm in diameter on 200 μm centers.

Care was taken to eliminate pressure-driven flow produced by liquid-level differences in the reservoirs and air currents above the reservoirs. Applied electric fields were kept low enough to avoid particle dielectrophoresis.

4.4 Results

Videos of 2,000 sequential interlaced images with 640 \times 480 pixels were processed to obtain independent speed measurements at each image pixel. Figure 3.2 in the previous chapter shows a typical raw particle image from a video. The maximum particle displacement per image delay is ~ 3 pixels ($\sim 150 \mu\text{m/s}$). Because the images are sequential, an additional optimization was performed

in which up to 32 frames are skipped between correlation pairs so that the particle displacement between correlation pairs is 1–3 pixels [6]. This optimization is performed independently for each velocity measurement, so more frames are skipped in slow-moving regions of the flow than in fast-moving regions, significantly extending the range over which velocities can be measured accurately. Figures 4.3–4.6 show measured electrokinetic flow fields. The flow fields are presented in the form of a simulated interferogram. Lines of constant gray scale are contours of constant field. The magnitude of the field at any point can be estimated with reasonable accuracy by counting and interpolating fringes.

Figure 4.3 shows the measured speed field in a circular post array oriented at 45° with respect to the applied field of 2 V/mm. The flow is from the lower left to the upper right. The fringe spacing is $24.5 \mu\text{m/s}$. The speed field throughout the flow can be inferred by counting fringes starting from zero at the stagnation regions in the lower-left and upper-right surfaces of the posts. The streaking patterns that cross the fringes are produced by agglomerated particles having an abnormal surface charge and consequently moving slower or faster than the others. These streaks, which follow flow streamlines, can be eliminated by thresholding the video images to remove the contributions from particles that are significantly brighter than the average particle. In the measurements shown, the threshold was set to retain some streaking in the image and provide more context for understanding the flow from the figures.

Figure 4.4 shows flow in a similar array of circular posts oriented at 22.5° with respect to the applied field of 2 V/mm.

Figure 4.5 shows u , the row-directed component of the velocity in an array of square posts with channels that are aligned with the electric field of 1 V/mm applied from left to right. The flow slows as it expands into a junction and accelerates as it leaves the junction. The inset expanded image shows the resolution of the flow measurements in the upper right junction. The size of a pixel is indicated by the white square toward the lower right of the inset image.

Figure 4.6 shows the speed field in an array of square posts at 45° with respect to the applied electric field. The expanded image shown in the inset shows how well the technique works at resolving the speed increase in the region of the sharp post tip. The blemish in the speed field evident in the upper-right channel is real, produced most likely by a localized surface contaminant.

4.5 Stationary turbulent circular jet

Experimental studies of turbulent flows are often conducted for validating numerical submodels and codes. Conventionally, point-measurement techniques like laser-Doppler or hot-wire anemometry are used to obtain turbulent velocity histograms, while imaging techniques like particle-image velocimetry are used to obtain “snapshot” measurements of a flow. While spatial scanning can improve the utility of point measurements, the lack of flow context for the measurements and the typical sparseness of the data can be serious shortcomings. While repetition can improve the utility of snap-shot imaging techniques, spatial resolution is often a shortcoming. Furthermore, it is generally unclear how to present experimental results based on a limited number of snap-shots in a format that is suitable for quantitative model validation.

Image-correlation processing and averaging can be used to obtain velocity correlations and statistics with high spatial resolution. The conventional method of obtaining velocity statistics by particle-image velocimetry is to make independent velocity measurements from a large number of image pairs [13, 20]. This method requires the use of large subimages for correlation to obtain reliable velocity estimates for each image pair. Each image-pair contributes the (estimated) most-probable velocity within the subimage to the histogram. Unfortunately, if a range of velocities is present within the subimage, e.g. if the subimage does not resolve a small-scale turbulent eddy, the information about the velocity distribution other than the most-probable velocity is discarded. Thus the velocity field should be uniform across a subimage, significantly limiting the range of turbulent length scales that

can be properly probed. In contrast, the image-correlation processing and averaging methodology used in this experimental study superimposes estimates from each image pair of the complete velocity distribution within the subimage. The signal-to-noise ratio (SNR) of each individual estimate can be well below unity, since the SNR of the distribution increases as the square root of the number of image pairs in the ensemble. Small, even single-pixel, subimages can be used in the correlation, provided the ensemble is sufficiently large. Furthermore, if multiple-pixel subimages are used, all velocities within the subimage contribute in the correct proportion to the histogram. Thus the velocity-distribution measurement is valid provided only that the flow statistics are uniform across the subimage.

4.5 Basis function for the nonlinear filter

Unlike the previous basis function, there is no simple general form of a turbulent velocity histogram. However, it was observed that the velocity distributions measured in the jet appeared to have a single peak with an ellipsoidal Gaussian flavor. The eccentricity, orientation, and length of the minor axis of the peak varies throughout the flow. A basis function was chosen to quantify these parameters for comparison with existing data and numerical models. The basis function is

$$\mathcal{P}\{\delta x, \delta y\} = A \exp \left(- \left[\frac{\delta x' - u_0 \Delta t}{\alpha \Delta t} \right]^2 - \left[\frac{\delta y' - v_0 \Delta t}{\beta \Delta t} \right]^2 \right), \quad (4.2)$$

where, u_0 and v_0 are the mean velocity components in the x - and y -directions, respectively, and

$$\alpha \equiv \sigma + \|\mathbf{e}\|, \quad (4.3)$$

$$\beta \equiv \sigma^2 / (\sigma + \|\mathbf{e}\|). \quad (4.4)$$

The parameters α and β are the lengths of the semi-major and semi-minor axes of the ellipse. These parameters are derived from σ , the effective half-width of the Gaussian ellipse, and the modulus of the eccentricity vector, \mathbf{e} , of the ellipse. The variables $\delta x'$ and $\delta y'$ are derived from δx and δy and \mathbf{e} via

$$\delta x' \equiv \frac{e_x \delta x + e_y \delta y}{\|\mathbf{e}\|}, \quad \text{and} \quad (4.5)$$

$$\delta y' \equiv \frac{e_y \delta x - e_x \delta y}{\|\mathbf{e}\|}, \quad (4.6)$$

where e_x and e_y are the components of the eccentricity vector in the x - and y -directions, respectively. Again, parameters that can range from $(0, \infty)$, i.e., A and σ , are mapped to external parameters that can range from $(-\infty, \infty)$ by taking logarithms. This mapping reduces stiffness and other difficulties with the numerical filter. The external parameters of the basis function are $\log(A)$, u_0 , v_0 , $\log(\sigma)$, e_x , and e_y . The external parameters of the same function may be expressed in a variety of different ways, e.g., in polar rather than Cartesian coordinates. However, the numerical implementation of the optimal nonlinear filter is more robust with this choice of parametrization than others that were attempted.

4.5 Experimental apparatus

The turbulent flow that was studied consists of an axisymmetric, central air jet surrounded by a low-velocity co-flowing air stream. The central jet tube has a 5.3-mm inside diameter and a 6.8-mm outer diameter. The straight jet tube is 1-m long, which ensures a fully-developed turbulent pipe flow velocity distribution at the jet exit. The outer co-flowing air stream has a 75-mm outer diameter, and passes through a honeycomb section to produce a uniform laminar flow.

The central-jet bulk velocity is 18.2 m/s, giving a Reynolds number based on the jet exit diameter of 6,100. The co-flowing air velocity is 0.96 m/s. Bulk velocity of the fuel jet was determined from the measured volumetric flow rates and the internal area of the jet nozzle. The gas-flow rate of the central jet and the co-flow are metered by mass-flow controllers to an accuracy of 2%.

The PIV system uses the output of a double-pulsed Nd:YAG laser (Spectra Physics PIV-400, 400 mJ/pulse at 532 nm) to illuminate seed particles added to the flow. The beam is formed into a 75-mm high laser sheet approximately 250- μ m thick by cylindrical optics and subsequently passed through the test section. Mie-scattered light from the seed particles is collected by a 105-mm focal length, f2.8 camera lens and detected using a CCD video camera with a 1024 \times 1024-pixel array (TSI Model 630045 Cross-correlation Camera). Particle images illuminated by the two laser pulses are recorded on sequential video frames using a frame-straddle technique. The particle displacement between a pair of images is ~ 10 pixels at the maximum velocity. The field of view of the images is 49 \times 49 mm, providing a resolution of 48 μ m/pixel. A 10-nm bandwidth interference filter centered at the laser wavelength of 532 nm placed in front of the collection lens eliminates background room light.

Seed particles in the both the fuel jet and co-flowing air were supplied by a fluidized-bed seeder. The seed particles are nominally-300-nm ceramic Zeeospheres manufactured by the 3M Corporation. Calculations show that this size is sufficiently small for the particles to accurately follow the gas flow at the flow conditions studied. Cyclone separators located downstream of the seeders remove particle agglomerates and improve the particle-size uniformity.

4.5 Results

An ensemble of 14,500 image pairs of this turbulent flow was processed to obtain independent velocity histograms at 8 \times 8-pixel and single-pixel resolutions. The mean speed fields measured at the lower and higher spatial resolution are shown in Figs. 4.7 and 4.8, respectively. The peak speed is ~ 18.2 m/s or ~ 10 pixels per frame at the base of the jet. The correlation window size in the single-pixel analysis is 8 \times 8 pixels, allowing velocity fluctuations of ± 4 pixels per image delay to be recorded.

Figure 4.9 shows the variance and peak-correlation-amplitude fields across the flow. As expected, the variance is largest at the edge of the base of the jet. The potential core of the jet disappears about two exit-diameters downstream of the nozzle. The peak correlation amplitude decreases by an order of magnitude from the ambient air to the center of the jet because of the combined effect of the higher variance and increased out-of-plane particle motion in the jet.

Figure 4.10 shows the components e_x and e_y of the eccentricity vector, \mathbf{e} , where the x - and y -directions are aligned with the rows and columns, respectively. The full scales of the variation of these parameters is less than a pixel in these measurements, i.e., the ellipsoidal correlation peak is elongated by less than a complete pixel. The measurement could be made less noisy by using a longer time delay between images at the cost of spatial resolution or by using a larger ensemble of images at the cost of increased processing and experiment duration.

The eccentricity fields in Fig. 4.10 contain a systematic error. Figures 4.7 and 4.8 show that the mean-velocity gradients at the base of the jet are too large for the approximation of uniform properties across an 8 \times 8-pixel subimage made in deriving the filter basis function (4.2). A velocity gradient across the subimage appears as an artificially increased eccentricity vector in the direction of the mean flow. To remove this artifice, the analyst could either use smaller subimages at the expense of SNR, revise the filter basis function to accommodate velocity gradients, or post-process the eccentricity field using the measured velocity field. The post-processing procedure is possible because of the simple form of the velocity-gradient effect on eccentricity vector and variance measurements.

Figure 4.11 shows color maps of the width of the two point correlation peak from different reference subimages. The reference subimage is located at the center of the red spot in each image,

corresponding to the correlation-peak-width minimum. This is an indication that the reference subimage is most strongly correlated with itself, as expected. The dip in the correlation width that is apparent in the region surrounding the reference image shows that the flow loses spatial coherence over a finite and even sizable region. Moreover, this procedure quantifies this zone of partial coherence, allowing comparison with simulations. The zone of partial coherence can be intuited as a measure of the effective “shape” of turbulent eddies in a region.

4.6 Conclusions

Particle image velocimetry can be applied to obtain high-spatial-resolution and high-accuracy velocity statistics of stationary but not necessarily steady flows. Accurate single-pixel-resolution velocity measurements of a steady flow can be made by ensemble averaging the correlations of $O(10^3)$ image pairs. Accurate measurements of velocity histograms can be made of a turbulent flow given a data set with $O(10^4\text{--}10^5)$ images, with the lower and upper range sufficient for 8×8 -pixel and single-pixel subimages, respectively. The storage and processing requirements for this size of data set are no longer prohibitive or particularly challenging. A more-serious problem is the need to maintain a stationary flow for $O(10)$ hours to record the image set using standard high-resolution PIV cameras which can typically record only $O(1)$ image-pair per second. Given the ability to make single-pixel measurements, experimentalists may reconsider the need for megapixel and multi-megapixel cameras with relatively low data throughput.

The statistical measurement capabilities of PIV could be used to study other flow phenomena having a strong stochastic component, such as boiling and natural and forced convection. Snapshot PIV has been applied to develop an understanding of the role of vortex and jet motion on wall heat transfer [28]. Statistical PIV methods promise to extend this understanding and provide data in a format suitable for computational model validation.

The potential for sub-micrometer resolution of velocity histograms makes it possible to study these phenomena at the microscale, providing a new window into fundamental heat-transfer. The need for particle seeding can be troublesome for some boiling studies, since particles serve as bubble nucleation sites and can thus perturb the flow behavior. However, the seeding density, size distribution, and hydrophilicity of the particle markers can be tailored to mimic those of particles that are intrinsic to a practical boiling system. Commercially available fluorescent latex microspheres that we have tested are not stable at the atmospheric boiling point of water, thus either Mie-scattering particles or improved fluorescent markers may need to be employed.

Finally, multiple-point correlation fields have been measured using a correlation-averaging technique, providing a clear window into flow coherence that had previously only been viewed through the keyhole of point measurements. A similar double-correlation methodology can be generally employed to measure components of the velocity gradient tensor.

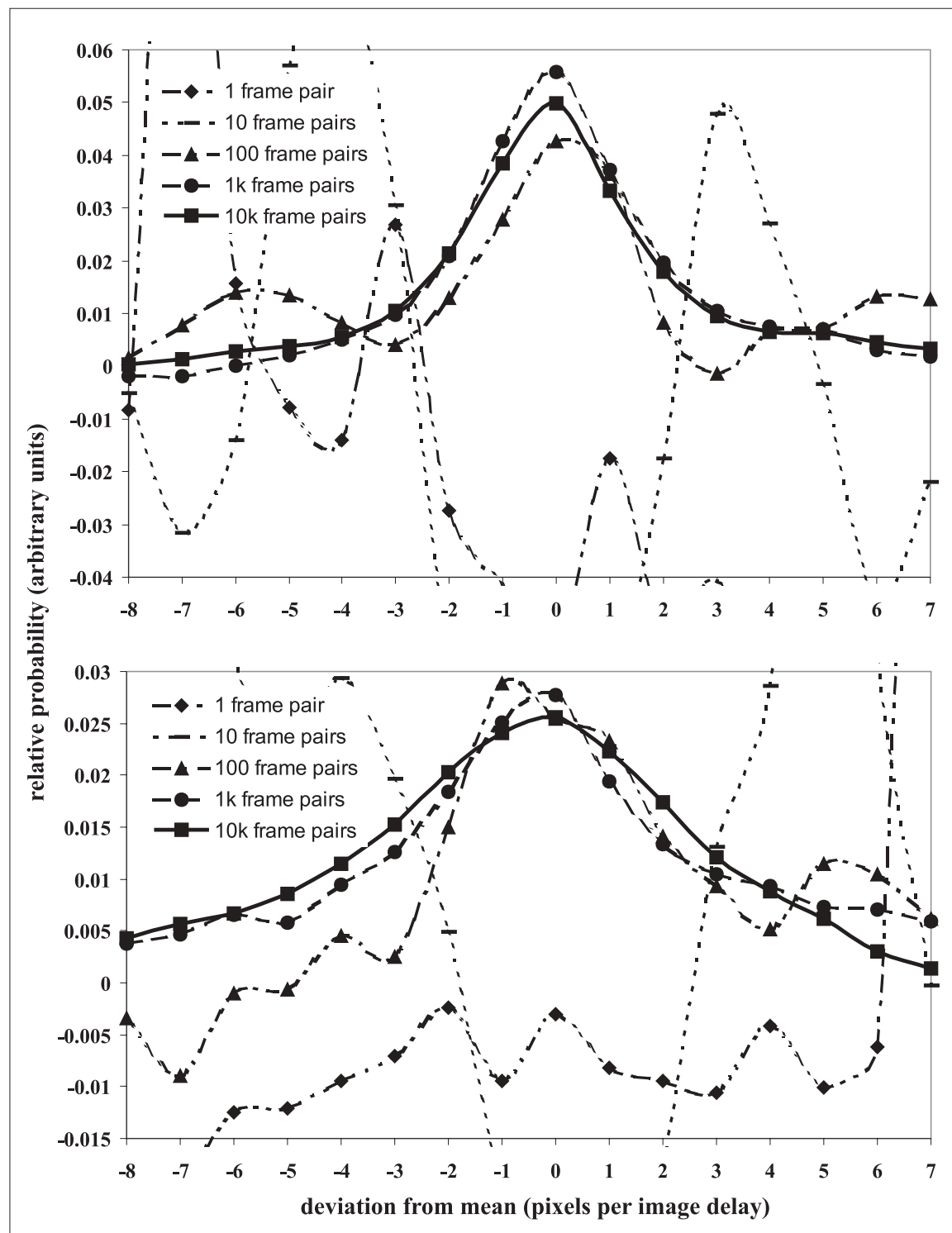
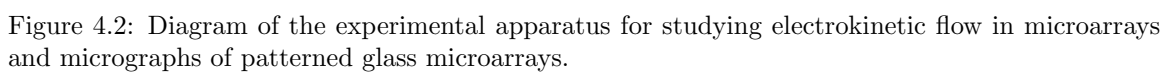


Figure 4.1: Experimentally measured velocity histograms from single-pixel subimages in a turbulent flow vs. the number of frame-pair correlations. The curves at the top and bottom were obtained in low- and high-turbulence regions, respectively.



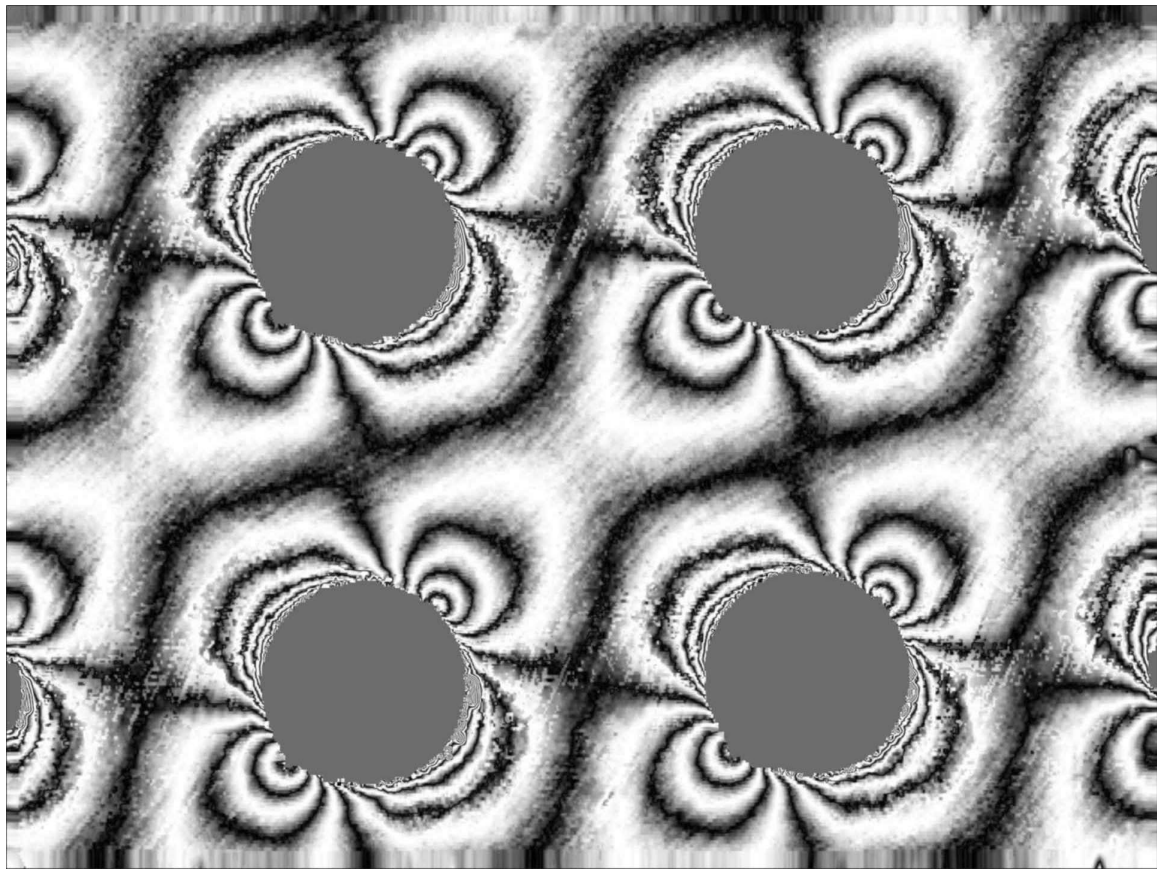


Figure 4.3: Electrokinetic speed field within an array of circular posts at 45° with respect to the applied electric field. The fringe spacing is 0.5 pixels per image delay ($24.5 \mu\text{m/s}$).

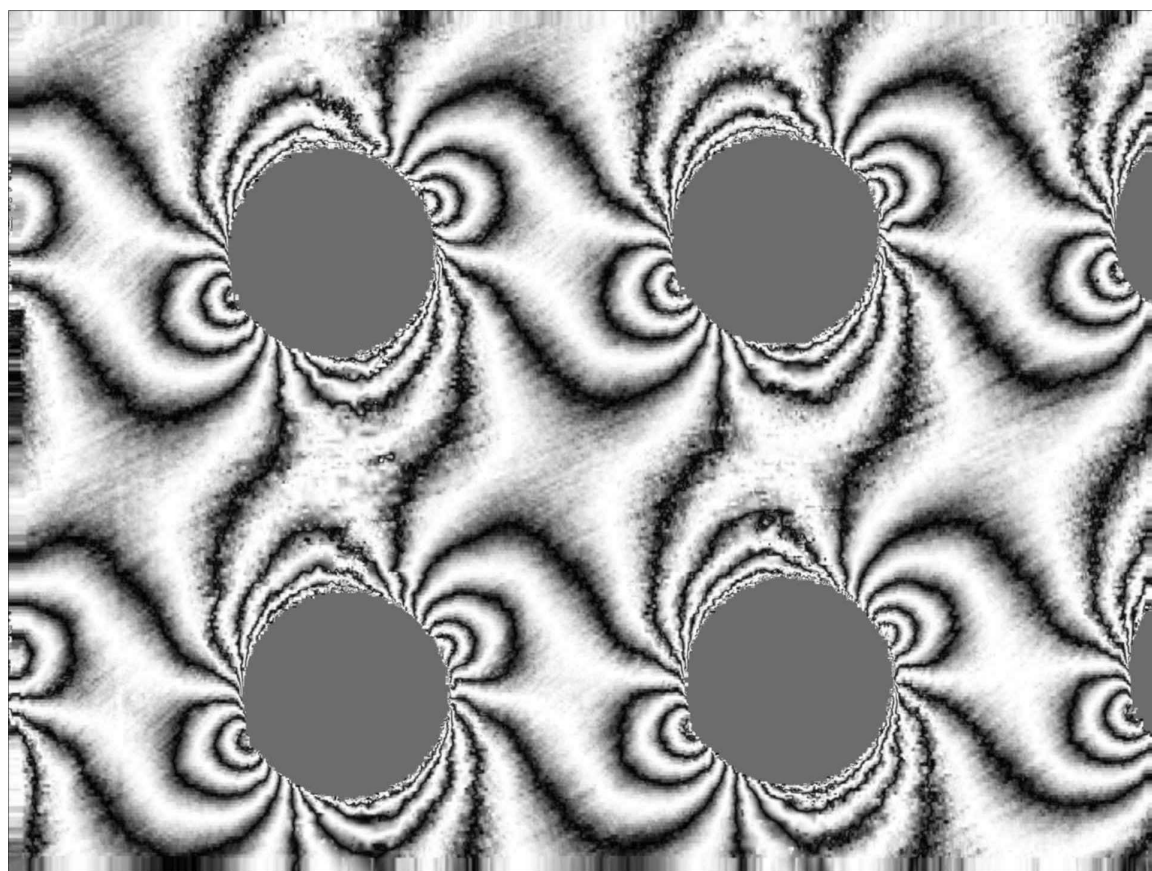


Figure 4.4: Electrokinetic speed field within an array of circular posts at 22.5° with respect to the applied electric field. The fringe spacing is 0.5 pixels per image delay ($24.5 \mu\text{m/s}$).

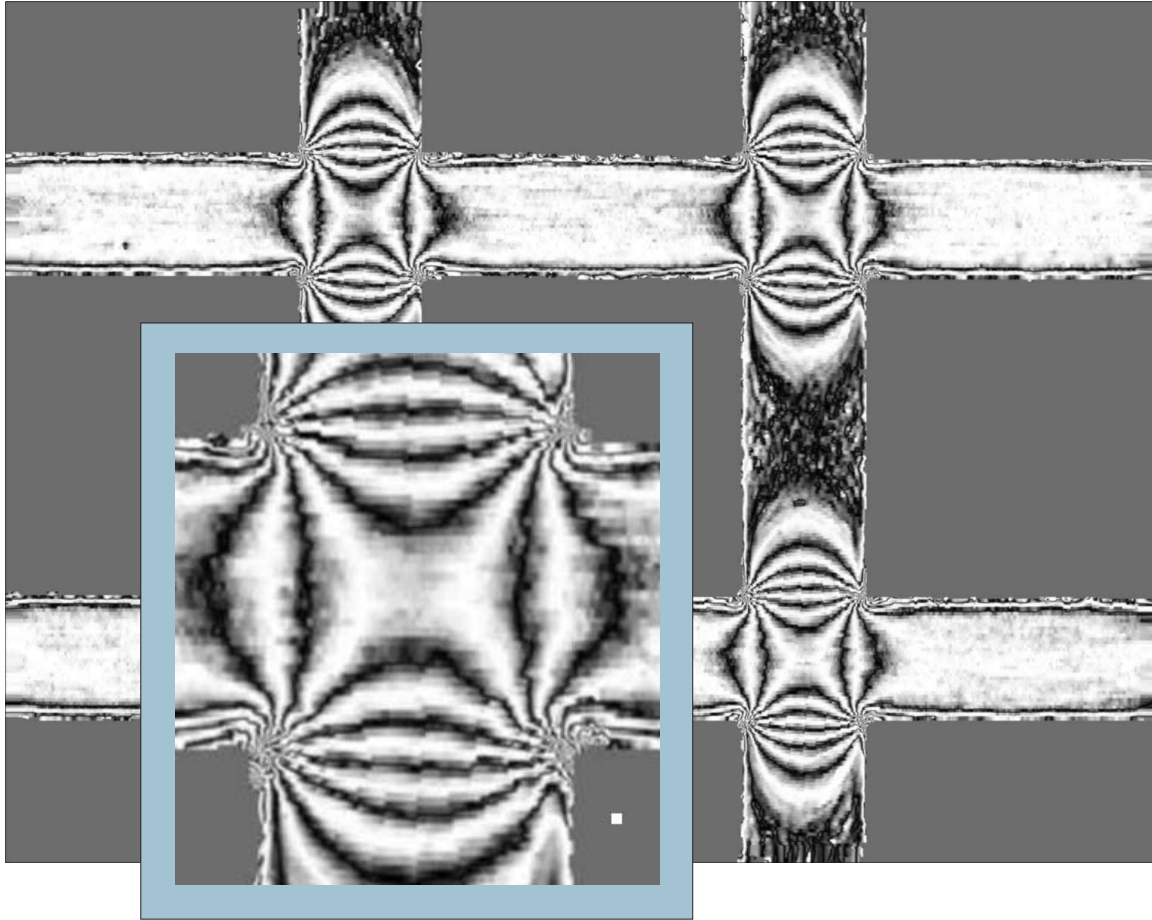


Figure 4.5: Electrokinetic u velocity field in an array of square posts at 0° with respect to the electric field applied from left to right. The fringe spacing is 0.2 pixels per image delay ($9.8 \mu\text{m/s}$). The inset image show a detail of the flow in the upper-right junction. The white rectangle in the inset shows the size of a single pixel.

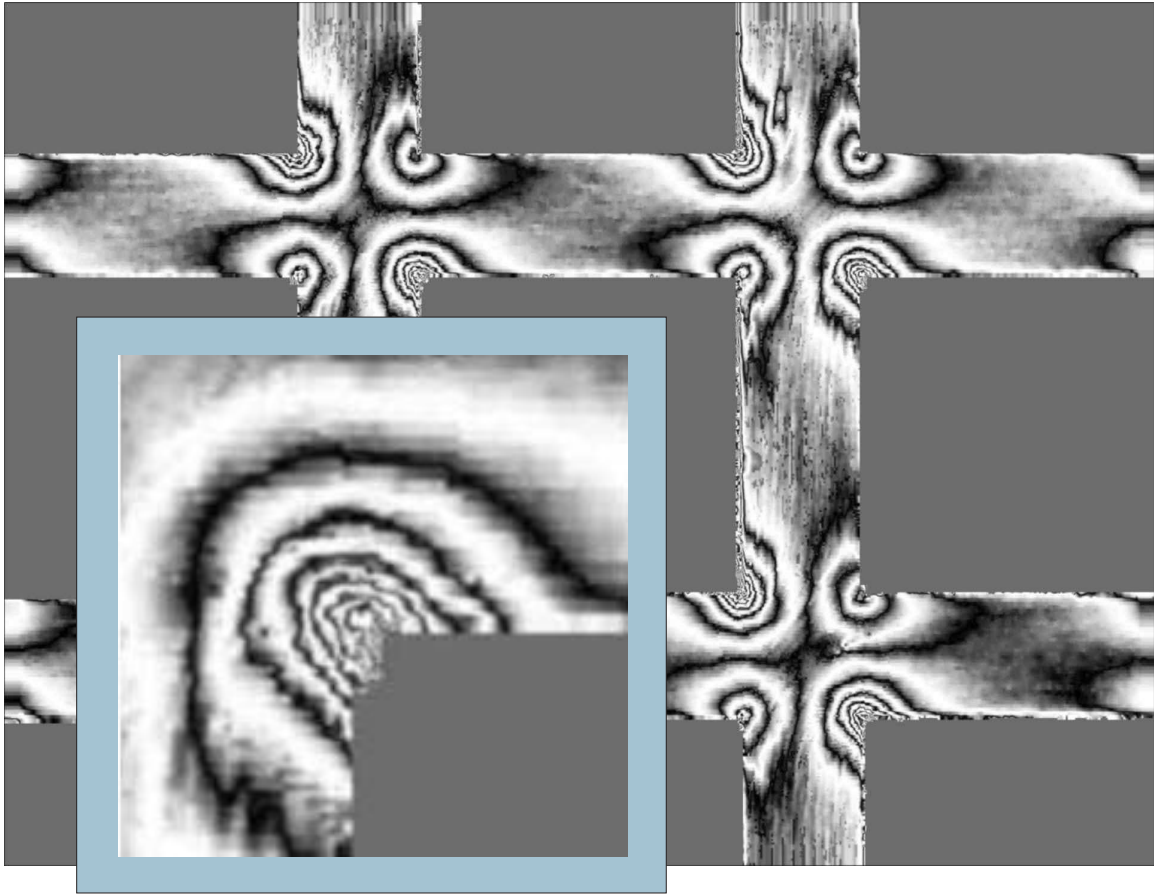


Figure 4.6: Electrokinetic speed field within an array of square posts at 45° with respect to the applied electric field. The fringe spacing is 0.5 pixels per image delay ($24.5 \mu\text{m/s}$). The inset image shows a detail of the flow in the upper right junction.

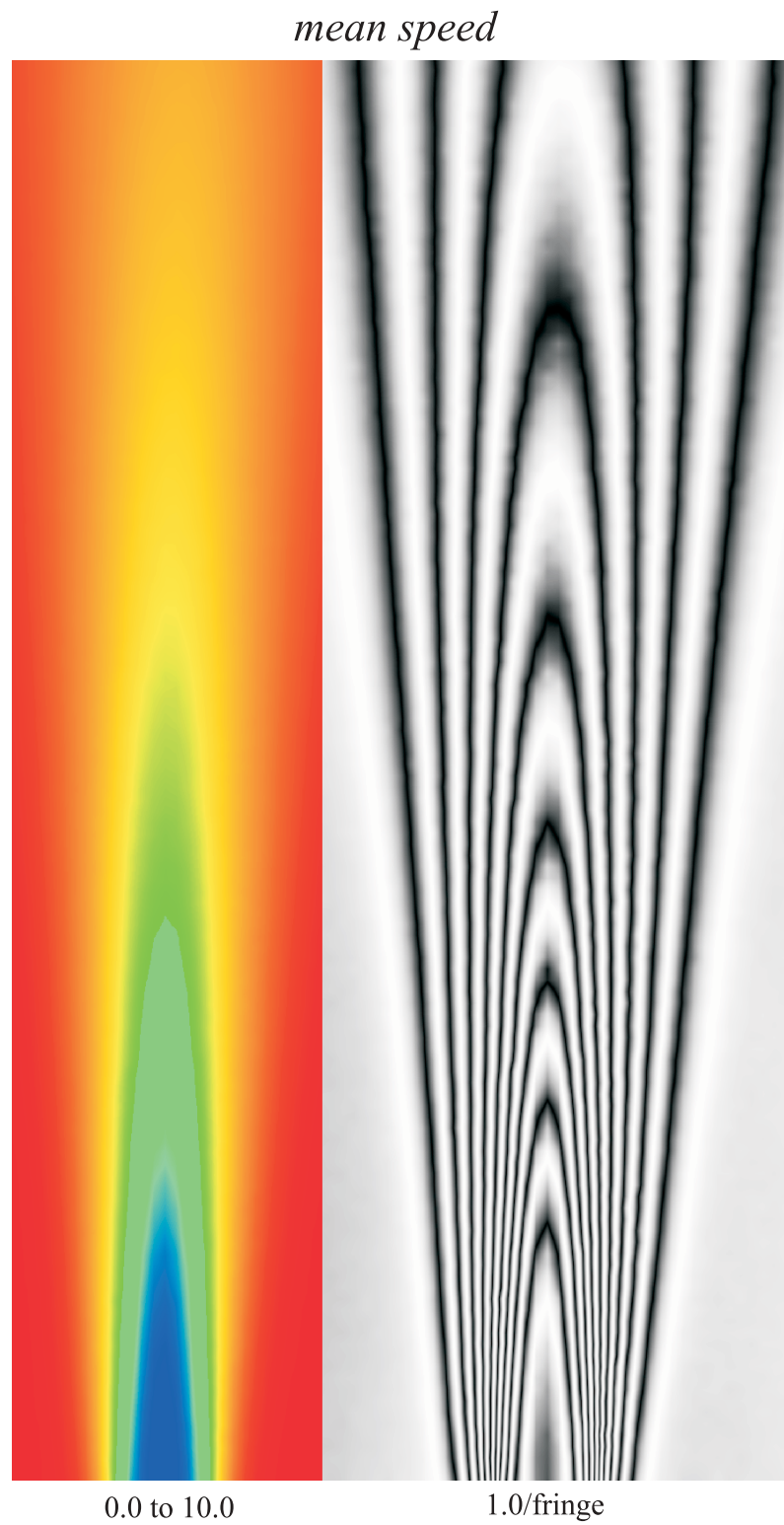


Figure 4.7: Color map and simulated interferogram of the mean speed field in the turbulent jet measured with 8×8 -pixel subimages. Red corresponds to zero speed and blue corresponds to 10 pixels displacement between images.

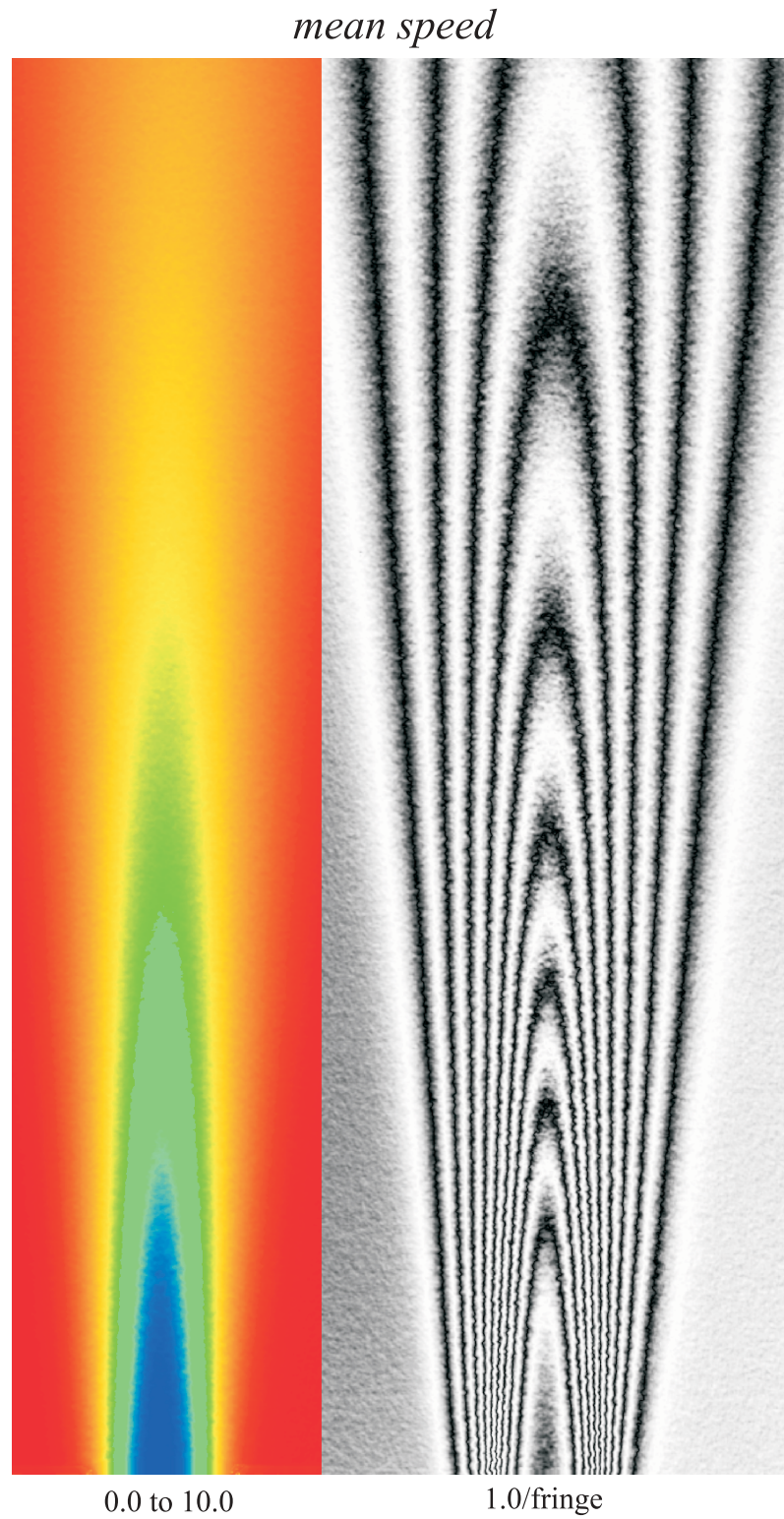


Figure 4.8: Color map and simulated interferogram of the mean speed field in the turbulent jet measured with single-pixel subimages. Red corresponds to zero speed and blue corresponds to 10 pixels displacement between images.

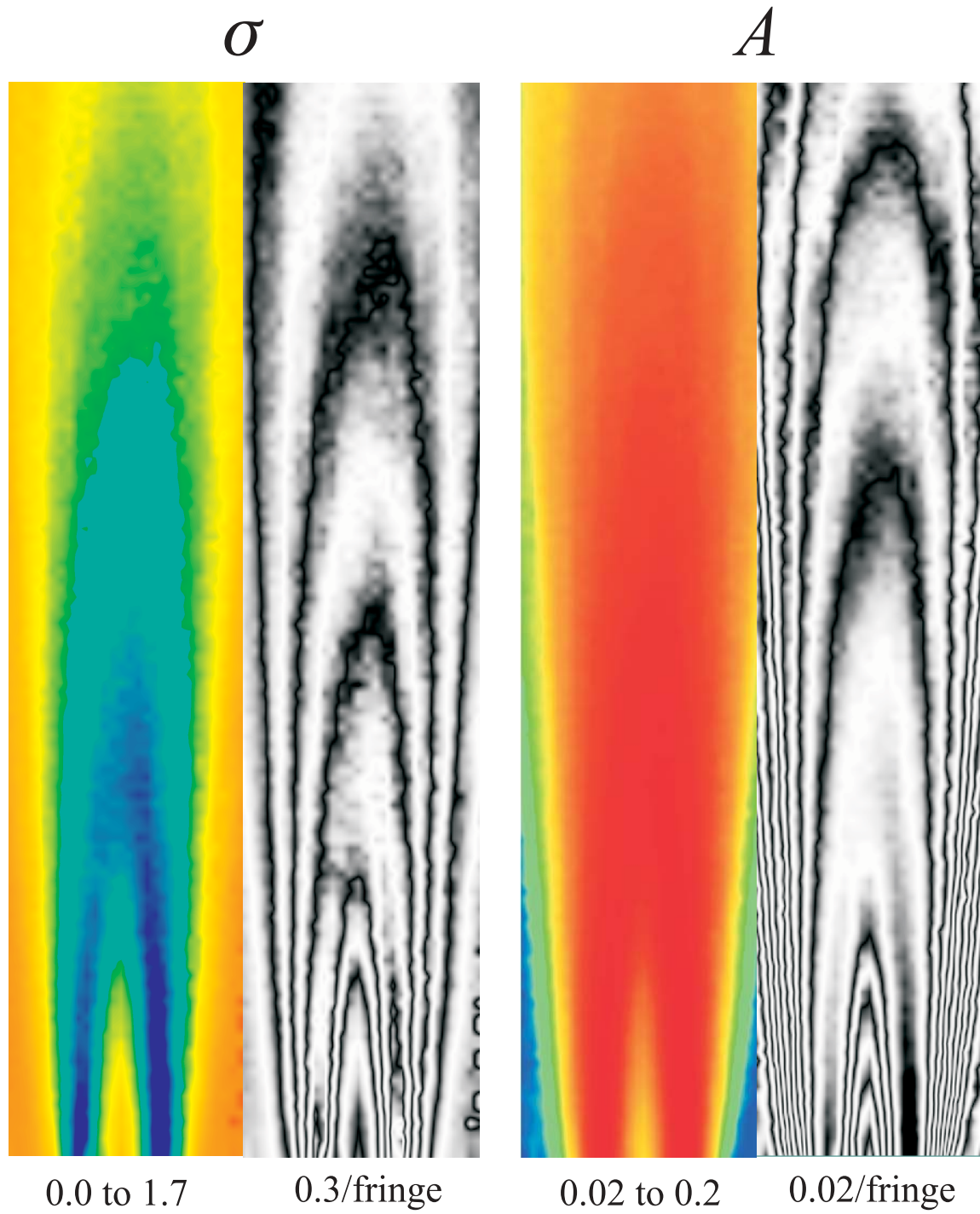


Figure 4.9: Color map and simulated interferogram of the components of the effective variance (σ) and peak correlation amplitude (A) measured with 8×8 -pixel subimages. The color-map ranges and fringe spacings are indicated beneath the images. The units of the variance are pixels per image delay and the units of the amplitude are arbitrary.

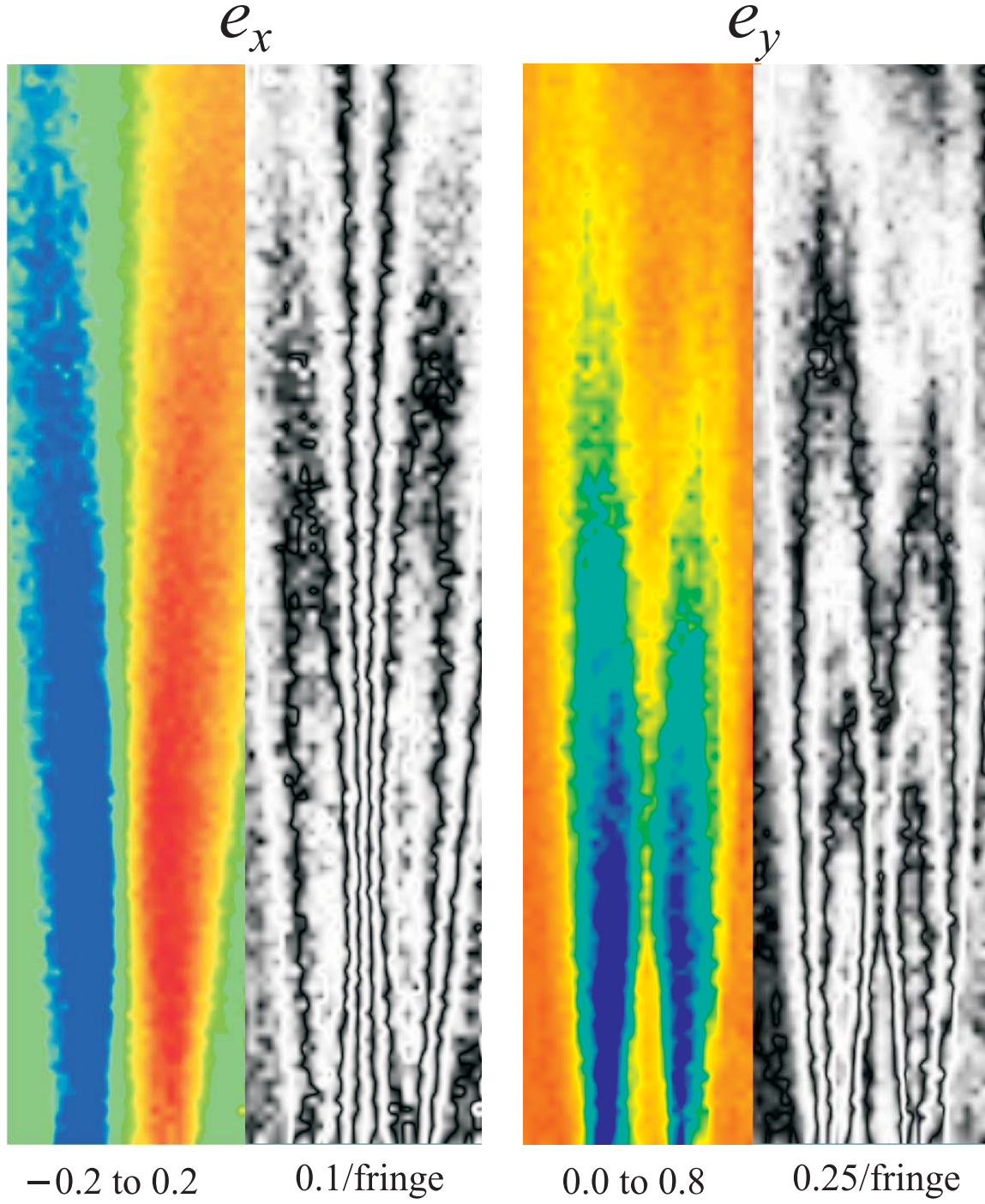


Figure 4.10: Color map and simulated interferogram of the components of the eccentricity vector measured with 8×8 -pixel subimages. The color-map ranges and fringe spacings are indicated beneath the image in units of pixel per image delay.

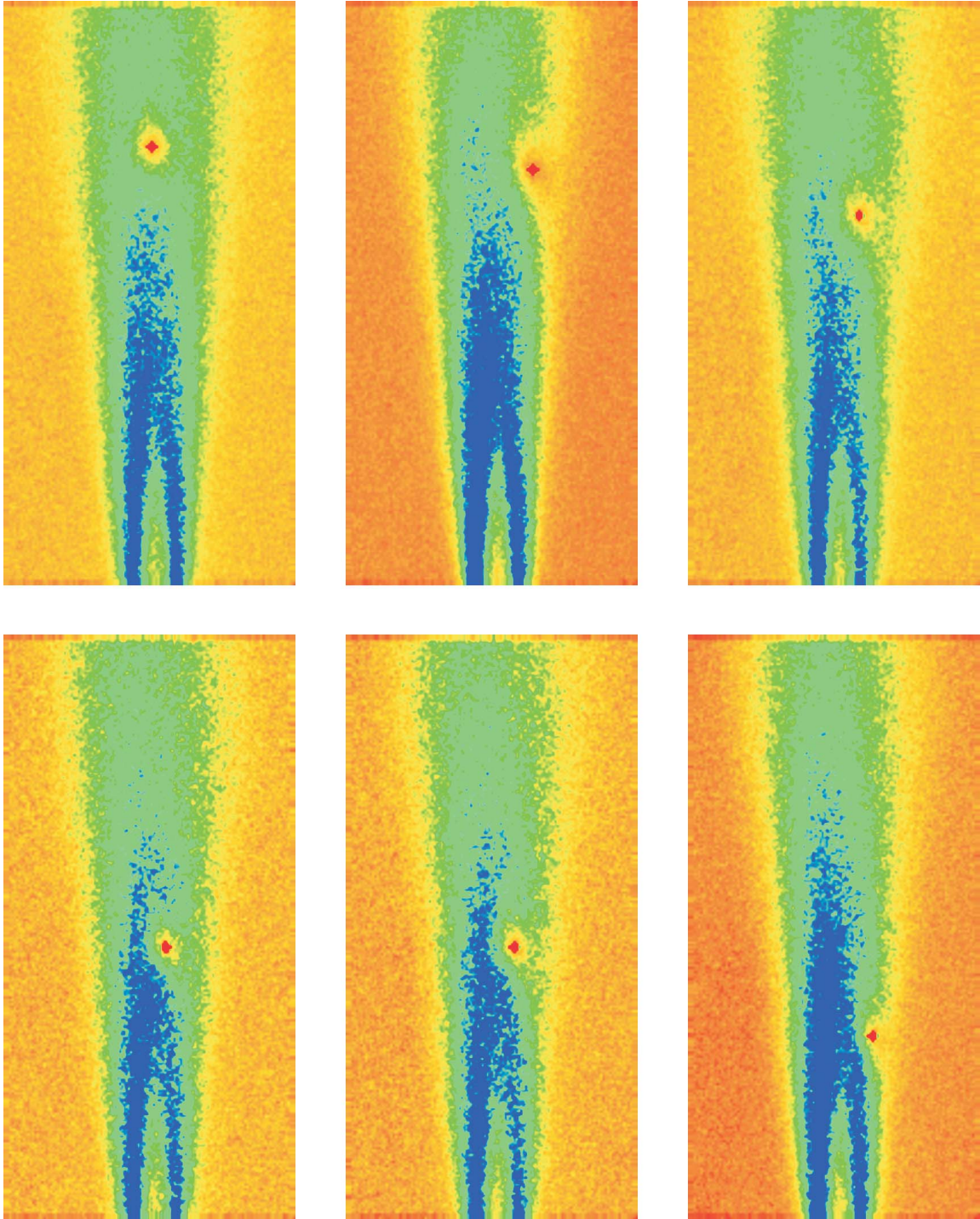


Figure 4.11: Color map of the Gaussian two-point correlation width from six different reference locations. The reference locations are located at the centers of the pronounced red spots in each image, corresponding to a small correlation width. The dip in the correlation width surrounding the reference point is evidence of the geometry of eddies near the reference region.

CHAPTER 5

Laplace: a general-purpose ideal EK flow simulator

5.1 *Abstract*

The software application **Laplace** is a general-purpose ideal EK flow simulator written to support fundamental EK theory development, experimental data interpretation, device simulation, and rapid evaluation of device concepts. The software solves the modified Laplace equation $\nabla \cdot (h(x, y) \nabla \phi(x, y)) = 0$ for the velocity/electrostatic potential ϕ on a quasiplanar domain that is specified in a bitmapped image file through the field h . The “height” of the flow domain, $h(x, y)$, is proportional to the 8-bit value of the blue channel of the image. This form of the Laplace equation properly handles both interior and boundary points. The software automatically enumerates ports where channels intersect the boundary of the image and solves for a basis set of solutions corresponding to each port individually held at unit potential while all others are held at zero potential. From this basis set a particular solution for a given set of applied potentials is constructed by superposition for simulation of particle trajectories and other post processing. To assist in studies of flow in uniform arrays, the software has a special mode which automatically constructs the array image and solves for periodic boundary conditions. Post-processing operations allow simulation of particle motion with diffusion, electrophoresis, and dielectrophoresis.

Nomenclature

- (i, j) Integral Cartesian coordinate pair
- n Index of a component of the solution vector
- h The height of the channel
- ϕ The solution of the Laplace equation, identified as a “potential”
- $\hat{\mathbf{s}}$ The unit vector along a streamline
- $\hat{\mathbf{n}}$ The unit normal vector of a boundary surface
- $\phi_{,ij}$ Second order ($i = j$) and mixed ($i \neq j$) derivatives of the potential: components of the deformation-rate tensor

5.2 Introduction

While a variety of analytical solution techniques are available for the Laplace equation that describes ideal EK flows, many of these techniques work easily only on simple geometries and do not lend themselves to general design and optimization work. Moreover post processing of the solution to obtain properties of interest like dispersion, streamlines, streaklines, and scalar transport is critical in evaluating designs but is not readily supported by even closed-form analytical solutions. The need for a general purpose ideal electrokinetic flow simulator is evident. The software application **Laplace** was written to fill this need.

Laplace is a general-purpose ideal EK flow simulator for arbitrary quasi-planar flow-channel geometries. The finite-difference computational grid is constructed directly from a bitmapped image of the desired flow geometry in which the eight-bit level of the blue component of the image at a pixel is proportional to the height of the the channel, h , at the pixel location. A value of 0x00 corresponds to a channel of zero height, i.e., a wall and a value of 0xFF (255) corresponds to a channel of the maximum height. **Laplace** solves the modified Laplace equation

$$\nabla \cdot (h(i, j) \nabla \phi(i, j)) = 0 \quad (5.1)$$

for the velocity/electrostatic potential ϕ across the image, given the channel height field $h(i, j)$ at the discrete pixel locations (i, j) of the bitmapped image. This equation is easily shown to be compatible with both the insulating boundary equations

$$\nabla \phi \cdot \hat{\mathbf{n}} \propto \nabla \phi \cdot \nabla h = 0 \quad (5.2)$$

and the interior equations

$$\nabla^2 \phi \propto h \nabla^2 \phi = 0 \quad (5.3)$$

for the Laplace equation in a purely planar geometry and is simply a statement of depth-averaged continuity in a purely two-dimensional flow. This solution is an exact discretization for ideal electrokinesis provided the depth of the channel does not vary along any streamlines, i.e., $\nabla h \cdot \hat{\mathbf{s}} = 0$ everywhere. It is a good approximation in regions where the depth varies slowly along a streamline, i.e., $\nabla h \cdot \hat{\mathbf{s}}/h \ll 1$. It is also a good approximation in regions located many channel depths away from an abrupt depth change along a streamline.

Discretizing the flow in this manner has several advantages.

1. No special handling of boundaries is inherently required.
2. Channel geometries can be specified easily using drawing programs, CAD programs, and fluorescence images of dye in actual channels
3. Channels having multiple depths can be treated approximately.
4. Natural (in the case of fluorescence images) or synthetic (in drawing software) “anti-aliasing” and defocus can be used to eliminate sharp discontinuities on boundary edges and smooth the effects of cartesian discretization on curved boundaries.
5. Simple algorithms exist for grid refinement to speed and de-stiffen solutions.

Figure 5.1 shows a 606×585 pixel image of a sample channel design sketched using a drawing program. The image has only black and white pixels, so curves are approximated discretely as abrupt steps. Figure 5.2 shows the same image with an anti-aliasing algorithm applied to use gray-scales to smooth the edges of curves. Figure 5.3 shows the same image with a blur applied to round the corners and produce smoothly varying channel depths. This particular blur simulates the effect of isotropic etching of a stamp on an embossed microchannel. Figure 5.4 shows a comparison of closeups of the

curve at the upper left in Figs. 5.1–5.3. The use of the “grayscale” approach to handling boundaries mitigates the artifacts of the discretization of the boundary on the flow/electric field solution. Figure 5.5 shows a comparison of the speed fields obtained from **Laplace** by constructing a grid from the two-tone image Fig. 5.1 and the anti-aliased image Fig. 5.2. The simulated interferograms in Fig. 5.5 show the speed field of the basis solution obtained by **Laplace** corresponding to a unit potential in the lower left port and zero potentials in the other ports. The speed difference between successive fringes is 0.2 units and the maximum flow speed is ~ 1.5 units. The mitigating effect of anti-aliasing on the artifacts of the boundary jumps is clear from the comparatively smoother speed contours in the solution at the right.

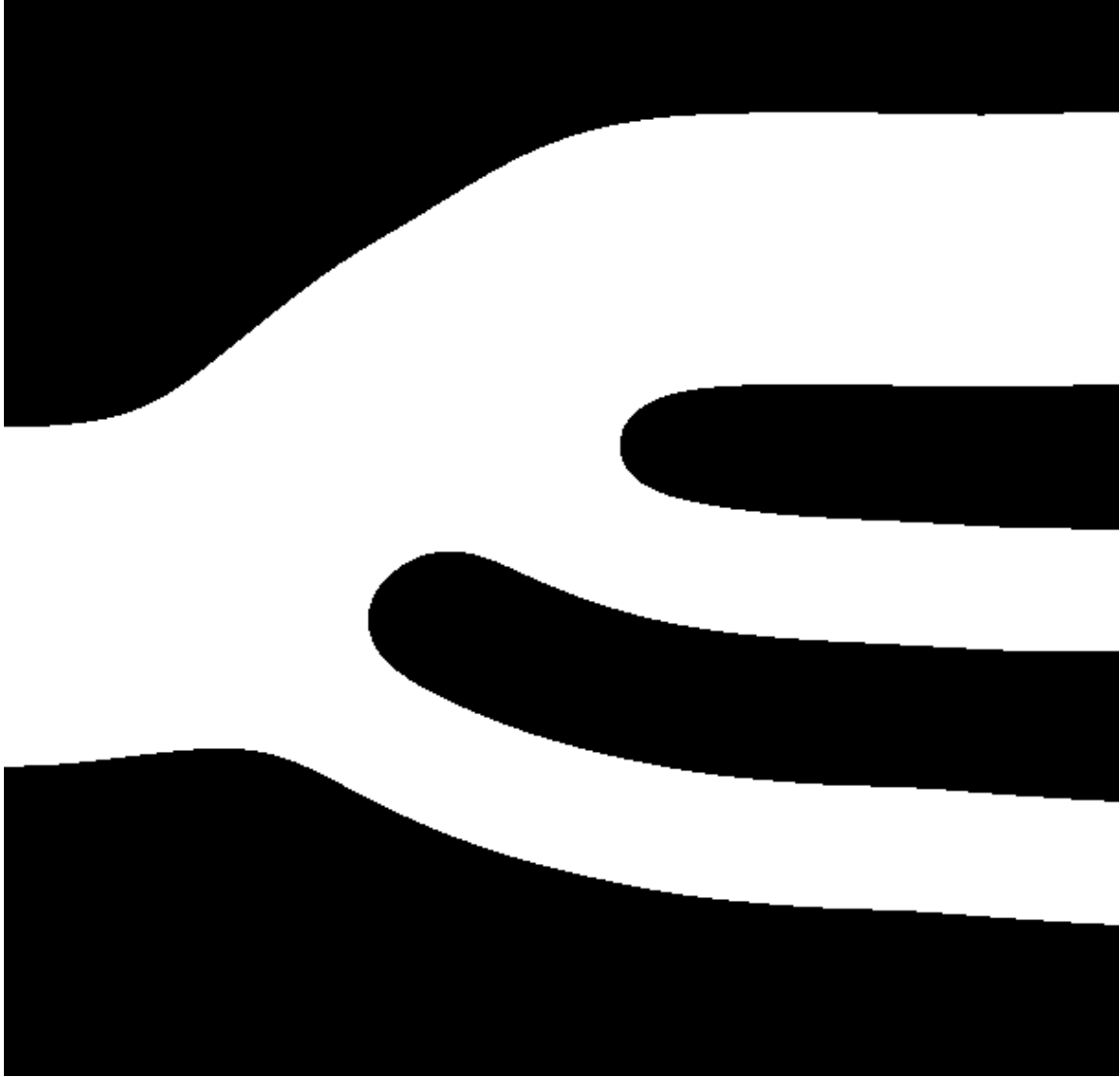


Figure 5.1: Sample black and white image of a whimsical microchannel design. Curves and lines that are not aligned with the rows and columns of the image are represented as abrupt steps.

By default, **Laplace** does not initially attempt to solve the system of equations at the full reso-

lution of the grid image. Instead, **Laplace** initially constructs a grid from a copy of the grid image that is downsampled by a power of two (typically 2^4 in each direction). Next, **Laplace** obtains a complete basis set of solutions at that reduced resolution. **Laplace** then repeats the process using successively less downsampling, interpolating initial estimates of the solutions from the previous solutions. This grid-refinement procedure improves the speed, accuracy, and robustness of **Laplace** on ill-conditioned domains. Moreover, the solver can be stopped at any point in the solution and still retain the basis set at the previous resolution. The solver can also be restarted from any step in this procedure, including restarting by opening a session that was previously saved to disk. This ability is useful since a reasonable picture of the full-resolution flow solution can often be obtained quickly at low resolution.

Figure 5.6 shows the effect of grid downsampling on the solution for the flow in the channel system specified by Figure 5.3. The solution times, t_s , are realized on a 750 MHz Pentium III computer with 512 MB RAM. The leftmost column of images shows the computational grid used by **Laplace** at the varying resolutions. The blue-green pixels correspond to zero-height channels (walls) and are not part of the solution domain. The speed-field interferogram in the second image column is remarkably consistent with grid scale factor except for the obvious pixelation and aliasing of the interferogram graphics at the lower resolutions. The streamlines plotted over a color map of the speed field in the right column fare less well at low resolutions. These lines are produced by propagating test particles through the flow system using bilinear interpolation of the flow solution. This approach to finding streamlines suffers from cumulative errors that are unacceptably large at low resolutions. Figure 5.7 shows overplots of the inverse of the transit time of particles through the flow system for solutions at different resolutions. All values are normalized to the maximum value from the full-resolution solution. The horizontal axis is the stream function, ϕ . For the full-resolution solution, particles in the small region to the left of the leftmost vertical gray bar flow from the lower-right port in Fig. 5.3 (port 0) to the narrow port 1 just above it. Particles in the region between the gray bars flow into the larger port 2 at the top right. The majority of the flow passes through port 3 at the left. The relative widths of these regions correspond to the relative flow rates through the ports. Figure 5.7 clearly shows how the particle trajectories lose accuracy at low solution resolution, affecting both scalar (time) and vector (location) integrated properties. Alternative approaches to finding streamlines surely perform better than this particle-propagation method at low resolution. However, particle simulations are favored for their simplicity and their ability to treat additional transport phenomena.

Laplace can display a variety of fields derived from the potential field solution as a color map, grayscale map, or simulated interferogram and it can save any of these fields on demand to a binary or ascii data file for external post processing. Fig. 5.8 shows these fields for an electrokinetic flow in a unit cell of a uniform array. The electric field is oriented mostly from top to bottom at an angle of $\sim 11^\circ$ to the right. The fields that can be displayed are

1. Flow speed field
2. Individual velocity components
3. Electrokinetic potential
4. Dielectrophoretic potential
5. Combined electrokinetic and dielectrophoretic potential
6. Deformation rate tensor components
7. Principal deformation magnitude
8. Vector components of the principal deformation

The location and magnitude of the branch cuts that are evident in the principal deformation vector fields can also be displayed. All these fields are available for calculation of the propagation of particles. For example the local velocity fields are useful for treating simple particle propagation with or without diffusion implemented using a Monte Carlo technique. The combined electrokinetic and dielectrophoretic potential (and its gradients) are useful for calculating particle trajectories in both filamentary and trapping dielectrophoretic systems. The deformation rate tensor and principal deformation fields are useful for semi-analytically treating diffusion and dispersion in microsystems, especially microarrays.

5.3 Software overview

Because **Laplace** is intended to fill a range of user requirements, from assisting with theoretical modeling to device design simulation and optimization, it was written to favor generality and ease of extension of its capabilities over efficiency. This tradeoff is evident in the choice of a simple first-order finite-difference solution to the Laplace equation on a uniform, square computational grid over higher-order solutions, boundary-element methods or semi-analytical methods. As discussed previously, simple particle propagation techniques are employed since they favor treating additional transport mechanisms where more sophisticated and specialized techniques could be more accurate, efficient, and limited.

Laplace uses the superb public software package PETSC[1, 3, 2], a product of Argonne National Laboratory, to solve the finite-difference matrix equations. This package provides finger-tip access to advanced solution techniques. The value of the contribution of the PETSC project to this software and this LDRD cannot be overstated.

Laplace is written in Microsoft Visual C++, extensively using the Microsoft Foundation classes for the user interface. While this limits the portability of **Laplace** to Win32 machines, this limitation is offset by programming convenience and the relative popularity of Win32-based systems. It will run on any PC, but it is preferable to have >128 MB RAM to perform moderately sized simulations without page swaps.

5.3 Format and philosophy

Laplace is intended to be a perennial work in progress, with extensions, modules, and capabilities added as needed. The ability to visualize the results of every processing step in the software was emphasized to facilitate the development of the software. For example, an image of the actual computational domain is displayed when a grid is generated as shown for the low-resolution domain in Fig. 5.9. The user/programmer can always view this domain to reconcile or debug unusual results. Moreover, the user/programmer can view a graphical representation of the equation corresponding to a selected pixel in the domain. The images in Fig. 5.10 were obtained by clicking in various locations on the image while the “View equations” option was selected. The displayed field is an auto-scaled gray scale image of the coefficient of each pixel/grid point in the equation. The image in Fig. 5.10.a shows a typical 9-point stencil for the Laplacian operator at an interior point. Because of the autoscaling, the negative value of the central pixel appears black, and the positive values of the surrounding points appear white and light gray. The zero-valued coefficients of all other points are a darker gray. This image is formed by premultiplying a unit vector corresponding to the selected equation by the transpose of the actual assembled equation matrix. Thus what you see is what is actually solved and indexing problems show up clearly and immediately. Figs. 5.10.b and c show the equations used at two points near boundaries. Because of its generality, **Laplace** must correctly form equations for all arrangements of surrounding valid (interior) and invalid (exterior) pixels. Finally, Fig. 5.10.d shows an inlet port equation, this point is an applied potential, thus no

other pixels are non-zero. Similar graphical views are available for the forcing vector of the matrix equations.

In keeping with the desire to keep the software simple, early versions of **Laplace** employed the simpler 5-point Laplacian stencil. This simpler stencil did not perform well on curved and inclined boundaries, so the better-performing 9-point stencil was adopted.

5.3 *Data display*

As shown previously, **Laplace** can display fields in a variety of formats. The display format is selected using the dialog window in Fig. 5.11. Any displayed field can be shown as a conventional color or gray-scale look-up table. If “Clip above Max” is not selected, the lookup table is repeated modulo the specified range of min to max. The combination of un-selecting “Clip above Max” and choosing a sinusoidally varying grayscale look-up table allows the user to display the data as a “simulated interferogram,” a display mode that is preferred for its ability to convey quantitative data in spite of poor printing or reproduction.

Details about any object pointed at by the cursor are always displayed in the status bar at the bottom of the main window. These include the double-precision field value, the two-dimensional coordinate, and the index in the solution vector of the selected point if the object is a field. Similarly, when a contour or particle is selected by pointing a cursor, details about that contour or particle are displayed including integrated properties such as time, distance travelled, and vector elongation and local properties such as velocity, and potential.

5.3 *Data exporting*

Displayed fields and contours can always be saved to a binary or ASCII file format at the press of a button. They can be saved in a format suited for publication by printing to a Postscript file. A variety of other formats for exported data have been developed as needed. Contour and particle properties can be saved to tab-separated ASCII data files compatible with Excel and other spreadsheet programs. Contours can also be selected and exported to a text AutoCAD script that draws the contour into a design drawing. This feature is useful, for example, to contour side walls of an off-axis microfluidic array to conform to the flow streamlines in an infinite array. This contouring ideally eliminates the effect of transverse truncation of an array on the flow in the interior of the array.

5.3 *Session serialization*

A session can be saved and restored by serialization and deserialization of its data members using the conventional “save” and “open” commands. This command saves the last completed basis solution set, and all user settings, including display, particle properties, etc. To minimize file size, contours and particles are currently not saved, although serialization code has been written for them. The default extension for saved **Laplace** sessions is “.mfl.”

5.4 *Grid formation*

The concept behind the grid generation has been detailed earlier. **Laplace** imports a computational domain from a bitmapped image, specifically a “tagged image file” or “TIFF” bitmap whose blue channel conveys the height of the channel across the image. The red and green channels are presently unused and may in the future be used to specify internal sources or sinks, specify port boundary conditions away from image edges, or for some other purpose. The blue channel is an eight-bit value for each pixel. A value of 0x00 corresponds to channel of zero height, or a wall. A value of 0xFF

(255) corresponds to the tallest possible channel height. The TIFF image is read into an array which is then optionally downsampled by the current grid scale factor by averaging pixels. For example, if the grid scale factor is sixteen, sixteen-by-sixteen-pixel regions of the image are averaged to produce a new image array for specifying the grid.

Only non-zero-valued pixels in the image array are used in the computational grid. On the first pass through the image, all non-zero pixels are counted. This count is the number of equations to be solved. A vector of solutions and forcing functions of this size is allocated and a square matrix of this size squared is allocated. These allocations are performed by calling functions in the PETSC toolbox. PETSC uses sparse matrix techniques, so opening an image of 200,000 pixels does not immediately allocate a $40 \cdot 10^9$ -element matrix! A forward and reverse map from coordinate (i, j) to equation index n is made.

The image is scanned for ports where channels intersect the border of an image. These ports are enumerated. The number of basis solutions required to construct a basis set is one less than the number of ports, since the last basis solution can be constructed by superimposing the trivial constant-potential solution and a scaled superposition of the other solutions. Scanning of ports proceeds along the image boundary in a counter-clockwise sense from the bottom-left corner.

Next the image is scanned for “islands” of zero-pixel values surrounded by channels. These islands or posts are enumerated. This was originally done so the circulation around each island could be specified¹. Later it was realized that the applied-potential boundary conditions implicitly force the flow to have no circulation about internal boundaries, as required for an ideal EK flow in the absence of a time-varying magnetic field. The enumeration of islands and the somewhat involved coding to generate equations to specify the circulation about arbitrary bodies has been retained as an option in the code in case studies of EK flows with magnetically induced circulation become of interest. The enumeration of islands has no other purpose. Passing the cursor over an island causes the integer identifier of the island to be displayed.

At this stage the equations matrix is ready to be assembled. First the equations for all interior points are added, including points adjacent to internal boundaries. Next the equations for the circulation about islands may be optionally added. Finally, the equations for the port boundary conditions are added both to the equation matrix and the forcing vector. Only these port equations vary between each basis equation set. The routine to add the port equations is therefore passed an argument identifying what set of port boundary conditions to apply.

Next, if there is a previous solution to the flow in memory, most commonly a solution at lower resolution or perhaps a solution having a different set of solver options, the software copies the previous solution into the initial guesses of the solution, interpolating as needed.

Now, the grid image, equations, and boundary conditions have been formulated and may be viewed graphically as described above.

5.4 The user interface

The user interface for this operation is quite simple. Pressing the toolbar button “import grid from image” opens a standard file dialog that by default shows files having the “.tiff” and “.tif” extensions. Selecting an image and clicking “Open” automatically grids and displays the system at the initial grid-scale factor.

If the user wishes to change the initial grid scale factor from its default of 16, before opening the bitmap, the user should click “View>Solver controller...” and set the desired scale factor in the dialog that opens. This dialog is described in more detail later.

A special tool was created to facilitate studies of flow in arrays. This tool automatically generates an image of a unit cell of a square array to user specifications for square and circular posts. This tool is accessed by clicking the “Create rectangular array” button on the toolbar. The user can then select the array properties from the popup dialog shown in Fig. 5.12. Processing of the automatically

¹Circulation is the line integral of the velocity along a closed curve.

generated image is the same as described above, except a flag is automatically set that a periodic solution is sought and the port equations are adjusted accordingly.

5.4 Notes from beneath the hood

The TIFF image is imported into a custom class called a CCArray that supports the resampling operations. The CCArray is part of a standard family of array classes that have been written to facilitate image and array manipulation, interpolation, differentiation, etc.

The mapping between pixels and equations is not one-one because there are fewer equations than pixels. Elements of the forward map are flagged by a negative index at points that do not have associated equations. These maps, the number of equations, the size of the images, the grid scale, and other parameters needed to interpret the channel geometry are modularized in a class called the “CGeometryMap.” In the island-detection step, each island is given a unique negative identifier. Elements of the forward map at positions on an island are given the (negative) value of the island.

A family of array classes used in **Laplace** is derived from the super class CMappedArray, which internally contains an array of values that are mapped to and from a two-dimensional rectangular field by a CGeometryMap, e.g., solutions to the flow equations that occupy a vector, but that correspond to the potential at various (i, j) points. The CMappedArray and derived classes were written to handle (and thus shield the developer from) complex indexing using the CGeometryMap for things like taking spatial derivatives, interpolating between solution points, etc.

5.5 The flow solver

Following the gridding of the image, the system of equations is ready for solution using the PETSC toolbox. The solution proceeds by executing the following steps.

1. Initialize the grid scale; clear the solution; open the image or automatically generate the image at full resolutions.
2. Down-sample the image by the current grid scale; load the interior equations; clear the basis solution counter.
3. Load the port equations (boundary conditions) for the current basis solution and interpolate the initial solution estimates from the previous solution, if any.
4. Solve the current system to the specified convergence. Update the displayed field periodically during the course of the solution. If the user has cancelled the operation, quit this procedure. The highest-resolution *complete* basis solution set will be retained, if any.
5. If there are more basis solutions to solve, increment the current basis solution counter and go back to step 3.; otherwise proceed.
6. Keep a copy of the current complete solution set and discard the previous solution set, if any. If not at the final grid scale factor, divide the grid scale factor by two and go back to step 2.; otherwise the solution is complete.

The principal advantage to nesting the grid refinement and basis solution switching in this fashion is that the user may stop the solver at any point in the solution and retain a complete basis set of valid solutions.

5.5 The user interface

The solver controller dialog, shown in Fig. 5.13, allows the user to change the properties of the flow solver and to start solving for the flow basis set. This dialog pops up automatically after a TIFF image is loaded and can be opened also by clicking “View>Solver controller...” menu item. This dialog allows the advanced user to attempt solution using a variety of different Krylov subspaces and preconditioners, change the initial and final grid-scale factors, and change convergence criteria. The default values have been found to work well for even very ill-conditioned domains and there is likely little need to change anything other than the final grid-scale factor or convergence criterion. Clicking “Solve” initiates the solution. The “Solve” button remains depressed while the solver is running. The displayed solution updates periodically, and a solver timer in the status bar shows the duration of the solution. Clicking the “Solve” button during a solution stops the solution when the current internal iteration of the solver completes. These iterations can be time consuming when large numbers of equations e.g., >200,000, are being solved, so there may be a lengthy delay before the solver actually aborts its task. Pressing the “Solve” button again resumes the solution. The properties of the solver may be changed during the course of a solutions. For example, the convergence criterion or even the Krylov subspace iterator can be changed mid solution. If the solver is running, the changes are actually implemented after the current internal iteration is complete. See [3] or [1] for more information about the numerical schemes and solver options.

5.5 Notes from beneath the hood

The PETSC toolbox is written in the C programming language. To accommodate object-oriented coding in C++, the CSolver class was written, a wrapper class for all the solver operations. The solutions are contained in a class called the CSolution and the basis set of solutions is a doubly linked list of CSolutions called the CSolutionList. The actual work of solving the equations, including the nested loops described in the previous list is performed in worker threads spawned by the CSolver. Multi-threading allows the user-interface to be responsive even when the solver is hard at work. The threads terminate when the solver is finished or when the solution has been cancelled by the user.

5.5 Port boundary conditions

Laplace supports a variety of port boundary conditions, but actually uses only a few in the automatic solutions: applied potential and applied no flux. The boundary conditions, fluxes, and properties of the ports can be viewed using the dialog shown in Fig. 5.14. This dialog is accessed by clicking the “View>Port properties...” menu item. This dialog currently is currently “read only,” and does not allow the user to modify the boundary conditions. In future developments, this dialog may be used to allow the user to specify more general boundary conditions. In addition, the user will in the future be given the options of reviewing the automatically generated basis set, changing the boundary conditions, and even eliminating some of the solutions, for example, if only a single particular solution is of interest.

5.6 Flow post-processing

Only half the usefulness of Laplace is its ability to solve for flow fields. In the majority of cases post-processing of the solution is essential. Often, the goal of simulations is to quantify dispersion and scalar transport. Also often, sequences of applied fields are required to achieve a desired device operation, for example injecting a band of analyte into a separation column or mixing two fluid streams. The post-processor of Laplace has been written to address these needs. Users can specify sequences of “steps” in a process. Entities called “particles,” “contours,” “flows,” and “super-particles” are available to simulate transport through these sequences of steps.

5.6 Steps

A “step” in a sequence corresponds to the application of a specified superposition of basis flows for a specified amount of time. Steps and sequences can be programmed using the Sequenced-field properties dialog shown in Fig. 5.15. An arbitrary number of steps may be specified for a sequence. The user manually edits the coefficients of the solutions contained in basis set of solutions. For user reference, the port boundary conditions of each solution are summarized in the second column of the list.

At the start of a step, the particular solution required by the step is calculated by superposition. Then all the derived fields needed for propagating particles are calculated. These usually only include the electrokinetic velocity field, but can more generally include the combined electrokinetic and dielectrophoretic velocity field and the deformation tensor fields. These fields are calculated once per step, then are available as look-up tables for further post-processing.

5.6 Particles

The particle is the most primitive element that undergoes scalar transport. The other elements (contours, etc.) are groups of particles. Each particle has a vector location, velocity, and elongation and scalar elapsed time, propagated distance, starting potential, and current potential, among other integrated and local properties. Particles also have display properties, e.g., color, and physical properties including electrokinetic mobility, dielectrophoretic mobility, and diffusivity.

When a particle propagates, it updates all its properties according to the bilinearly interpolated values of the fields at its location. Particles can be instructed to propagate for a small time step (treated as an infinitesimal step), for a finite time step, or for a finite total distance. The small-time-step propagation assumes the local values of the fields, e.g., velocity, are constant over the short distance propagated. First, integrated values, e.g., the location, are updated using the previously interpolated local field values. Then the local field values are interpolated at the new particle location. The finite distance and time propagation proceeds as a series of these short-time propagation steps.

If the particle has a finite diffusivity, at each small-time-step a suitably scaled random velocity perturbation is added to the interpolated local velocity.

5.6 Contours

Three types of contours are currently supported: streamlines, streaklines, and pathlines, each having their usual meaning. Figs. 5.16.a and b respectively show streamlines and streaklines of an EK flow in an array of posts. Because these contours are calculated by propagating particles, they can be augmented by additional transport mechanisms. For example, Fig. 5.17.a shows streaks of simulated particles undergoing both electrophoresis and diffusion. Figure 5.17.b show streaks of simulated particles undergoing electrophoresis, dielectrophoresis, and diffusion. The dielectrophoretic mobility of particles in Fig. 5.17.b is high enough that trapping is evident. The background image is a spectral color map of the mean speed of particles. The differences between the background images and particle streaks in Figs. 5.17.a and b highlights how dielectrophoresis modifies both the Eulerian and Lagrangian particle motion.

5.6 Super particles

Super particles are special-purpose objects that propagate through the flow providing advanced diagnostic information, normally to assist with theoretical work. For example, one super particle is a collection of a large number of diffusing particles that are initially at the same location. As the super particle propagates, it provides information about the location distribution of the diffusing particles. Another super particle consists of a small ring of particles surrounding a central particle.

This particle quantifies the finite elongation and deformation experienced by a particle traversing the system. Both these super particles are useful in the process of validating theoretical models of dispersion and diffusion.

Super particles can be launched at any point in a flow by simply double-clicking on the flow image where the particle is desired.

5.6 Flows

In **Laplace** a flow is a dense collection of non-interacting particles. Flows are a computationally inefficient way to simulate transport of a scalar in a microsystem. They are included in the **Laplace** application for completeness, but their use is not recommended.

5.7 Conclusions

Laplace is an application that supports both rapid evaluation of designs and detailed simulation of transport processes in microsystems. The novel use of a bitmap image to specify the channel geometry puts quantitative analysis of ideal EK and DEP microfluidic systems in reach of anyone with a drawing program. Solution of a basis set of applied-potential solutions for a four-port system of $\sim 200,000$ equations (channel pixels) takes only four minutes on a mid-range personal computer, while systems of $\sim 10,000$ equations take under 4 seconds. The time elapsed from sketch of a design concept to complete solution and simulation of scalar transport in the design is measured in single-digit minutes. A designer can perform a dozen design optimization iterations in an hour.

Laplace has been designed to support coding development, with advanced debugging features like the ability to view graphically any interior or boundary equation. Complicated indexing and array manipulations have been placed in thoroughly tested classes of objects that are available to the developer.

Laplace has also been designed to provide the user a circumspect view of simulation results. A variety of fields derived from the solutions may be displayed in a many different visual formats or saved to disk for external post processing. Post-processing of solutions allows the user to generate, view, and save to disk quantitative streamlines, streaklines, and pathlines. By specifying a finite particle diffusivity or dielectrophoretic mobility, the user can simulate complex transport phenomena like trapping and filamentary dielectrophoresis.

5.8 Future development areas

As stated earlier, **Laplace** is a work in progress. It is expanding to meet the needs of both designers and theoreticians. Several priority areas of expansion have been identified:

1. quantification of dispersion by both direct simulation and semi-analytical theory,
2. automated design optimization,
3. quantification of filamentary dielectrophoresis by both direct simulation and semi-analytical theory, and
4. implementation of (and user access to) a broader range of boundary conditions.

Many other developments are possible, e.g., simultaneously handling particles having different physical properties, treating non-ideal effects perturbatively, etc. Any such developments will be driven by customer need.

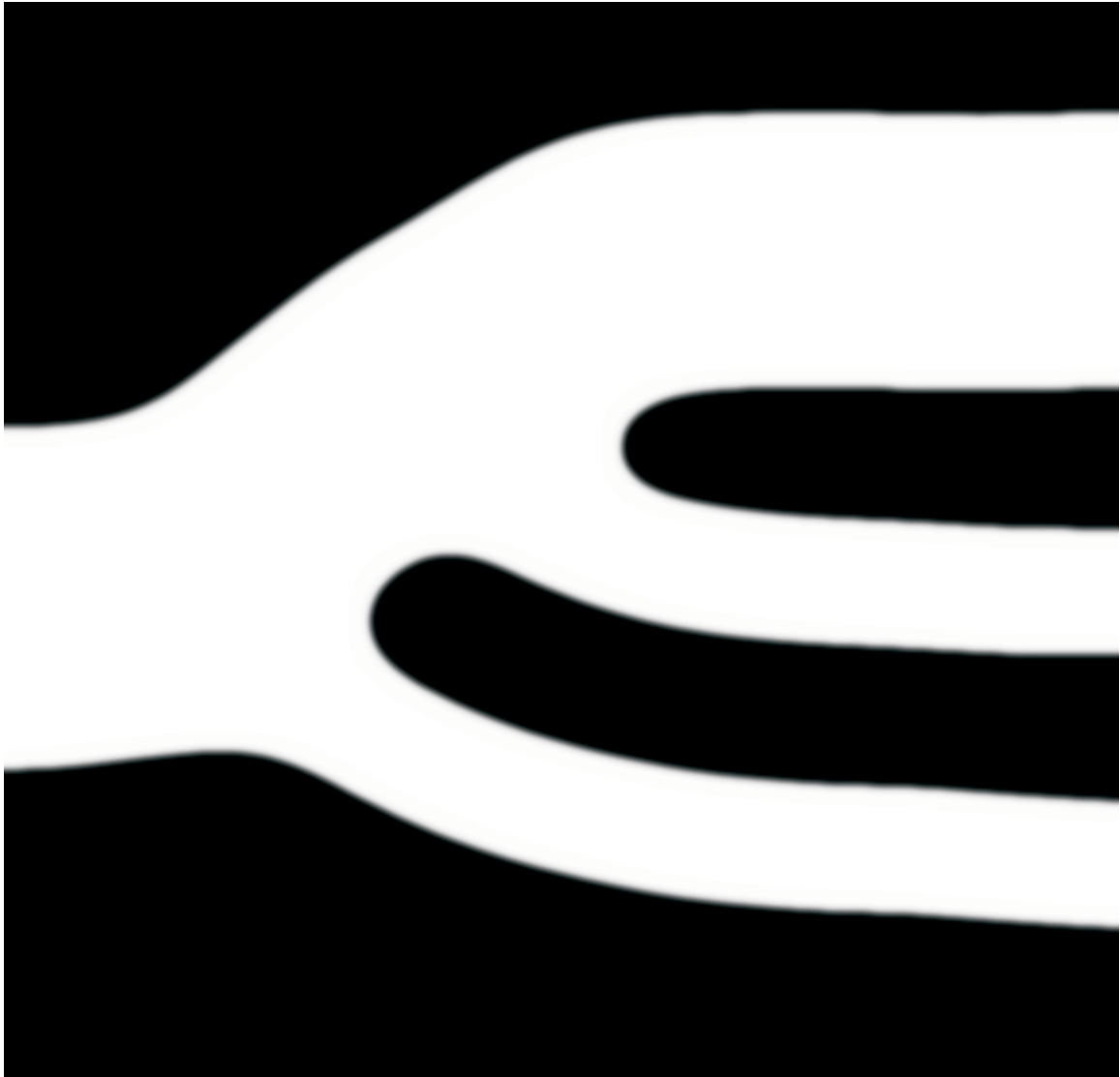


Figure 5.2: Sample anti-aliased gray-scale image of the same whimsical design as in Fig. 5.1. Boundary curves and lines are smoothed by representing them using grayscales. This smoothing dramatically improves numerical results produced by `Laplace` .



Figure 5.3: Sample anti-aliased and blurred gray-scale image of the same whimsical design. The blurring simulates the slope of walls that are fabricated using non-ideal techniques, e.g., embossing by an imperfect stamp. This allows the user to simulate systems that approximate production geometries.

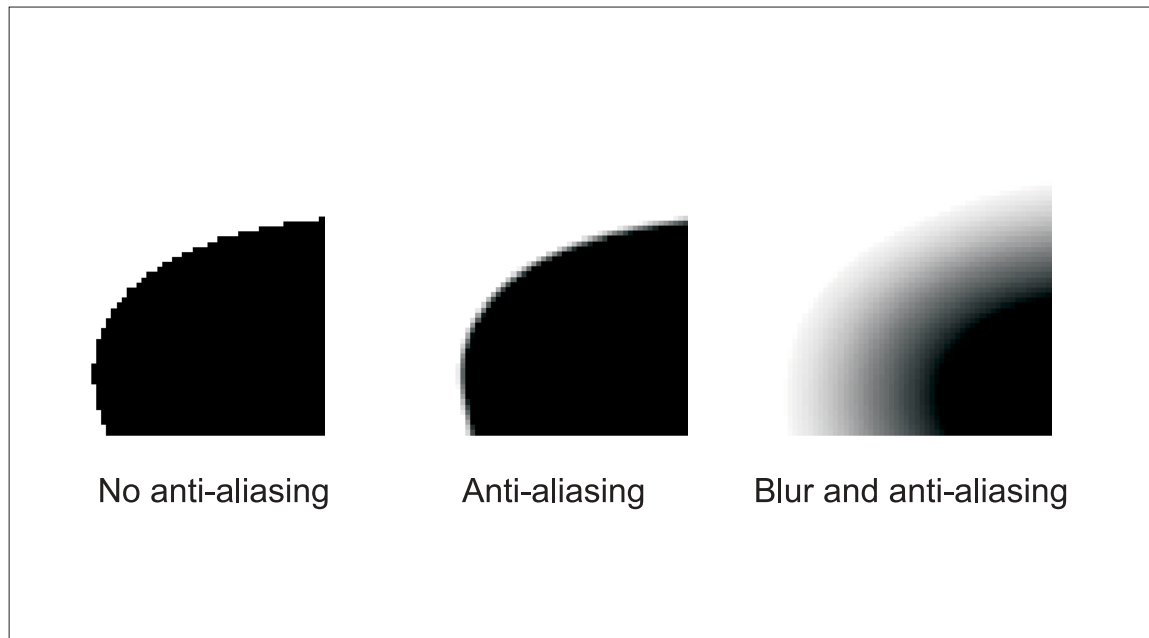


Figure 5.4: Close up of a corner from the previous three grids showing the effect of anti-aliasing and blurring.

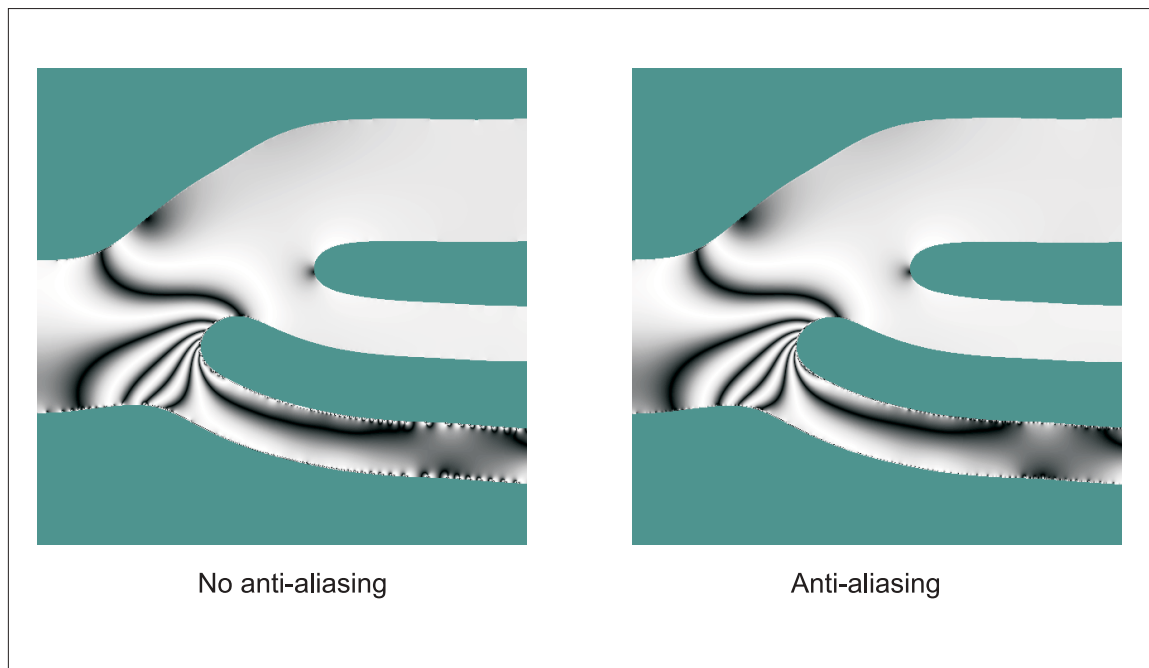


Figure 5.5: Particular speed field solutions obtained by `Laplace` using the black-and-white grid in Fig. 5.1 at left and the gray-scale grid in Fig. 5.2 at right. The speed fields are presented as simulated interferograms. The solution at left shows considerable artifacts of the discrete boundary steps, while that at right is less affected.

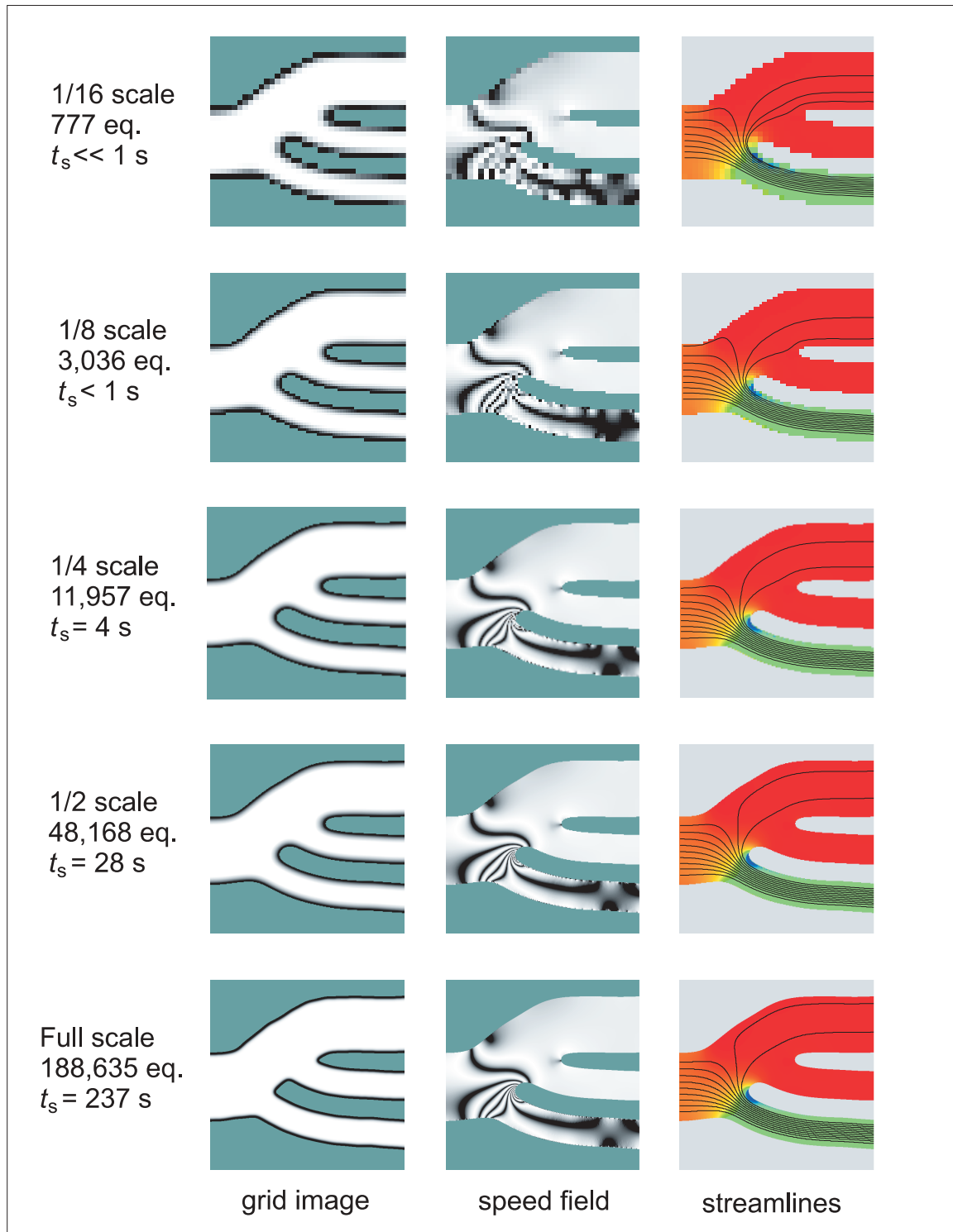


Figure 5.6: Grids and solutions derived from Fig. 5.3 at varying amounts of downsampling. The image in the left column is the downsampled grid image (blue-green pixels are outside the solution domain). The center column of images shows a simulated interferogram of the speed field. The right column shows calculated streamlines overlaid on a color map of the speed field. The streamlines are affected more than the speed field by reductions in resolution.

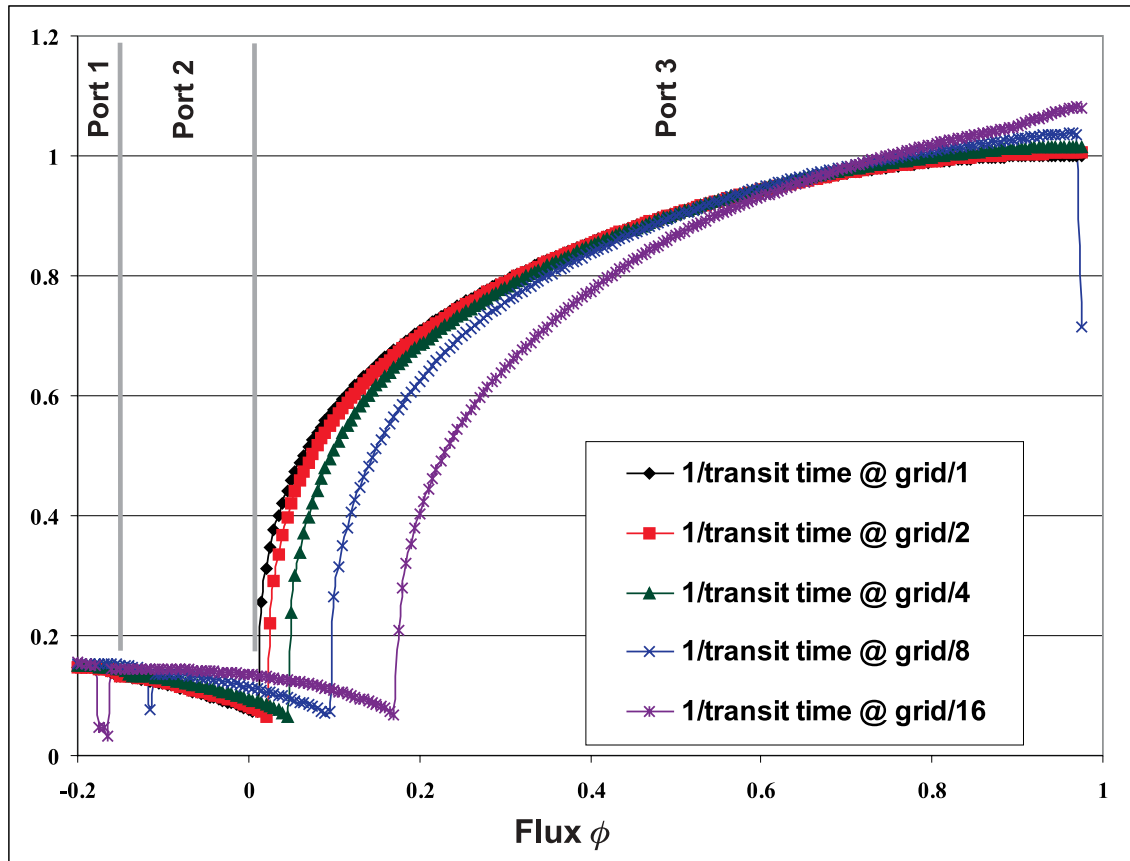
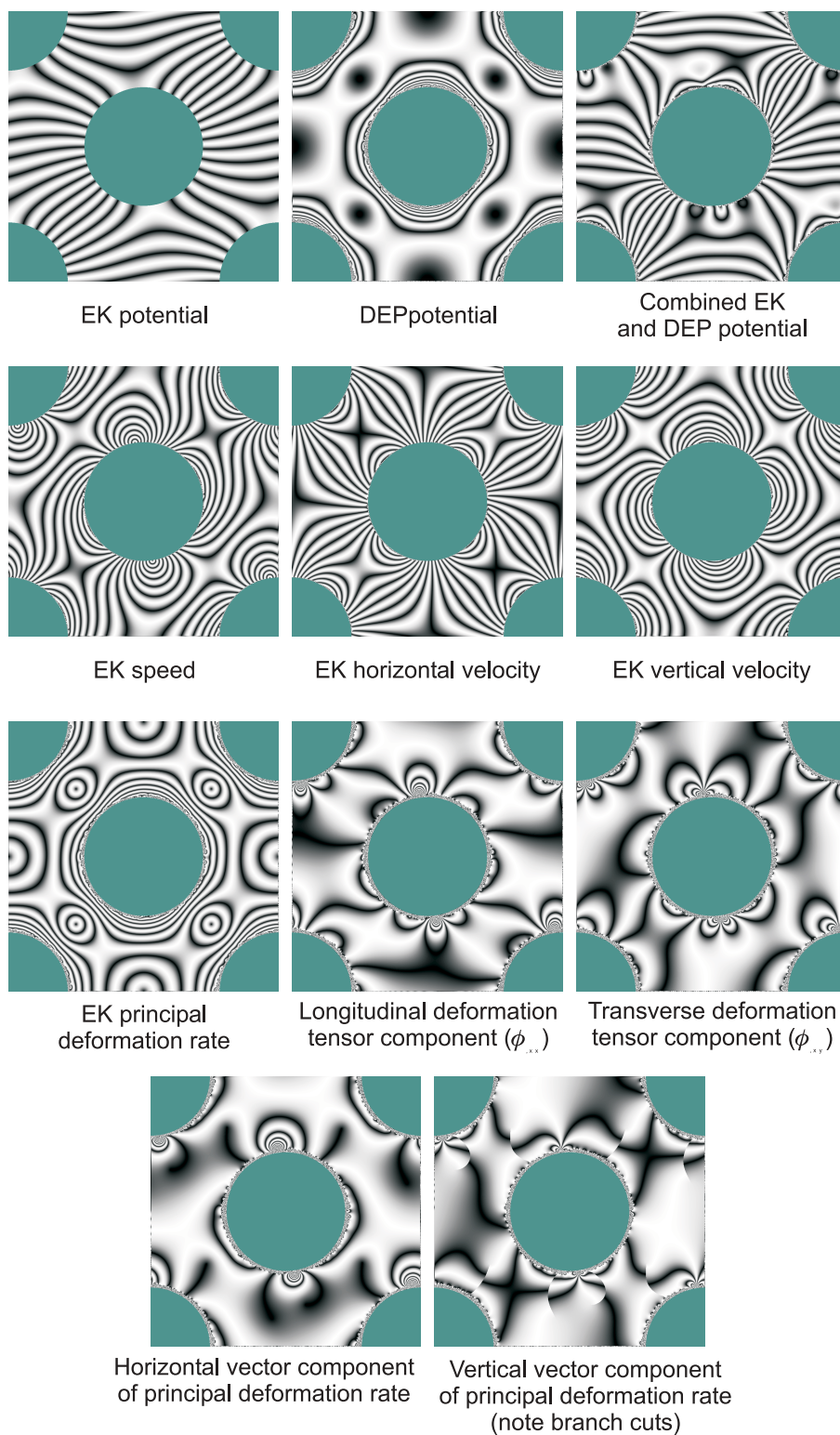


Figure 5.7: Calculated curves of the inverse of the particle transit time through the whimsical microsystem versus stream function. The gross deviations of these curves at low resolution is caused by cumulative errors from interpolation in the particle-propagation.

Figure 5.8: Fields that `Laplace` can display and save to disk.

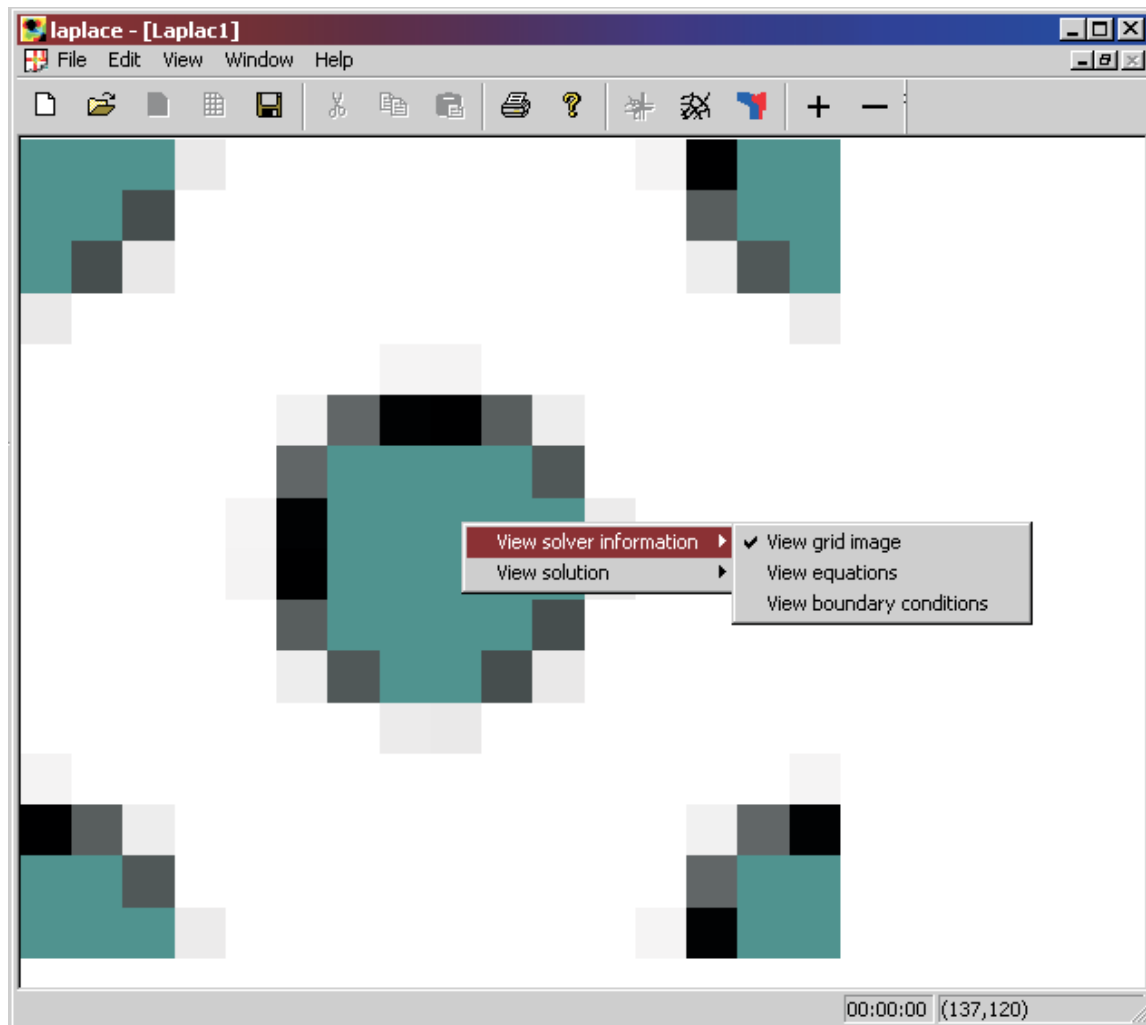


Figure 5.9: Screen shot of Laplace displaying the computational grid of an array at low resolution.

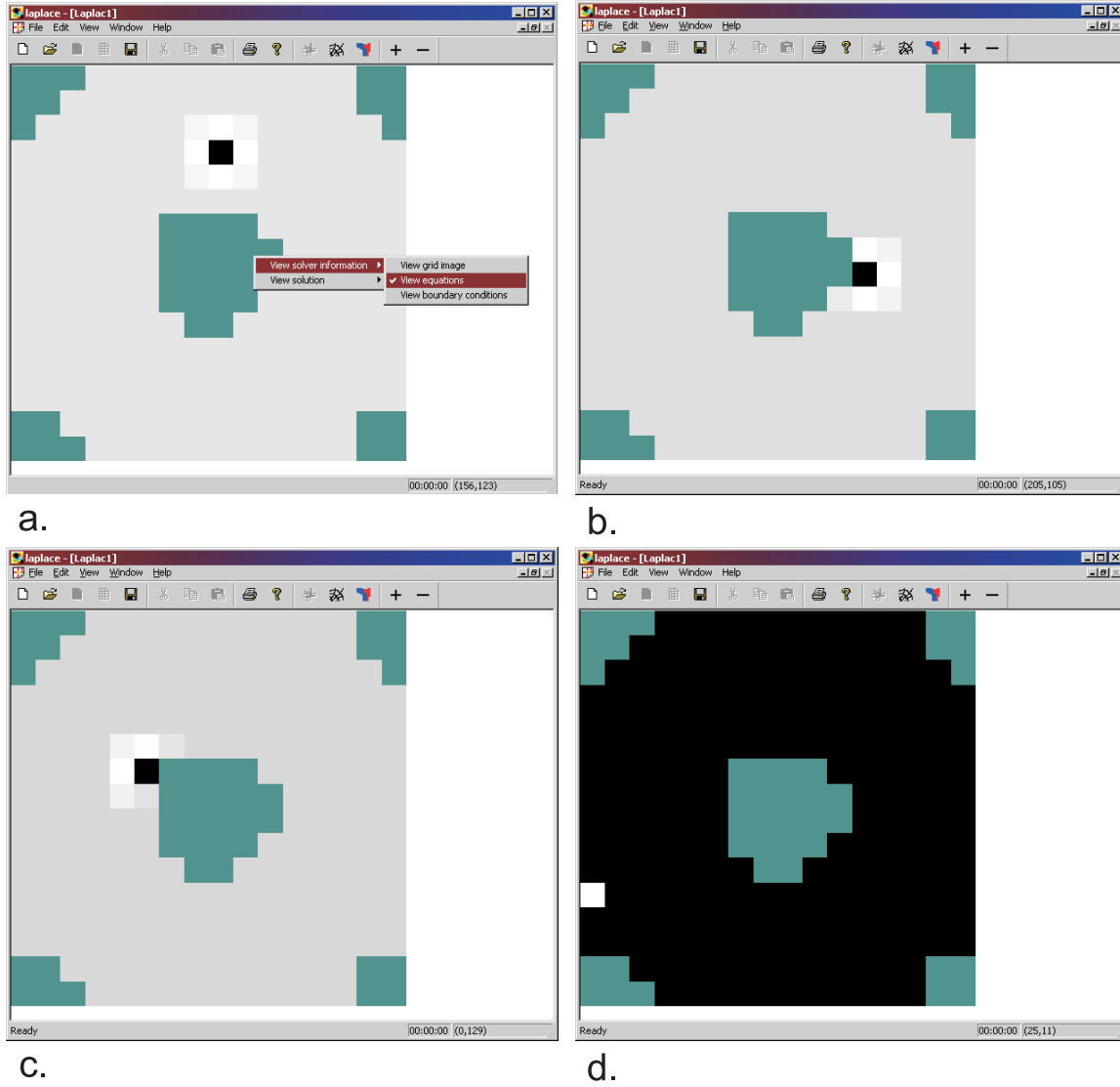


Figure 5.10: Screen shots of Laplace graphically displaying the equations automatically generated an interior point (a.) near an internal boundary (b. and c.) and at a port (d.) Interior equations are gridded using a 9-point Laplacian stencil. Equations next to boundaries require a customized stencil.

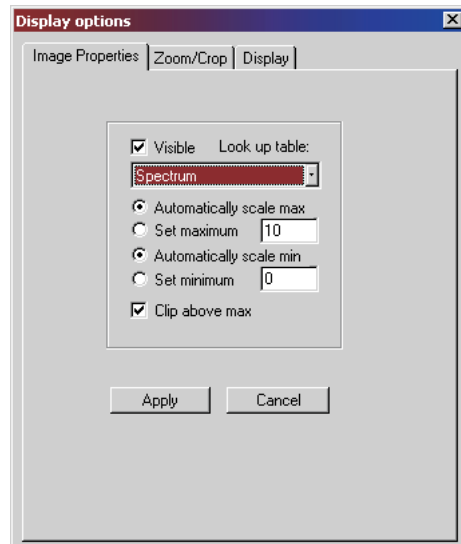


Figure 5.11: Screen shot showing the dialog box used to adjust the way field images are displayed.

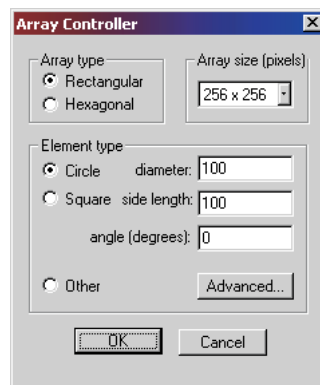


Figure 5.12: Screen shot of dialog used to set the properties of the automatically generated array image.

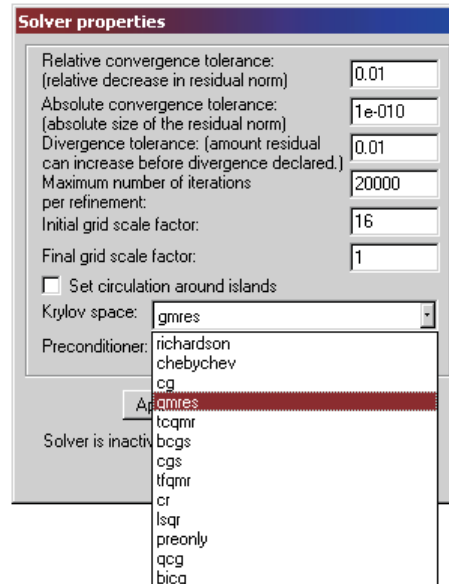


Figure 5.13: Screen shot of the solver-controller dialog showing the daunting list of Krylov subspace iterator options. Fortunately the default settings have been chosen for their good performance on even ill-conditioned geometries. Press “Solve” to solve.

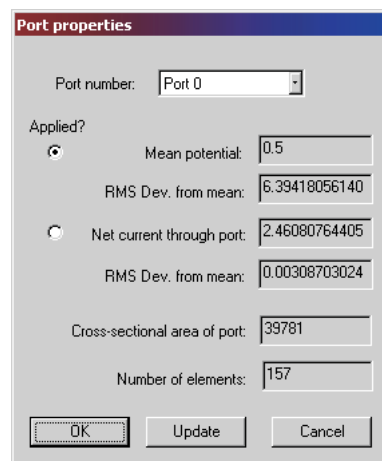


Figure 5.14: Screen shot of the port-properties dialog. This dialog is currently “read only” but that status may change in future developments.

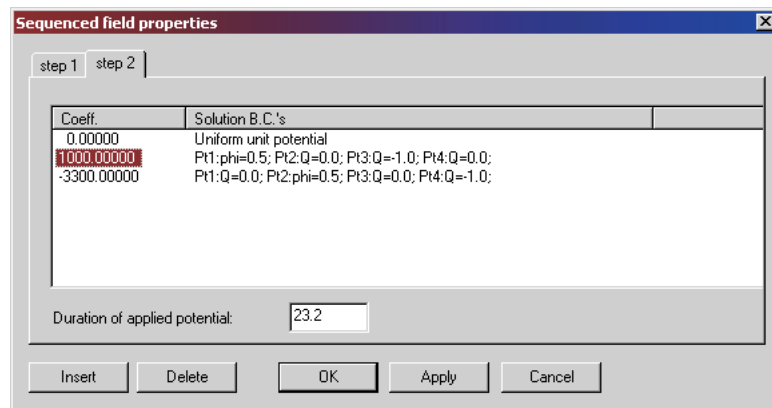


Figure 5.15: Screen shot of the sequenced-field-properties dialog that allows users to specify an arbitrary sequence of propagation steps for post-processing of the solution.

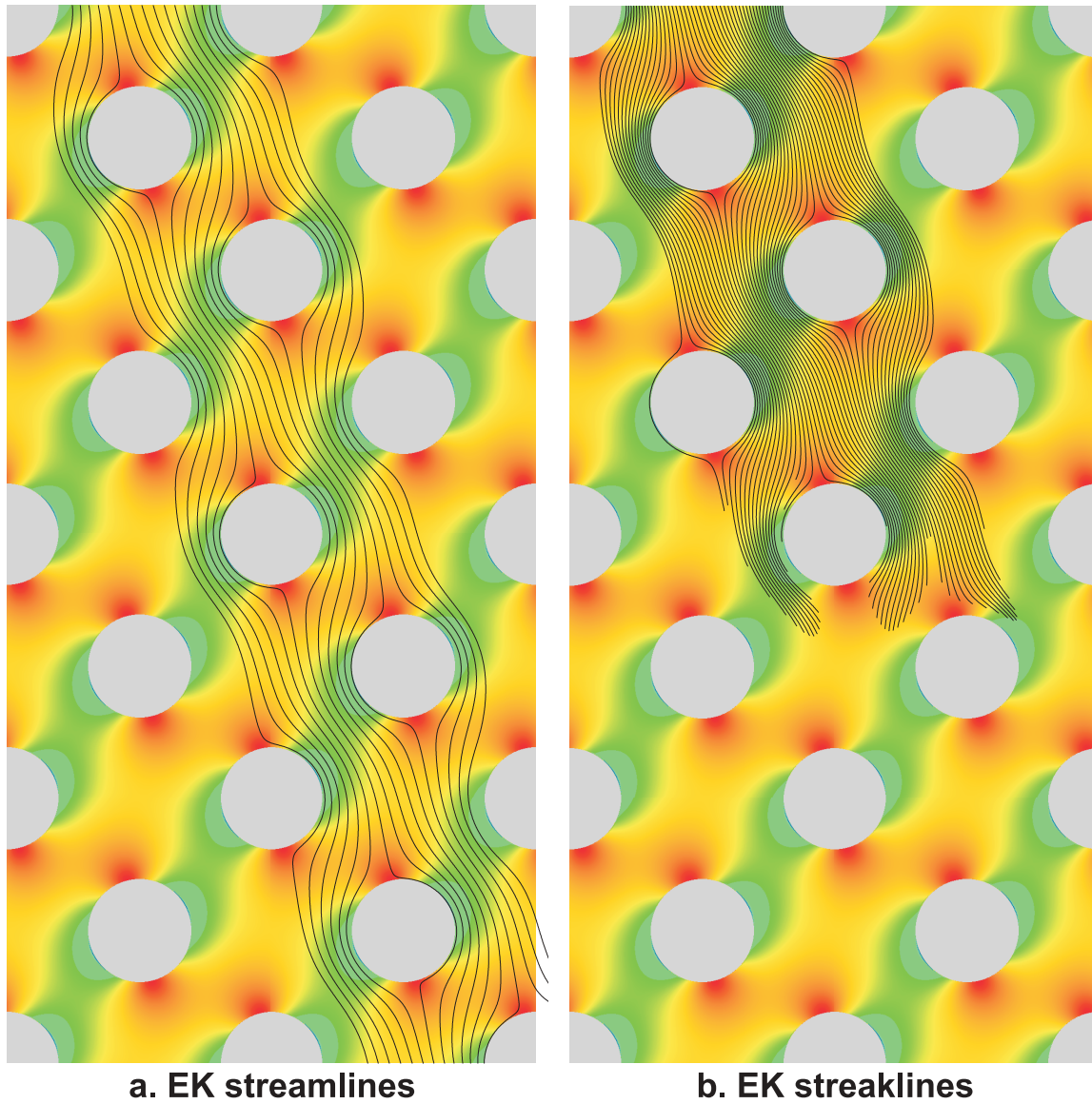


Figure 5.16: Electrokinetic streamlines and streaklines in an array of circular posts. The background image shows a spectral color map of the electrokinetic speed. Blue is the highest speed and red is zero speed.

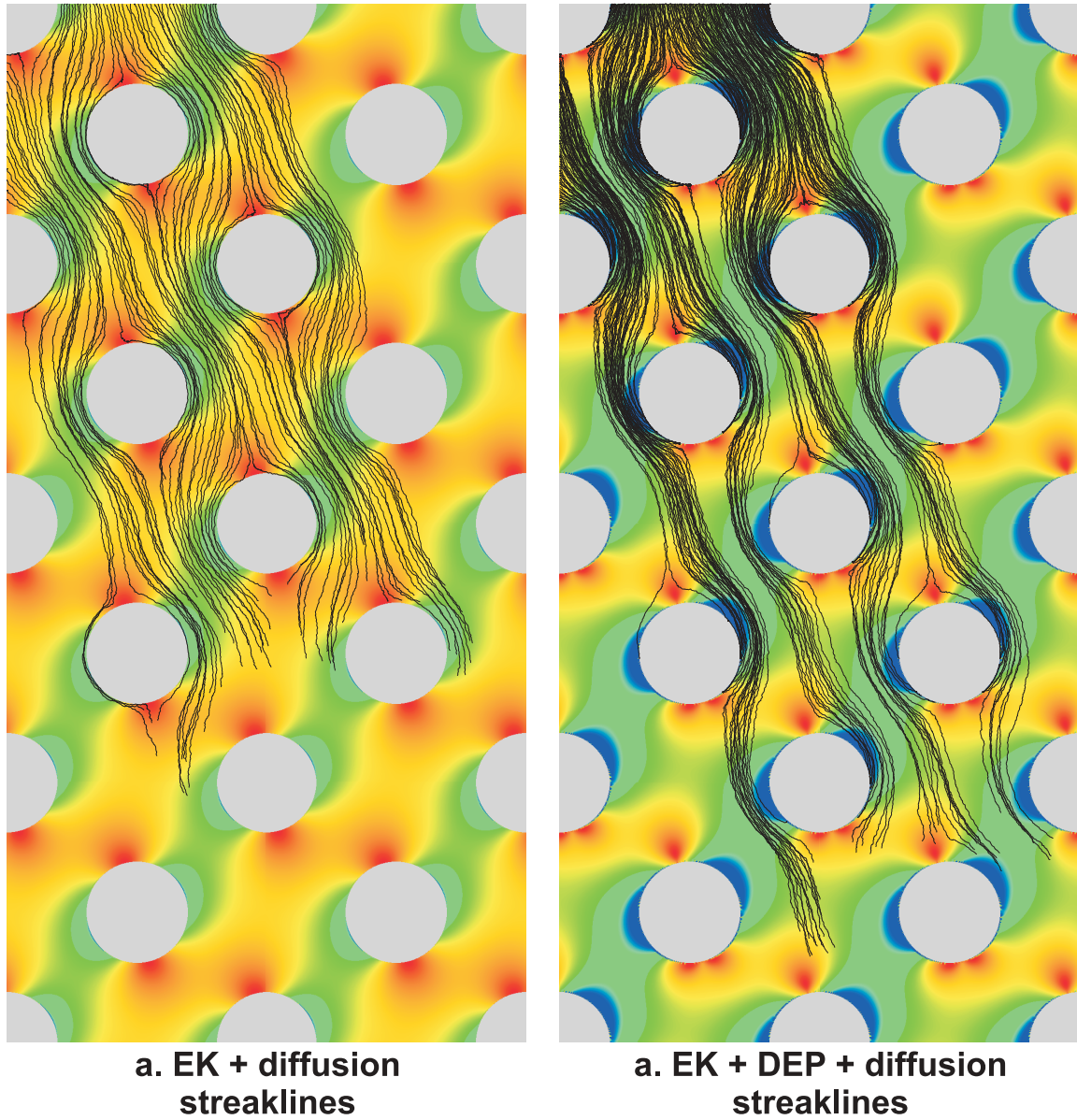


Figure 5.17: Streaklines of simulated particles undergoing electrokinesis and diffusion (a.) and electrokinesis, dielectrophoresis, and diffusion (b.). Trapping dielectrophoresis is evident in b. The background image is a color map of the mean particle speed through the array. Blue is the highest speed and red is zero speed.

This page intentionally contains only this sentence.

Bibliography

- [1] Satish Balay, Kris Buschelman, William D. Gropp, Dinesh Kaushik, Lois Curfman McInnes, and Barry F. Smith. PETSc home page. <http://www.mcs.anl.gov/petsc>, 2001.
- [2] Satish Balay, William D. Gropp, Lois Curfman McInnes, and Barry F. Smith. Efficient management of parallelism in object oriented numerical software libraries. In E. Arge, A. M. Bruaset, and H. P. Langtangen, editors, *Modern Software Tools in Scientific Computing*, pages 163–202. Birkhauser Press, 1997.
- [3] Satish Balay, William D. Gropp, Lois Curfman McInnes, and Barry F. Smith. PETSc users manual. Technical Report ANL-95/11 - Revision 2.1.0, Argonne National Laboratory, 2001.
- [4] J. Cheng, E. L. Sheldon, L. Wu, A. Uribe, L. O. Gerrue, J. Carrino, M. J. Heller, and J. P. OConnell. Preparation and hybridization analysis of dna/rna from e-coli on microfabricated bioelectronic chips. *Nature Biotechnology*, 16:541–546, 1998.
- [5] E. B. Cummings. Applied electrokinetic and pressure-driven microfluidics. *SAND report*, SD-99-8228, 1999.
- [6] E. B. Cummings. An image processing and optimal nonlinear filtering technique for particle image velocimetry of microflows. *Exp. Fluids*, to be published in January 2001.
- [7] E. B. Cummings, S. K. Griffiths, R. H. Nilson, and P. H. Paul. Conditions for similitude between the fluid velocity and electric field in electroosmotic flow. *Anal. Chem.*, 72:2526–2532, 2000.
- [8] E. B. Cummings, R. W. Schefer, and J. N. Chung. A piv methodology for high-resolution measurement of flow statistics. *ASME Internation Mechanical Engineering Congress and Exposition, Nov 5–10, Orlando, FL*, 2000.
- [9] E. B. Cummings and A. K. Singh. Dielectrophoretic trapping without embedded electrodes. *Proc. of SPIE Conference on Micromachining and Microfabrication, September 17–20, Santa Clara, CA*, 4177:164–173, 2000.
- [10] E. Delnoij, J. Westerweel, N. G. Deen, J. A. M. Kuipers, and W. P. M. van Swaaij. Ensemble correlation piv applied to bubble plumes rising in a bubble column. *Chem. Engr. Sci.*, 54:5159–5171, 1999.
- [11] S. Fiedler, S. G. Shirley, T. Schnelle, and G. Fuhr. Dielectrophoretic sorting of particles and cells in a microsystem. *Anal. Chem.*, 70:1909–1915, 1998.
- [12] P. R. C. Gascoyne, Y. Huang, R. Pethig, J. Vykoukal, and F. F. Becker. Dielectrophoretic separation of mammalian-cells studied by computerized image-analysis. *Meas. Sci. & Tech.*, 3:439–445, 1992.

- [13] I. Grant, E. Owens, Y. Y. Yan, and X. Shen. Particle image velocimetry measurements of the separated flow behind a rearward facing step. *Exper. in Fluids*, 12:238–244, 1992.
- [14] N. G. Green and H. Morgan. Dielectrophoretic investigations of sub-micrometre latex spheres. *J. Phys. D*, 30:2626–2633, 1997.
- [15] S. K. Griffiths and R. H. Nilson. Band spreading in two-dimensional microchannel turns for electrokinetic species transport. *Anal. Chem.*, 72:5473–5482, 2000.
- [16] S. K. Griffiths and R. H. Nilson. Electroosmotic fluid motion and late-time solute transport for large zeta potentials. *Anal. Chem.*, 72:4767–4777, 2000.
- [17] S. K. Griffiths and R. H. Nilson. Low-dispersion turns and junctions for microchannel systems. *Anal. Chem.*, 73:272–278, 2001.
- [18] B. He, N. Tait, and F. Regnier. Fabrication of nanocolumns for liquid chromatography. *Anal. Chem.*, 70:3790–3797, 1998.
- [19] T. B. Jones. *Electromechanics of Particles*. Cambridge University Press, Cambridge, 1995.
- [20] H. Kawanabe, K. Kawasaki, and R. Shioji. Gas-flow measurements in a jet flame using cross-correlation of high-speed-particle images. *Meas. Sci & Tech.*, 11:627–632, 2000.
- [21] G. H. Markx and R. Pethig. Dielectrophoretic separation of cells: continuous separation. *Biotechnology and Bioengineering*, 45:337–343, 1995.
- [22] G. H. Markx, J. Rousselet, and R. Pethig. Dep-fff: Field-flow fractionation using non-uniform electric fields. *J. Liquid Chrom. & Rel. Tech.*, 20:2857–2872, 1997.
- [23] C. D. Meinhart, S. T. Wereley, and J. G. Santiago. A piv algorithm for estimating time-averaged velocity fields. *ASME/JSME Fluids Engineering Conference, San Francisco, CA, July 18–23, FEDSM 99-7261*, 1999.
- [24] H. Morgan, M. P. Hughes, and N. G. Green. Separation of submicron bioparticles by dielectrophoresis. *Biophysical Journal*, 77:516–525, 1999.
- [25] F. A. Morrison, Jr. Electrophoresis of a particle of arbitrary shape. *J. Colloid and Int. Sci.*, 34:210–214, 1970.
- [26] N. A. Patankar and H. H. Hu. Numerical-simulation of electroosmotic flow. *Anal. Chem.*, 70:1870–1881, 1998.
- [27] H. A. Pohl. *Dielectrophoresis*. Cambridge University Press, Cambridge, 1978.
- [28] T. J. Praisner, C. V. Seal, L. Takmaz, and C. R. Smith. Spatial-temporal turbulent flow-field and heat transfer behavior in end-wall junctions. *Int. J. Heat & Fluid Flow*, 18:142–151, 1997.
- [29] R. F. Probstein. *Physico-chemical hydrodynamics: an introduction*. John Wiley & Sons, New York, 1994.
- [30] L. D. Reed and F. A. Morrison, Jr. Hydrodynamic interactions in electrophoresis. *J. Colloid and Int. Sci.*, 54:117, 1975.
- [31] F. Regnier. Microfabricated monolith columns for liquid chromatography : Sculpting supports for liquid chromatography. *HRC-J. High Res. Chrom.*, 23:19–26, 2000.
- [32] F. F. Reuss. *Memoires de la Societe Imperiale de Naturalistes de Moscou*, 2:327, 1809.

- [33] C. L. Rice and R. J. Whitehead. *J. Phys. Chem.*, 69:4017–4023, 1965.
- [34] I. Rubinstein. *Electro-Diffusion of Ions*. SIAM, Philadelphia, 1990.
- [35] J. G. Santiago, S. T. Wereley, C. D. Meinhart, D. J. Beebe, and R. J. Adrian. A particle image velocimetry system for microfluidics. *Experiments in Fluids*, 25:316–319, 1998.
- [36] A. K. Singh, E. B. Cummings, and D. J. Throckmorton. Fluorescent liposome flow markers for microscale particle-image velocimetry. *Anal. Chem.*, 73:1057–1061, 2001.
- [37] M. Smoluchowski. *Krak. Anz.*, page 182, 1903.

Distribution

4		Jacob Chung, Mech. Eng. University of Florida Gainesville, FL 32611	
1		Morteza Gharib, Caltech MC 205-45, Pasadena, CA 91125	
1		Tom Sobota, APRI 1925 McKinley Drive, Suite B LaVerne, CA 91750	
1		John McDonnell, McDonnell Boehnen Hulbert & Berghoff 300 South Wacker Drive, 32nd Floor Chicago, IL 60606	
1	MS 1425	Douglas Adkins	Org 1715
1	9403	Arlyn Antolak	8723
1	9161	Walter Bauer	8704
1	9054	Robert Carling	8350
10	9951	Eric Cummings	8358
1	1425	Mark Derzon	1740
1	1425	Gregory Frye-Mason	1715
5	9042	Stewart Griffiths	8728
1	9031	Charles Hartwig	8907
1	0826	Wahid Hermina	9113
1	9401	Jill Hruby	8702
1	9401	Richard Janek	8729
1	9001	Miriam John	8000
1	9404	Wendell Kawahara	8725
1	9409	Glenn Kubiak	8732
1	9103	Jane Ann Lamph	8111
1	9951	Duane Lindner	8101
1	9054	Bill McLean	8300
1	1413	Terry Michalske	1040
1	9053	Charles Mueller	8362
1	9951	Len Napolitano	8130
5	9042	Robert Nilson	8728
1	1094	Michael Oborny	3127
1	0834	Timothy O'Hern	9112
1	9951	Arthur Pontau	8358
1	9051	Larry Rahn	8351
3	0824	Arthur Ratzel	9110
1	9052	Allen Salmi	8361
1	9051	Robert Schefer	8351
1	9951	Joe Schoeniger	8130
1	9951	Anup Singh	8130
1	9004	John Vitko	8100
1	9103	Karl Wally	8111
1	0826	Channy Wong	9113
1	0839	Gerold Yonas	16000
3	9018	Central Technical Files	8945-1
1	0899	Technical Library	9616
1	9021	Classification Office	8511
1		DOE/OSTI via URL	
1	0188	Donna Chavez, LDRD Office 4001	1030